Low-Frequency Instabilities and Plasma Turbulence

by

Dragan B. Ilić

SUIPR Report No. 534

July 1973

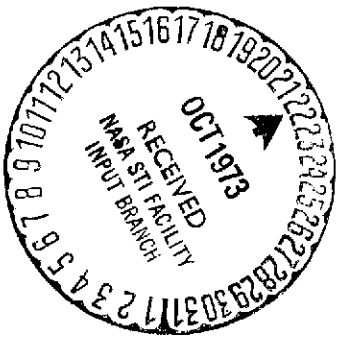

NSF Grant GP-33365
and
NASA Grant NGL 05-020-176

INSTITUTE FOR PLASMA RESEARCH
STANFORD UNIVERSITY, STANFORD, CALIFORNIA

LOW-FREQUENCY INSTABILITIES AND PLASMA TURBULENCE

by

Dragan B. Ilić

NSF Grant GP-33365

and

NASA Grant NGL 05-020-176

SU-IPR Report No. 534

July 1973

Institute for Plasma Research
Stanford University
Stanford, California

LOW-FREQUENCY INSTABILITIES AND PLASMA TURBULENCE

Dragan B. Ilić

Institute for Plasma Research
Stanford University
Stanford, California 94305

This work is a theoretical and experimental study of steady-state and time-dependent characteristics of the positive column and the hollow cathode discharge (HCD). It forms part of a wider program on plasma turbulence.

The steady state of a non-isothermal, cylindrical positive column in an axial magnetic field is described by three moment equations in the plasma approximation. Volume generation of electron-ion pairs by single-stage ionization, the presence of axial current, and collisions with neutrals are considered. The theory covers the range from the low pressure, collisionless régime to the intermediate pressure, collisional régime. It yields radial profiles of the charged particle velocities, density, potential, electron and ion temperatures, and demonstrates similarity laws for the positive column. The results are compared with two moment theories and with experimental data on He, Ar and Hg found in the literature for a wide range of pressures. A simple generalization of the isothermal theory for an infinitely long cylinder in an axial magnetic field to the case of a finite column with axial current flow is also demonstrated.

The excitation characteristics of the current-driven ion acoustic instability are studied by a linearized kinetic model for a weakly ionized plasma, which predicts convective instability for typical positive column conditions. The calculated spatial growth rate shows frequency dependence similar to the amplitude spectra of the instability measured in our positive column experiments in He and Ar. The results point to the important role of collisionless ion Landau damping of the instability for such experimental conditions.

Results of measurements of steady-state characteristics of our HCD apparatus are presented, and the influence of discharge conditions on the excitation and suppression of self-excited, low-frequency instabilities is studied. The spatial variations of amplitude and phase of

density and potential fluctuations of two such modes are presented, and it is concluded that the ambipolar radial electric has a major role in driving these instabilities. A linear perturbation analysis is given for a model based on a fluid description of a collisionless, cylindrical plasma column in the presence of a static axial magnetic field and with radially-varying number density and radial electric field. The instabilities are identified as centrifugal flute modes, driven by Hall drift in the presence of a density gradient and non-uniform radial electric field. The identification is based on reasonable agreement between theory and experiment of the observed and calculated frequencies, mode numbers, and the spatial variations of eigenfunctions of the density and potential fluctuations.

CONTENTS

CONTENTS (Contd.)

CONTENTS (Contd.)

TABLES

ILLUSTRATIONS

ILLUSTRATIONS (Contd.)

ILLUSTRATIONS (Contd.)

ILLUSTRATIONS (Contd.)

LIST OF SYMBOLS

Symbol		Page where first used
	(1) Latin Alphabet	
a	discharge radius	5
$\underset{\sim}{a}$	unit vectors	9
a_0	slope of ionization characteristic	10
$\underset{\sim}{B}$	magnetic field	7
B	normalized ion collision frequency	11
C	electron to ion mass ratio	11
C	Landau contour of integration	40
c	parameter in Eq. (4.2)	72
D	dispersion relation	39
$\underset{\sim}{E}$	electric field	5
e	unit charge	10
F	function defined in Eq. (2.15)	14
f	velocity distribution function	10
G	function defined by Eq. (3.7)	40
I	collision integral	8
I	current	17
i	$(-1)^{1/2}$	38
J	mean current density	17
K	quantity defined by Eq. (2.22)	17
$\underset{\sim}{k}$	wavenumber	38
L	system length	79
M	normalized magnetic field	11
m	mass	7

LIST OF SYMBOLS (Contd.)

Symbol		Page where first used
m	azimuthal mode number	78
N	normalized number density	11
n	local number density	7
$\bar{n}$	mean number density	50
P	probability of ionization	9
p	neutral gas pressure	5
$\underset{\sim}{Q}$	heat flux	8
q	particle charge	7
r	displacement in radial direction	11
r_0	density scale length	104
S	probe area	70
s	normalized radial coordinate	11
s_0	normalized discharge radius	11
T	temperature in energy units	7
t	time	7
u	normalized drift velocity	11
$\underset{\sim}{u}'$	particle thermal velocity	8
V	normalized temperature	11
V	electrode potential	96
$\underset{\sim}{v}$	drift velocity	7
$\bar{v}$	mean drift velocity	52
W	normalized potential	11
$\underset{\sim}{w}$	particle velocity	8
w	normalized frequency	45,107

Symbol		Page where first used
Y	normalized running variable in Eq. (2.15)	14
Z	plasma dispersion function	44
z	displacement in the axial direction	11

(2) Subscripts

A	anode	96
a	starting anode	97
a	ion acoustic	16
c	cyclotron	78
D	drift	10
D	Debye	44
d	diamagnetic	104
E	rotation due to $\underset{\sim}{E} \times \underset{\sim}{B}/B^2$ drift	104
e	electron	7
f	floating	72
i	ion	7
i	imaginary part	40
j	running index	14
n	neutral gas	8
p	plasma	47
r	radial component	9
r	real part	40
s	saturation	70
s	ion sound	40
s	saddle point	42

Symbol		Page where first used
s	space	72
t	thermal	39
x	component along x-axis	10
y	component along y-axis	10
z	axial component	5
0	value on axis	15
0	unperturbed (zero-order) component	38
1	fluctuating (first-order) component	38
θ	azimuthal component	11
$\perp$	perpendicular to z-axis	81

(3) Greek Alphabet

α	normalized ionization frequency	11
$\underset{\approx}{\alpha}$	elements of viscosity tensor, Eqs. (5.4) and (5.5)	103
$\mathcal{E}$	normalized axial electric field	11
ϵ^I	ionization energy	8
ζ	function defined by Eq. (3.7)	40
θ	azimuthal coordinate	9
κ	coefficient of heat conductivity	34
λ	wavelength	44
ν	effective frequency for collisions with neutrals	8
ν^I	ionization frequency	7
ν'	$\nu^I + \nu$	7

LIST OF SYMBOLS (Contd.)

Symbols		Page where first used
ξ	dummy variable	40
π	3.14159 ---	10
$\underset{\approx}{\pi}$	viscosity tensor	103
ϕ	potential	9
φ_1	quantity defined by Eq. (2.18)	16
χ	quantity defined by Eq. (5.7)	104
ψ	quantity defined by Eq. (5.7)	104
Ω	Doppler-shifted angular frequency	40
ω	angular frequency	38

ACKNOWLEDGMENTS

The author gratefully acknowledges his adviser, Prof. F. W. Crawford, for guidance and stimulating discussions during the course of this research, and for numerous constructive comments regarding the manuscript; Dr. S. A. Self for many valuable discussions and critical reading of this thesis; and Prof. V. G. Cerf for his careful reading of the manuscript.

Thanks are due to Dr. T. D. Rognlien for theoretical results of Section 5.2., and to Dr. G. M. Wheeler for help with the measurements of Section 3.2. Technical assistance with the construction of the two experiments from Mr. J. D. MacGowan is appreciated. Ms. E. J. Johnston has expertly typed the manuscript through all the stages of revision.

1. INTRODUCTION

The work to be described in this thesis represents the first steps in a study, both experimental and theoretical, of the turbulent state in two common laboratory plasmas: the positive column and the hollow cathode arc discharge (HCD). Plasma turbulence is normally the result of nonlinear saturation of linear instabilities, driven by sources of free energy in the plasma. For example, the ordered motion of the charged particles, induced by an applied electric field, can cause wave growth when sufficiently strong current passes through the plasma. The instability saturates by some nonlinear mechanism at an energy level which is often significant with respect to the thermal level, so that the macroscopic steady-state plasma characteristics may be altered considerably from their values determined by collisions. While the linear theory of plasma waves and instabilities is well established, and in many cases well confirmed by experiments, much remains to be done toward understanding the nonlinear plasma processes. There have been extensive developments of nonlinear theories, but very few firm experimental results to confirm them or distinguish among rival theoretical models.

The presence of turbulence in plasmas is important to workers whose ultimate goal is to achieve controlled thermonuclear fusion, because it often increases plasma resistivity and thus causes heating; but it may also enhance plasma particle diffusion across magnetic field, and thus be detrimental to plasma confinement. The HCD simulates fusion-type plasmas more closely than the positive column, and is consequently more appropriate for studying turbulence problems relevant to fusion. However, as discussed in Section 4, it is very difficult to describe theoretically many of the observed features of the HCD. We have considered it worthwhile to consider simpler systems first, such as the positive column, because some of the observed features of the HCD can then be predicted, and physical processes responsible for them elucidated.

Our approach to the subject of plasma turbulence is in three steps: first, theoretical models and their experimental verifications are given for the steady-state characteristics of the discharges of interest.

Next, it is important to determine whether these steady states are stable against small perturbations. Here, we examine the excitation of low-frequency, self-excited instabilities in two kinds of plasma sources. We report observations of instabilities and develop suitable theoretical explanations for them. The emphasis on low-frequency oscillations stems from their strong influence on ion motions: they are important for plasma heating, and are also responsible for decreasing the effectiveness of plasma confinement by a static magnetic field. Finally, detailed studies of the saturated instability spectrum and charged particle velocity distributions should be made to determine the character of the interchange between electromagnetic and particle kinetic energy. Our work brings us only to the edges of this last, and most difficult area. It is being investigated further by other members of the Experimental Plasma Physics Group at Stanford.

1.1. Positive Column: Theory and Experiment

At low or medium pressures, the positive column consists of neutral particles, ions, and electrons. The number densities of positive and negative charges are nearly equal, and much lower than ($\lesssim$ 1%) the number density of neutrals. Collisions of charged particles with neutral particles only are important for describing the observed phenomena, so that Coulomb-type collisions may be neglected. The mean free path between successive collisions is larger than the discharge radius at low pressures, and smaller than the discharge radius at medium pressures. The fast electrons charge the walls of the discharge negatively when it is first initiated, and the name derives from the positive charge of the body of the column with respect to the walls.

The first theoretical descriptions of the steady state of the positive column appeared almost 50 years ago,[1,2] and have since been extended to explain observations of both steady-state and time-dependent characteristics of the column.[3,4] Section 2 generalizes the existing isothermal theories to include radially-varying electron and ion temperatures. The model is based on the first three moments of the Boltzmann equation for electrons and ions. It is shown that although the electron temperature is not a strong function of radius, the ion temperature is.

Close to the wall, the ion temperature is much higher than the neutral temperature.[5] Since there are no experimental data on ion temperature in the positive column, many authors assume it to be equal to the neutral temperature. Our results show that such an assumption is not justified.

It is shown in the Appendix that the results of an isothermal theory developed for an infinitely long plasma column by Ewald et al.[3] can be readily generalized to describe a cylinder of finite length.[6] This is relevant to the case of a positive column in a strong static axial magnetic field, when the radial motions of particles are effectively collision-dominated, and the axial motions are collisionless. Consequently, the axial loss of particles dominates the total particle loss, even though the physical length of the discharge is much larger than its radius. A similar simple extension to the non-isothermal theory of Section 2 could not be found.

In Section 3, we discuss ion acoustic waves excited by passage of current through a positive column. The instability is microscopic,[7] i.e., it arises as the result of deviation of the electron velocity distribution function from a local Maxwellian. Accordingly, our theory employs a linear kinetic model of a weakly ionized plasma. The wave dispersion characteristics are analyzed, and shown to predict convective instability, i.e., spatial amplification. The theory is capable of explaining the instability onset characteristics measured in our positive column experiment. Comparison of theory and experiment further demonstrates the importance of collisionless ion Landau damping of the wave for typical experimental conditions.

The linear theory is limited to small perturbations, and cannot explain characteristics of the wave when it is strongly excited. A discussion of some nonlinear models reported in literature which may be relevant to our positive column experiment is given at the end of Section 3.

1.2. The Hollow Cathode Arc Discharge

The HCD of the type studied here is formed as an intense, high-pressure arc inside a hollow cathode, through which gas flows. Charged particles and neutrals diffuse into an evacuated chamber, and are confined near the axis by a static magnetic field, where they form a high-density,

highly-ionized (up to 99%) core, with relatively tenuous external plasma surrounding it. This type of discharge was described in the literature for the first time only about 15 years ago,[8] while theoretical work on its characteristics is even more recent.[9] Even though much work has been reported dealing with the HCD, theory and experiment are still not in close agreement. There is also a lack of experimental data on some important steady-state characteristics, which makes the formulation of theoretical models even more difficult. Section 4 reviews the experimental results and related theoretical work reported in the literature during recent years, and serves to put in proper perspective our work on the HCD.

Section 5 presents the results of our measurements of steady-state and time-dependent HCD characteristics, which have led to the identification of two observed instabilities as centrifugal flute modes. The theoretical model of Section 5.2. for the fluid-type (macroscopic)[7] instability, was developed in the Ph.D. thesis of Rognlien,[10] and uses the measured steady-state parameters of our HCD. Favorable comparison between the calculated radial variations of the eigenfunctions and the measured radial variations of amplitude and phase of potential and density fluctuations of the two observed instabilities is demonstrated.[11]

In contrast to the positive column, Coulomb collisions are of primary importance in the HCD. A thorough description of the steady state of the HCD, of the type developed by Section 2 for the positive column, is lacking, but some insight can be gained into the processes in the HCD from the results of Section 2. For example, the observed negative radial electric field in the HCD indicates that energetic ions are confined near the axis more effectively than by the static magnetic field alone, while the observed magnitude of the radial electric field implies the ions to be significantly more energetic than the neutrals (Section 2.3.2.).

Possible extensions of the present research, with an emphasis on the turbulent heating problem, are discussed in Section 6.

2. THEORY OF AN INFINITELY LONG, STEADY-STATE, NON-ISOTHERMAL POSITIVE COLUMN IN A MAGNETIC FIELD

The early theoretical descriptions of the positive column are of two basic types, depending on the pressure range of applicability.[1,2,12-14] Both types provide information about the radial distributions of potential and density, with electron and ion densities assumed to be equal, and the electrons assumed to be isothermal and Maxwellian. At low pressures, the Tonks-Langmuir free-fall theory[1,12,13] assumes ions to be generated in the volume, and then to move without collisions to the wall, under the influence of the self-consistent electric field. At high pressures, Schottky's isothermal ambipolar diffusion theory describes both ion and electron motions as dominated by collisions, and yields a radial density profile in the shape of a zero-order Bessel function for a cylindrical column.[2] These theories were extended to include energy transfer from electrons in collisions with neutrals in order to explain the observed similarity laws. According to these laws the ratio of axial electric field to pressure, E_z/p , electron temperature, T_e , and the ratio of axial density to current density, $n(0)/J$, depend on p and a only through the pressure-radius product of the column, pa. These theoretical analyses up to 1955 are reviewed by Francis.[14]

Several positive column theories which treat the experimentally important pressure range between the above two limits have appeared in the last ten years. Using the ambipolar diffusion assumption, Persson[15] noted that retaining the nonlinear ion inertia terms in the momentum equations leads to a natural boundary where the ion velocity is equal to either the isothermal or the adiabatic sound speed, depending on the assumptions of the model. At the boundary, the gradients of velocity, density, and potential have infinite values, even in the presence of an axial magnetic field,[16] while the density is non-zero, contrary to the assumption of Schottky's theory.

Kino and Shaw[17] treated a low-pressure discharge column by moment equations for collisionless ions and Maxwellian electrons. This approach was expanded by Self and Ewald (SE)[18] to include the effects of collisions with neutrals of both electrons and ions. Their theory may

be applied for pressures between the free-fall and diffusion regimes. It predicts correctly the results of free-fall theory at low pressure, and ambipolar diffusion theory in the high pressure limit. Next, Ewald, Crawford and Self (ECS)[3] included the effects of an axial magnetic field. Another theory based on isothermal electrons and ions, which neglects magnetic field effects on the ions and shows the transition between the low and high pressure limits, was presented by Forrest and Franklin.[19] In addition, they derive the dependences of electron temperature on axis on pressure and on magnetic field, by using modified plasma balance equations,[1,2] which connect together the column radius, electron temperature, and ionization rate.

The ECS model was extended by Self, who added the ion energy equation and solved for the elements of the ion pressure tensor to obtain a description of the ion kinetics in the adiabatic and collisionless (low pressure) regime.[20] Ecker and Zöller[21] also gave a non-isothermal theory, but considered only the heat conduction from electrons to neutrals, so that their theory applies to high-current, high-pressure discharges.

The present theory extends the ECS analysis to include spatially varying electron and ion temperatures. Thus, in addition to collisions of ions and electrons with neutrals, and magnetic field effects, as introduced by the ECS theory, electron and ion energy equations are added. The ionization frequency varies with electron temperature, and there is an axial current present which provides the energy input necessary for maintaining the discharge.

The additional equations enable us to develop a more complete physical picture of the positive column than the above two-moment models, which need the value of temperature as an input parameter, and do not consider the energetics of the discharge. Once the working gas is specified by its collision frequencies, and the pressure-radius product (pa) of the column is assigned, the values of on-axis temperature and the ratio of the axial electric field and pressure are determined as eigenfunctions of the model, as is the ratio of the on-axis density to the mean current density of the discharge. Integration of the equations further specifies the radial variations of electron and

ion velocities and temperatures, potential, density and ionization frequency.

The model to be analyzed will be discussed in Section 2.1., while the method of solution will be dealt with in Section 2.2. The results of the theory will be compared with experimental results, and results of other theories, in Section 2.3. Finally, Section 2.4. will discuss some of the discrepancies between theory and experiment in relation to the simplifications introduced in the formulation of the model.

2.1. The Model

2.1.1. Moment equations

We shall consider an infinitely long plasma cylinder immersed in a uniform static magnetic field, B_z. The plasma is taken to be quasi-neutral, i.e., the ion and electron densities are assumed to be equal, $n_e = n_i = n$. This is the plasma approximation; Poisson's equation is not used, so that the model does not describe the sheath.

The moment equations of the steady state ($\partial/\partial t = 0$) are derived by taking moments of the Boltzmann equation, as described by Braginskii.[22] We write the moment equations for electrons and ions separately and use subscripts e and i for the two species. Only collisions of ions and electrons with a homogeneous neutral background will be taken into account.

The first moment equation is the continuity equation,

$$\nabla \cdot (n\underset{\sim}{v}) = n\nu^I \ , \qquad (2.1)$$

where electrons and ions are assumed created at a rate proportional to the local plasma density, with the ionization frequency, ν^I, a function of electron temperature, and thus of position.

The second moment equation is the equation of momentum transfer,

$$(\underset{\sim}{v} \cdot \nabla)\underset{\sim}{v} = \frac{q}{m}(\underset{\sim}{E} + \underset{\sim}{v} \times \underset{\sim}{B}) - \frac{\nabla(nT)}{nm} - \nu'\underset{\sim}{v} \ , \qquad (2.2)$$

where q and m represent charge and mass of the particles,

$\nu' = \nu + \nu^I$, where ν is the effective momentum transfer frequency for collisions with neutrals, and T is the temperature in energy units.

The continuity and momentum transfer equations in the isothermal approximation were discussed in Refs. 3 and 18, where it was shown that the assumptions of neutrality and scalar pressure are invalidated near the boundary. However, collisionless theories which consider the sheath correctly by using Poisson's equation[12,13] show that the sheath thickness is small compared to the discharge diameter for typical experimental conditions, so that the phenomena in the positive column are well described even when the plasma approximation is made. Space charge effects in discharges become important at extremely low pressures and low current densities, which are not typical positive column conditions.[23]

The third moment equation is the energy transfer equation. After using the adiabatic assumption ($\nabla \cdot \underset{\sim}{Q} = 0$, where $\underset{\sim}{Q} = mn < u'^2 \underset{\sim}{u}' >/2$ and $\underset{\sim}{u}'$ is the particle thermal velocity) and the continuity equation, this becomes

$$\underset{\sim}{v} \cdot \nabla \left(\frac{m v^2}{2} + \frac{5}{2} T \right) + \nu^I \left(\frac{m v^2}{2} + \frac{5}{2} T \right) = q \underset{\sim}{v} \cdot \underset{\sim}{E} + I \ , \qquad (2.3)$$

where I is the collision integral, which represents the energy exchange per particle of one species due to collisions with particles of other species, in this case with neutrals. $I = (1/2n) \int m \underset{\sim}{w}^2 (\partial f/\partial t)_c \, d\underset{\sim}{w}$, where $\underset{\sim}{w} = \underset{\sim}{v} + \underset{\sim}{u}'$ is the particle velocity, and $\underset{\sim}{v} = \langle \underset{\sim}{w} \rangle$ is the drift velocity.

The electron collision integral describes elastic electron-neutral collisions in which on average the electron loses all of its momentum and the fraction $2 m_e/(m_e + m_n)$ of its energy, and inelastic ionizing collisions in which the electron loses energy equal to the energy of ionization of the particular gas, ϵ^I . Since $T_e \gg T_n$, $m_e \ll m_n$ and $m_e/m_n \simeq m_e/m_i$, where subscript n refers to neutrals, we have

$$I_e = - \epsilon^I \nu^I - 3 \left(\frac{m_e}{m_i} \right) T_e \ . \qquad (2.4)$$

Energy losses due to collisions in which neutrals are excited, which are important in molecular gases, processes of stepwise ionization, and Coulomb collisions are neglected.

The ions are assumed to be created with temperature equal to that of the neutrals. As shown by results of measurements presented by Brown,[24] charge transfer is the dominant mechanism affecting the motion of low energy ions in their own gas. Thus, an ion loses all its momentum and excess energy to neutrals at the rate described by ν_i, and the ion collision integral becomes

$$I_i = \frac{3}{2} \nu^I T_n - \frac{3}{2} \nu_i (T_i - T_n) . \qquad (2.5)$$

The numerical factors in Eqs. (2.4) and (2.5) follow from defining temperature as $T = m \langle u'^2 \rangle / 3$.

The electric field is static, $\underset{\sim}{E} = - \nabla\phi$, where ϕ is a scalar potential function. Since we do not include variations with the azimuthal coordinate θ, $\underset{\sim}{E} = - (\partial\phi/\partial r)\underset{\sim}{a}_r + E_z \underset{\sim}{a}_z$, where E_z is a spatially uniform axial electric field and $\underset{\sim}{a}_r$, $\underset{\sim}{a}_z$ are unit vectors.

The energy equations [Eqs. (2.3)-(2.5)] describe how the external power input qv_zE_z, on the right-hand side of Eq. (2.3) is expended in increasing the internal energy of the particles and in losses due to collisions and flow to the walls. The implications of neglecting the heat fluxes and radiation losses, which simplifies our calculations considerably, are discussed in Section 2.4. Electron-ion collisions and volume recombination are not important, except at very high densities. The wall acts as a sink for electrons and ions, and keeps the neutrals at room temperature.

2.1.2. Collision frequency for ionization

The ionization frequency, ν^I, describes the single-stage process of generation of ion-electron pairs in inelastic collisions of energetic electrons with slow neutrals. The probability for this process to occur $P(w_e)$ (since $w_e \gg w_n$) is zero for electrons with kinetic energies below the ionization energy, and then increases steeply with electron energy. At still higher electron energies, the ionization

probability maximizes and then decreases for very high electron velocities.[25] To calculate ν^I, we start from

$$\nu^I = p\int P(w_e) w_e f(w_e)\, dw_e \,, \tag{2.6}$$

where w_e is the electron speed, $f(w_e)$ is the electron distribution function, p is the neutral gas pressure, and the integration is performed for $w_e > \left(2\epsilon^I/m_e\right)^{1/2}$. We assume a linear dependence of $P(w_e)$ on electron energy above the ionization energy, with slope a_0 as tabulated by von Engel[25] for various gases, $P(w_e) = (m_e a_0/2e)(w_e^2 - 2\epsilon^I/m_e)$, where e is the electron charge.

The electrons drift axially due to axial electric field, so for $f(w_e)$ we use a Maxwellian drifting in the z-direction, $f(w_e) = (m/2\pi T)^{3/2} \exp\{-m[w_x^2 + w_y^2 + (w_z - v_{De})^2]/2T\}$, where subscript e is understood for m and T; $w_e^2 = w_x^2 + w_y^2 + w_z^2$, and v_{De} is the electron axial drift velocity.

Equation (2.6) can be evaluated in spherical coordinates. After integrating out the angular dependences, we obtain

$$\nu^I(T_e, v_{De}) =$$

$$\frac{a_0 pm}{2ev_{De}}\left(\frac{m}{2\pi T}\right)^{1/2} \int_{\left(\frac{2\epsilon^I}{m}\right)^{1/2}}^{\infty} \left(w^4 - 2\epsilon^I \frac{w^2}{m}\right)\left\{\exp\left[-\frac{m}{2T}(w-v_{De})^2\right] - \exp\left[\frac{m}{2T}(w+v_{De})^2\right]\right\} dw \,, \tag{2.7}$$

where subscripts e are understood for m, T, and w. This integral can now be expressed in closed form as a sum of weighted exponential and error functions. The final expression is rather lengthy, and will not be reproduced here. For zero drift, Eq. (2.7) reduces to the expression which is often used as an approximation for ν^I in theories of the positive column,[14]

$$\nu^I = \frac{4a_0 p}{e\left(2\pi m_e\right)^{1/2}} T_e^{3/2} \left(2 + \frac{\epsilon^I}{T_e}\right) \exp\left(-\frac{\epsilon^I}{T_e}\right) . \qquad (2.8)$$

Use of the linear approximation to $P(w_e)$ in Eq. (2.6) is appropriate for a positive column, since there are very few energetic electrons to be affected by the deviation from linearity of $P(w_e)$ at high energies. The representation of $f(w_e)$ in Eq. (2.7) by a drifting Maxwellian is an improvement over Eq. (2.8) which is significant at low pressures, when the drift velocity becomes a sizable fraction of the thermal velocity. We are, however, neglecting the effect of transverse velocity truncation at the wall, which decreases ν^I, and the effect of magnetic field on ν^I, which increases the total velocity by introducing the azimuthal drift velocity into $f(w_e)$, and thus increases ν^I.

In view of the approximations made above, we should expect our theory to hold at very low pressures, and to start breaking down as pressure is increased to near 1 Torr, the exact limit depending on the gas.

2.2. Method of Solution

2.2.1. Normalization and component equations

Equations (2.1)-(2.3) will now be separated into their cylindrical polar components, noting that $\partial/\partial\theta = \partial/\partial z = 0$. First, let us define the following dimensionless quantities:

$$\alpha = \frac{\nu^I}{\nu_e} , \; B = \frac{\nu_i}{\nu_e} , \; C = \frac{m_e}{m_i} , \; M = \frac{eB_z}{m_e \nu_e} , \; \mathcal{E} = \frac{eE_z}{\nu_e (m_e \epsilon^I)^{1/2}} ,$$

$$u = v_r \left(\frac{m_e}{\epsilon^I}\right)^{1/2} , \; u_{\theta,z} = v_{\theta,z} \left(\frac{m_e}{\epsilon^I}\right)^{1/2} , \; s = r\,\nu_e \left(\frac{m_e}{\epsilon^I}\right)^{1/2} ,$$

$$s_0 = a\nu_e \left(\frac{m_e}{\epsilon^I}\right)^{1/2} \quad N = \frac{n(r)}{n(0)} , \; W = \frac{e\phi}{\epsilon^I} , \; V_{e,i} = \frac{T_{e,i}}{\epsilon^I} . \qquad (2.9)$$

Note that even though some symbols are the same, the normalization is very different from that of the ECS theory,[3] which uses electron temperature and ionization frequency as normalizing parameters, both of which are variables here.

The collision frequencies used in this model are directly proportional to pressure. Consequently, the normalized quantities α and B are independent of pressure, while $\mathcal{E}$ is proportional to E_z/p, with the constant of proportionality depending only on the gas type. The collision frequencies may be calculated from electron drift velocity and ion mobility data presented by Brown[24] and von Engel.[25] The values for He, Ar and Hg are presented in Table 2.1, together with the constants of proportionality used for calculating $\mathcal{E}$, V and M.

Equation (2.1) for electrons and ions in dimensionless form becomes:

Continuity:

$$\frac{u}{s} + \frac{du}{ds} + u\,\frac{d\ln N}{ds} = \alpha \ . \qquad (2.10)$$

The component equations of momentum transfer become:

Electron momentum:

$$u\,\frac{du}{ds} - \frac{u_{e\theta}^2}{s} + (\alpha+1)u = \frac{dW}{ds} - Mu_{e\theta} - \frac{dV_e}{ds} - V_e\,\frac{d\ln N}{ds} \ ,$$

$$u\,\frac{du_{e\theta}}{ds} = Mu - (\alpha+1)u_{e\theta} - u_{e\theta}\,\frac{u}{s} \ ; \qquad u_{ez} = -\frac{\mathcal{E}}{1+\alpha} \ ; \qquad (2.11)$$

Ion momentum:

$$\frac{1}{C}\left[u\,\frac{du}{ds} - \frac{u_{i\theta}^2}{s} + (\alpha+B)u\right] = -\frac{dW}{ds} + Mu_{i\theta} - \frac{dV_i}{ds} - V_i\,\frac{d\ln N}{ds} \ ,$$

$$u\,\frac{du_{i\theta}}{ds} = -MCu - (\alpha+B)u_{i\theta} - u_{i\theta}\,\frac{u}{s} \ , \qquad u_{iz} = \frac{C\mathcal{E}}{\alpha+B} \ . \qquad (2.12)$$

TABLE 2.1

Collision data and numerical conversion factors for various gases

Gas	ν_e/p [10^9/sec Torr]	ν_i/p [10^7/sec Torr]	$E_z/p\mathcal{L}$ [V/cm Torr]	T/V [eV]	pa /s_0 [Torr cm]	B_z/pM [G/Torr]
He	2.2	3.0	260	24.5	0.094	126
Ar	5.0	2.0	474	15.7	0.032	303
Hg	8.6	2.1	662	10.4	0.016	490

The scalar energy equations in normalized form are:

Electron energy:

$$u^2\left(\frac{du}{ds}+\frac{\alpha}{2}\right)-\left(1+\frac{\alpha}{2}+\frac{u}{s}\right)u_{e\theta}^2+Mu_{e\theta}u+\frac{5}{2}u\frac{dV_e}{ds}$$

$$=u\frac{dW}{ds}+\frac{\left(1+\frac{\alpha}{2}\right)}{(1+\alpha)^2}\mathcal{E}^2-\alpha-\left(\frac{5}{2}\alpha+3C\right)V_e\ ; \qquad (2.13)$$

Ion energy:

$$\frac{u^2}{C}\left(\frac{du}{ds}+\frac{\alpha}{2}\right)-\left(B+\frac{\alpha}{2}+\frac{u}{s}\right)\frac{u_{i\theta}^2}{C}-uMu_{i\theta}+\frac{5}{2}u\frac{dV_i}{ds}$$

$$=-u\frac{dW}{ds}+\frac{\left(B+\frac{\alpha}{2}\right)C\mathcal{E}^2}{(\alpha+B)^2}+\frac{3}{2}(\alpha+B)V_n-(5\alpha+3B)\frac{V_i}{2}\ . \qquad (2.14)$$

To complete the set, we have the expression for ionization frequency, $\alpha(V_e,u_{De})$, which follows directly from Eq. (2.7). Since $v_{De}=v_{ez}$, it follows from the expression for u_{ez}, Eq. (2.11), that $\alpha=\alpha(V_e,\mathcal{E},\alpha)$.

2.2.2. Starting values for integration

The next step is to manipulate Eqs. (2.10)-(2.14) algebraically in such a way as to obtain a system of seven coupled nonlinear differential equations of the form

$$dY_j/ds=F_j(\alpha,Y_1,Y_2,\ldots,Y_7)\ ,\ j=1,\ldots 7\ , \qquad (2.15)$$

where $Y_1=u$, $Y_2=u_{i\theta}$, $Y_3=u_{e\theta}$, $Y_4=N$, $Y_5=W$, $Y_6=V_e$, $Y_7=V_i$, are the normalized variables whose variation with s we want to find, and F_j are the corresponding nonlinear algebraic expressions involving the above variables. These differential equations may be integrated simultaneously by numerical methods, together with the subsidiary relation

for α , starting from the axis. There are numerical difficulties on axis due to the s^{-1} terms, so that Taylor expansion of the equations must be performed, and the integration is started close to the axis. It is assumed that the potential, the velocities and the first derivatives of the temperatures, density and potential with respect to radius are zero, while $N = 1$, at $s = 0$.

The energy equations yield two additional relations which determine the values of the electron and ion temperatures at the axis in terms of the collision frequencies and the axial electric field. At $s = 0$, the electron energy equation reduces to

$$V_{e0} = \left[\frac{\alpha_0 + 2}{(\alpha_0 + 1)^2}\,\mathcal{E}^2 - 2\alpha_0\right] \Big/ (5\alpha_0 + 6C) \ , \qquad (2.16)$$

while the ion energy equation becomes

$$V_{i0} = \left[\frac{(\alpha_0 + 2B)C\mathcal{E}^2}{(\alpha_0 + B)^2} + 3(\alpha_0 + B)V_n\right] \Big/ (5\alpha_0 + 3B) \ , \qquad (2.17)$$

where the ionization frequency, α_0 , is understood to be $\alpha(V_{e0})$ in both equations.

The value of on-axis electron temperature, V_{e0} , follows from the simultaneous solution of Eqs. (2.7) and (2.16). A double iteration numerical procedure is used to obtain a corresponding pair of values (V_{e0}, α_0) for each assigned $\mathcal{E}$.

Since for $V_{e0} > 0$ Eq. (2.7) implies $\alpha > 0$, it follows from Eq. (16) that $\mathcal{E} > 0$. In case of $\alpha \ll 1$, this condition reduces to $ev_{ez}E_z > \nu^I \epsilon^I$. This means that the energy gained by an electron from the axial current must be sufficient to at least offset the loss of energy due to inelastic ionizing collisions. It follows that the positive column must be supplied with energy from the outside, in this case via axial current.

2.2.3. Integration and location of radial boundary

It remains to derive, and then to integrate numerically, the differential equations expressed by Eq. (2.15). The first of these is

$$\frac{du}{ds} = \frac{\varphi_1}{5(V_e+V_i) - 3u^2(1+1/C)} , \tag{2.18}$$

where

$$\varphi_1 = \varepsilon^2 \left[\frac{2+\alpha}{(1+\alpha)^2} + \frac{(\alpha+2B)C}{(\alpha+B)^2}\right] + 3(\alpha+B)V_n - 2\alpha - 6CV_e - 3BV_i$$

$$+ u^2 [4\alpha(1+1/C) + 5(B+C)/C] + (2+\alpha)u_{e\theta}^2 + (2B+\alpha)u_{i\theta}^2/C$$

$$- 3Mu(u_{i\theta}-u_{e\theta}) - [5(V_e+V_i) + 3(u_{e\theta}^2 + u_{i\theta}^2/C)]u/s .$$

Equation (2.18) shows that the gradient of the radial velocity becomes infinite when the velocity becomes equal to the adiabatic ion acoustic speed, $v_a = [5(T_e+T_i)/3(m_e+m_i)]^{1/2}$. As discussed by Persson,[15,16] this singularity determines the position of the radial boundary, i.e., the coordinate s_0 where the integration of Eq. (2.15) is to be terminated. If the electron nonlinear inertia terms had not been retained in Eq. (2.11), the singularity in Eq. (2.18) would depend on magnetic field, and the adiabatic ion acoustic speed would not be obtained at the boundary.

It follows from Eqs. (2.11) and (2.12) that the slopes of $u_{e\theta}$ and $u_{i\theta}$ are not infinite at s_0 . The slopes of density, potential, and the electron and ion temperatures are infinite at s_0 , however, as may be seen by forming the remaining four expressions of Eq. (2.15). These are lengthy, and will not be reproduced here.

It is convenient to use s as the independent variable near the axis, and u near the boundary, where it is numerically difficult to handle large values of du/ds.[3] It is found that the boundary coordinate, s_0 , decreases when M and α are increased. We keep α as a variable throughout the integration.

Next, we derive a relation connecting the axial electron density, $n(0)$, and the mean current density in the column $J = I/\pi a^2$, where I is the total current in the discharge,

$$I = 2\pi \int_0^a env_z r \, dr \,, \tag{2.20}$$

where $v_z \equiv v_{iz} - v_{ez}$. Hence, in terms of normalized variables, we have

$$\frac{n(0)}{J} = K \frac{(pa)^2}{(E_z/p)} \,, \tag{2.21}$$

where K depends on the gas type and pressure via the density profile,

$$K = \frac{\nu_{e0}^3 m_e^2}{2 e^2 \epsilon^I \int_0^{s_0} s \, N \left[(\alpha+B+C)/(\alpha+1)(\alpha+B)\right] ds} \,, \tag{2.22}$$

where $\nu_{e0} = \nu_e/p$ and $C \ll 1$ in the expression for u_z. The value of K is established numerically in the course of integrating Eq. (2.15).

Once the integration is performed, and the radial boundary is thus determined, the value of s_0 yields the pressure-radius (pa) product, since by Eq. (2.9), $s_0 = a\nu_e(m_e/\epsilon^I)^{1/2}$ (see Table 2.1). By repeating the integration for a wide range of values of $\mathcal{E}$, we obtain the values of $\mathcal{E}$, V_{e0} and $n(0)/J$ for various values of s_0. By Table 2.1, these correspond to dependences of E_z/p, T_{e0}, and $n(0)/J$ on pa; they constitute the similarity laws for the positive column.[14]

2.3. Results

2.3.1. No magnetic field

Similarity laws: The results of simultaneous solution of Eqs. (2.7) and (2.16) are presented in Figs. 2.1 and 2.2. The broken lines in both figures indicate the simultaneous solution of Eqs. (2.8) and (2.16) for He, and show that the effect of drift on the ionization frequency

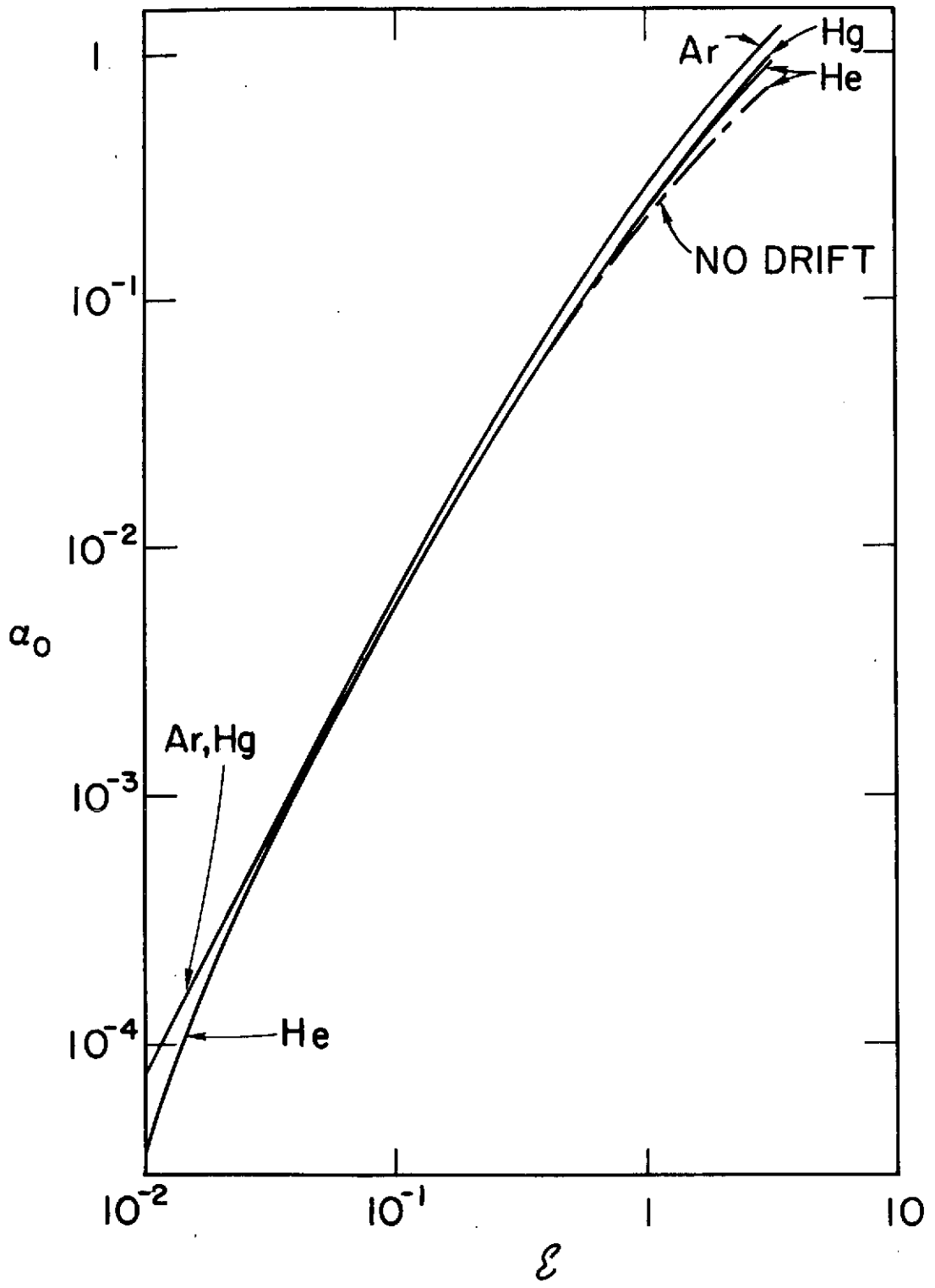

FIG. 2.1. The dependence of normalized ionization collision frequency at the axis on normalized axial field for various gases. The broken line is the result for He without axial drift in the ionization frequency.

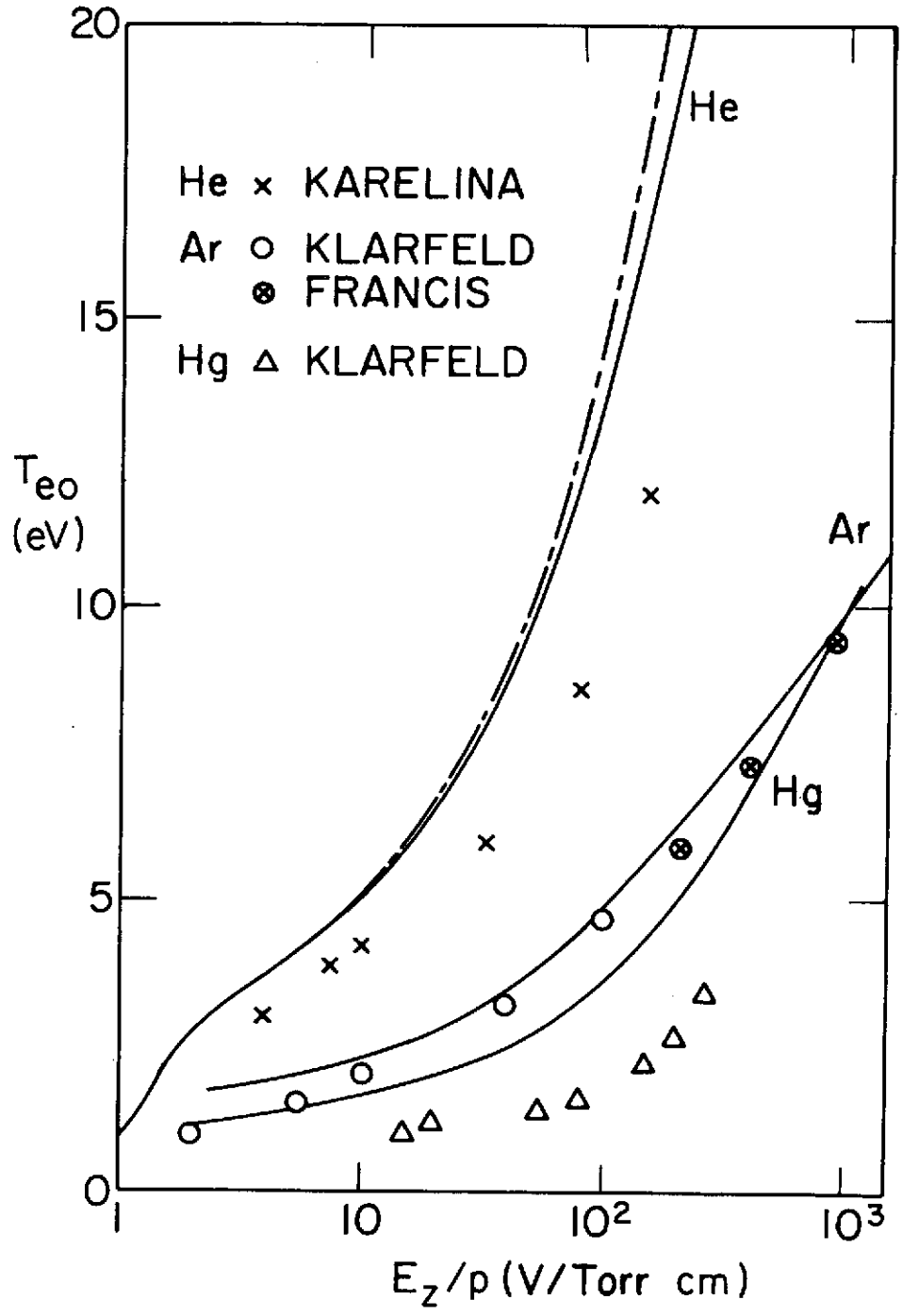

FIG. 2.2. Comparison of calculated (full lines) and experimentally-measured (points) dependences of T_{eO} on E_z/p for three gases. Experimental data from Refs. 14, 26-28. The broken line is calculated for He without axial drift in the ionization frequency.

becomes significant at low pressures. Figure 2.1 shows that $\alpha \ll 1$ for a wide range of values of $\mathcal{E}$ which correspond to high pressures, and that α depends in a very similar way on $\mathcal{E}$ for the three gases shown. In Fig. 2.2 the $V_{e0}(\mathcal{E})$ dependence has been converted to $T_{e0}(E_z/p)$ by using the conversion factors in Table 2.1. This enables direct comparison with experimental points indicated in the figure. The three gases considered here were chosen because results of measurements for a wide range of pressures are to be found in the literature.[14,24-28]

The integration of the full set of equations is performed next by numerical methods for a wide range of $\mathcal{E}$ values. The resulting dependence of the boundary s_0 on $\mathcal{E}$, and thus on V_{e0}, corresponds to dependences of T_{e0} and E_z/p on pa, as explained in Section 2.2.3. The results are shown in Figs. 2.3 and 2.4 together with experimental data. The broken lines again indicate results for He when $v_{De} = 0$ in Eq. (2.7).

When comparing experimental data with calculated curves, one should bear in mind that measurements on the positive column represented by points in Figs. 2.2-2.4 are results of Langmuir probe measurements, which are subject to errors of typically ± 10%. In addition, the results of nominally identical experiments show additional spread, presumably due to differences in factors such as errors in pressure and current density measurements, and the presence of impurities in the gas.

The agreement of theory and experiment demonstrated by Figs. 2.2-2.4 for He is good for a wide range of pressures. The effect of drift on the ionization collision frequency is significant at low pressures. The comparison of experiments and computations is not so favorable for Hg and Ar, probably because our model neglects such effects as radiation and secondary ionization in these gases. The agreement is poorest for the dependence of E_z/p on pa, while the differences between theory and experiments for T_{e0} are within 30%.

The results of evaluating Eq. (2.21) for He, Ar and Hg for a range of pa values are shown in Fig. 2.5, together with experimental points.[26-28] The broken lines are results for He for non-zero magnetic field to be discussed in the next subsection. The agreement

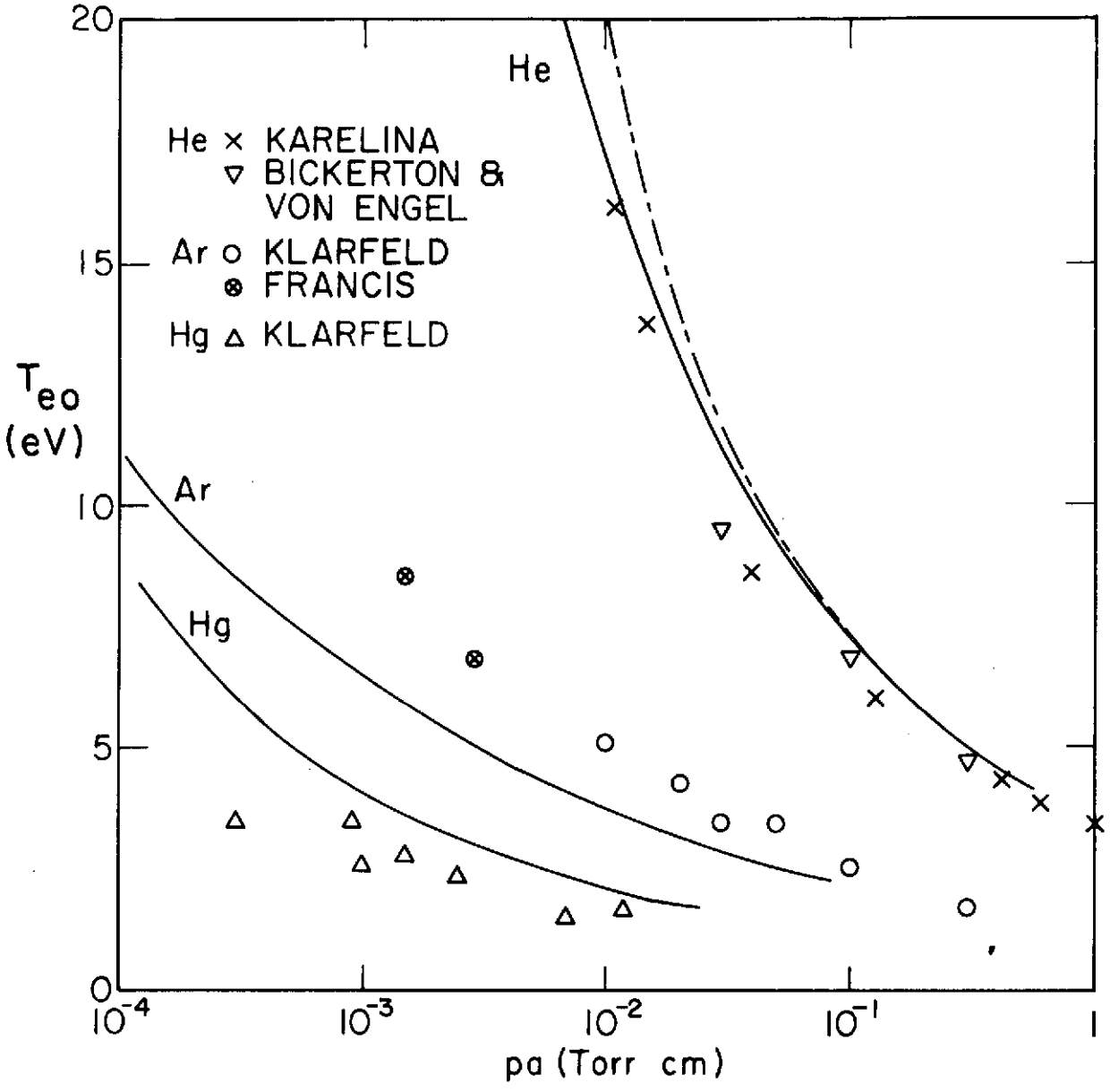

FIG. 2.3. Comparison of calculated and experimental $T_{eO}(pa)$ dependences for He, Ar and Hg. Notation as in Fig. 2.2.

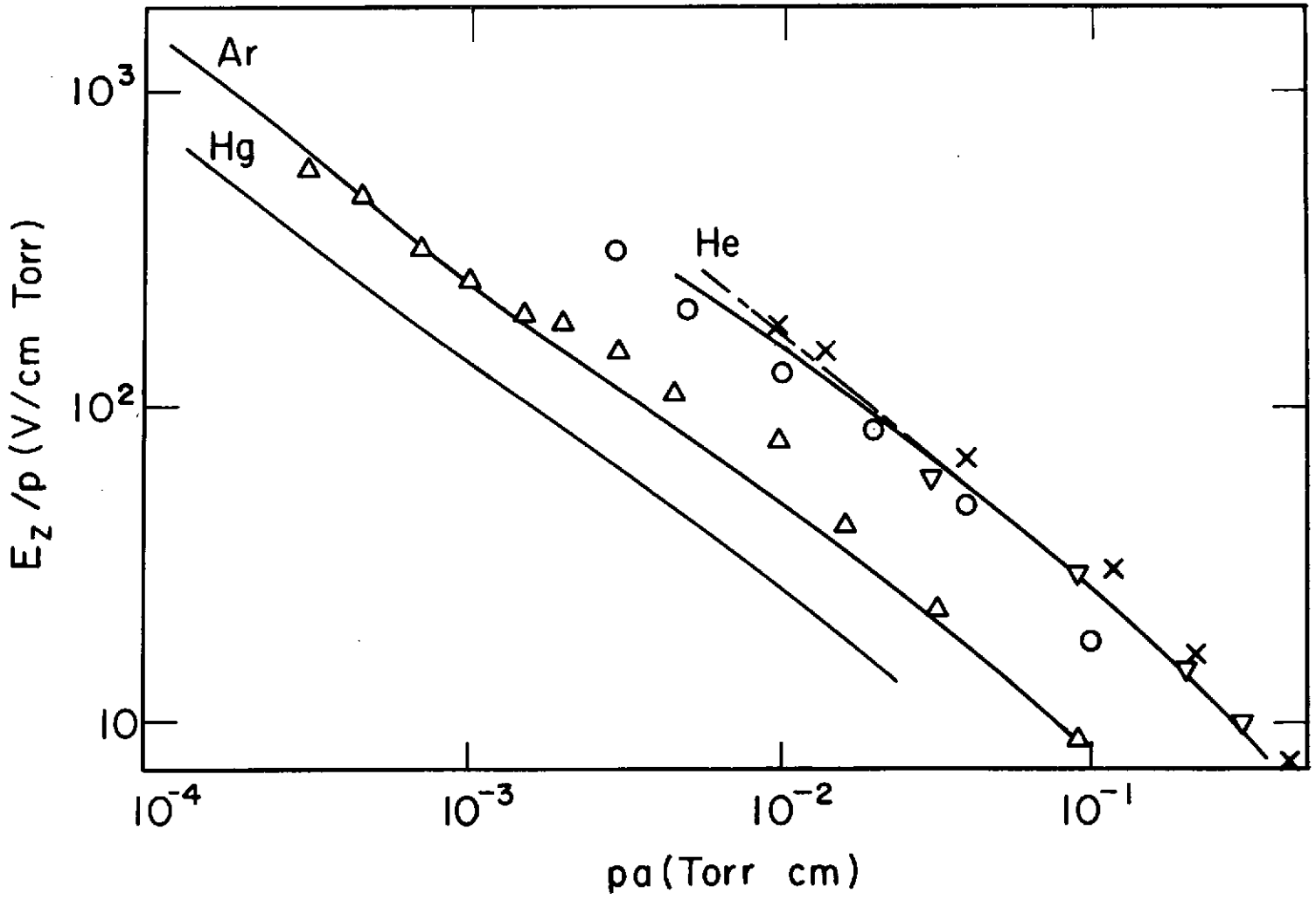

FIG. 2.4. Comparison of calculated and experimental dependences of E_z/p on pa for He, Ar and Hg. Notation as in Fig. 2.2.

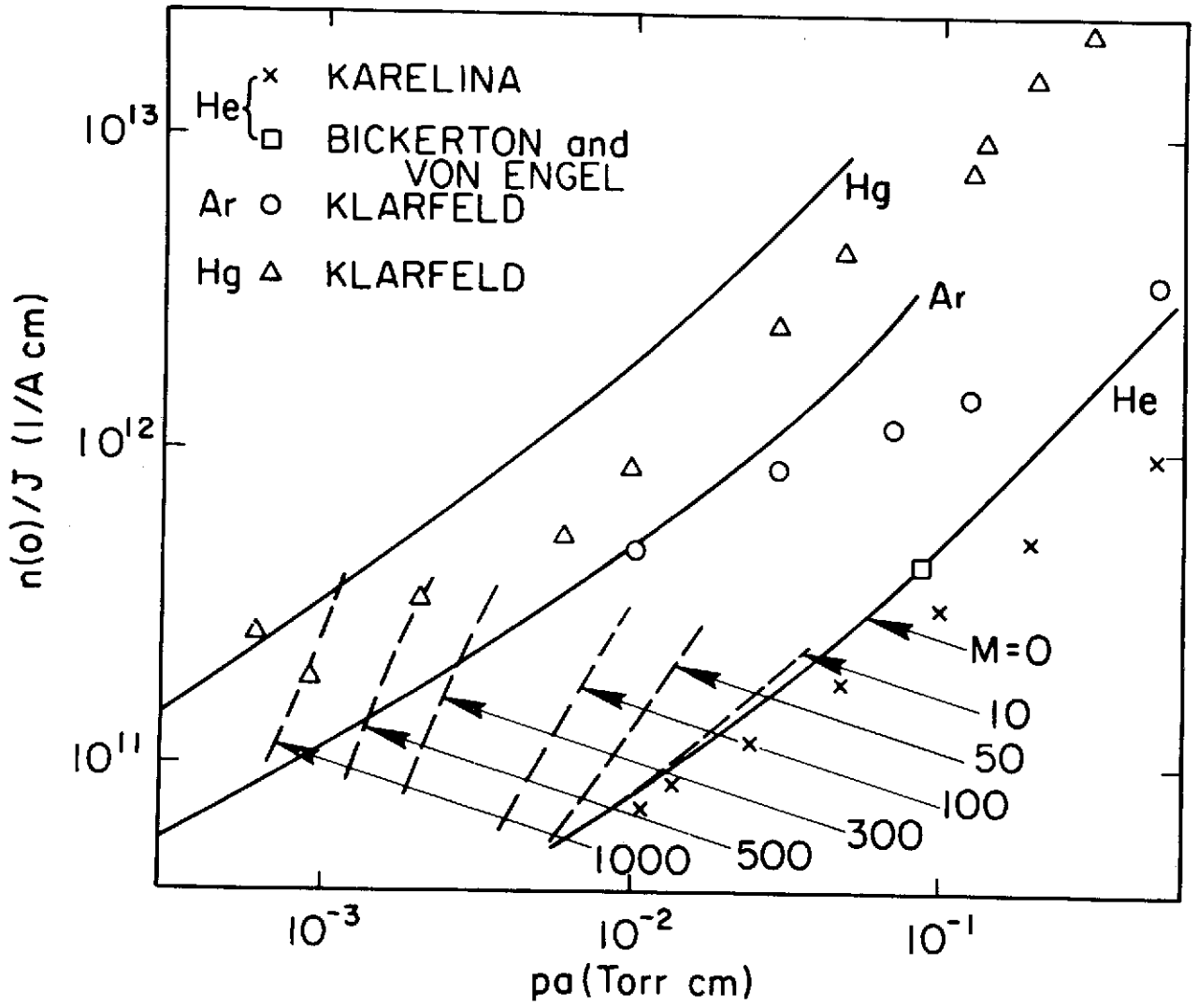

FIG. 2.5. The dependence of n(0)/J on the pa product for He, Ar and Hg. Notation as in Fig. 2.2. The broken lines are calculated values for He in non-zero magnetic field.

for He is good, especially at low pressures, while the other two gases again show poorer agreement.

Radial profiles: The radial profiles of normalized plasma density, potential, electron temperature, ambipolar radial velocity, and ion temperature in He for various pa values are shown in Figs. 2.6(a)-2.6(e), respectively. The results in Figs. 2.6(a) and 2.6(d) agree qualitatively with the results of two-moment theories. Both theories predict that the velocity profile is flattened with increasing pressure, and that the density profile becomes steeper at higher pressures. For comparison, some results of Ref. 18 are plotted as broken lines in Fig. 2.6(a). Direct comparison is not possible, because the two-moment theories cannot identify a particular curve with a specific pa value, but it is seen that our results fall between the high- and low-pressure limits of the two-moment theory.[18]

The electron temperature variation in Fig. 2.6(c) shows that the temperature decreases with increasing pressure, as in Fig. 2.3, and that the profile is somewhat steeper at low pressures. There is little variation in the body of the discharge, but a drop occurs near the wall.

The profiles of potential, when inverted, and ion temperature, Figs. 2.6(b) and 2.6(e), resemble each other closely: at low pressures both are steep, flattening out as pressure is raised. The axial value of the ion temperature is very close to the neutral temperature at low pressures, increases with pressure, and then returns to the neutral temperature at high pressures. This may be seen by studying Eq. (2.17) for various values of α and $\mathcal{E}$, as dictated by Fig. 2.1.

Off axis, the ion temperature becomes much larger than the neutral temperature, as anticipated by Bickerton and von Engel.[28] The collisionless theory of Self[20] also found that the maximum V_i appears near the wall, and that it is much larger than the neutral temperature. Fig. 2.6(e) shows that $T_i \sim 1$ eV in He near the wall. Ion temperature is difficult to measure, since the intensity and broadening of spectral lines emitted from the positive column are insufficient for accurate spectroscopic diagnostics. This theory provides the $T_i(r)$ variation, which is important for calculating the ion Landau damping of ion waves propagating in the positive column (see Section 3).

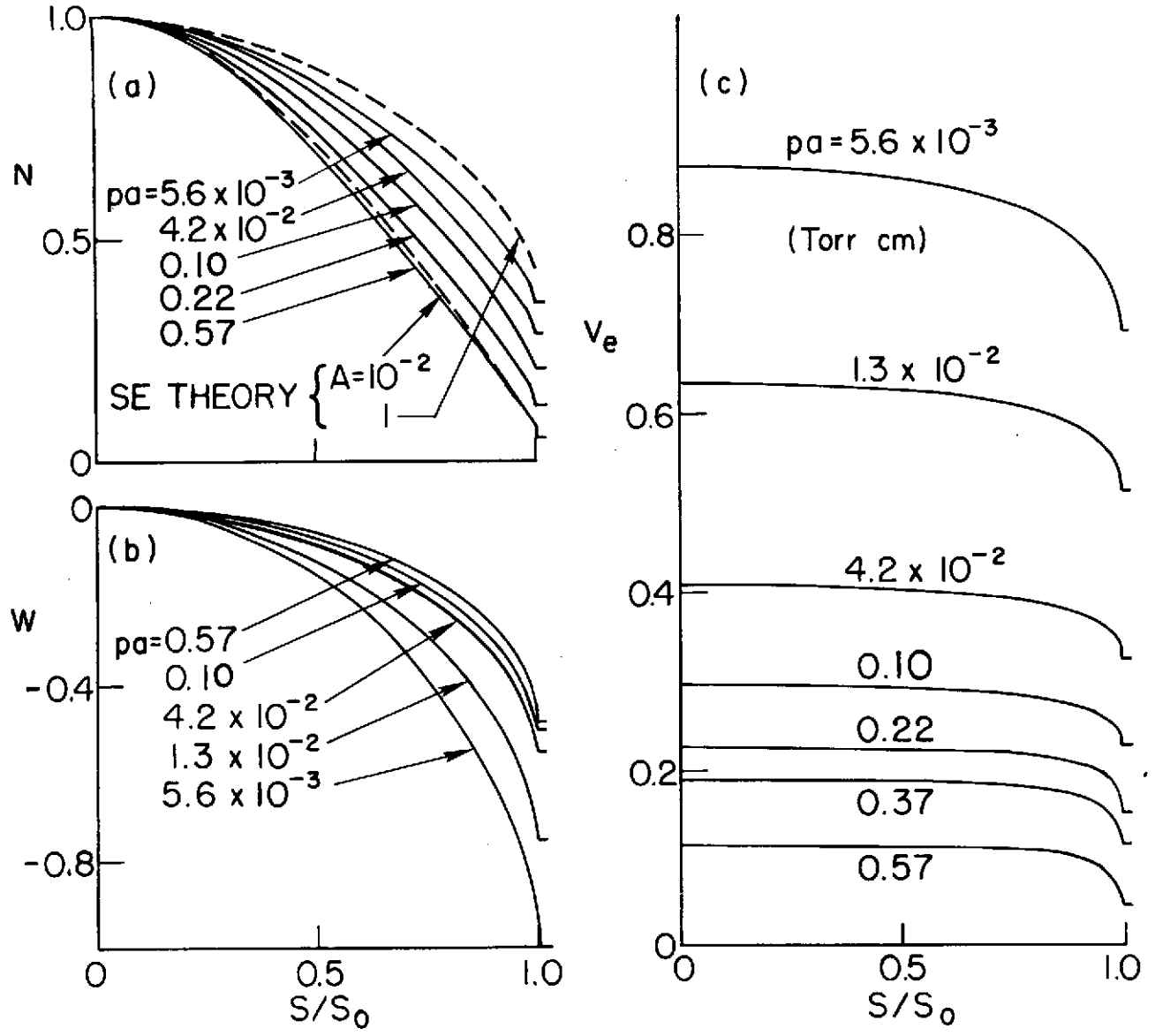

FIG. 2.6. The radial variations of normalized values of (a) plasma density; (b) potential; (c) electron temperature. The broken lines in (a) are results of Ref. 18.

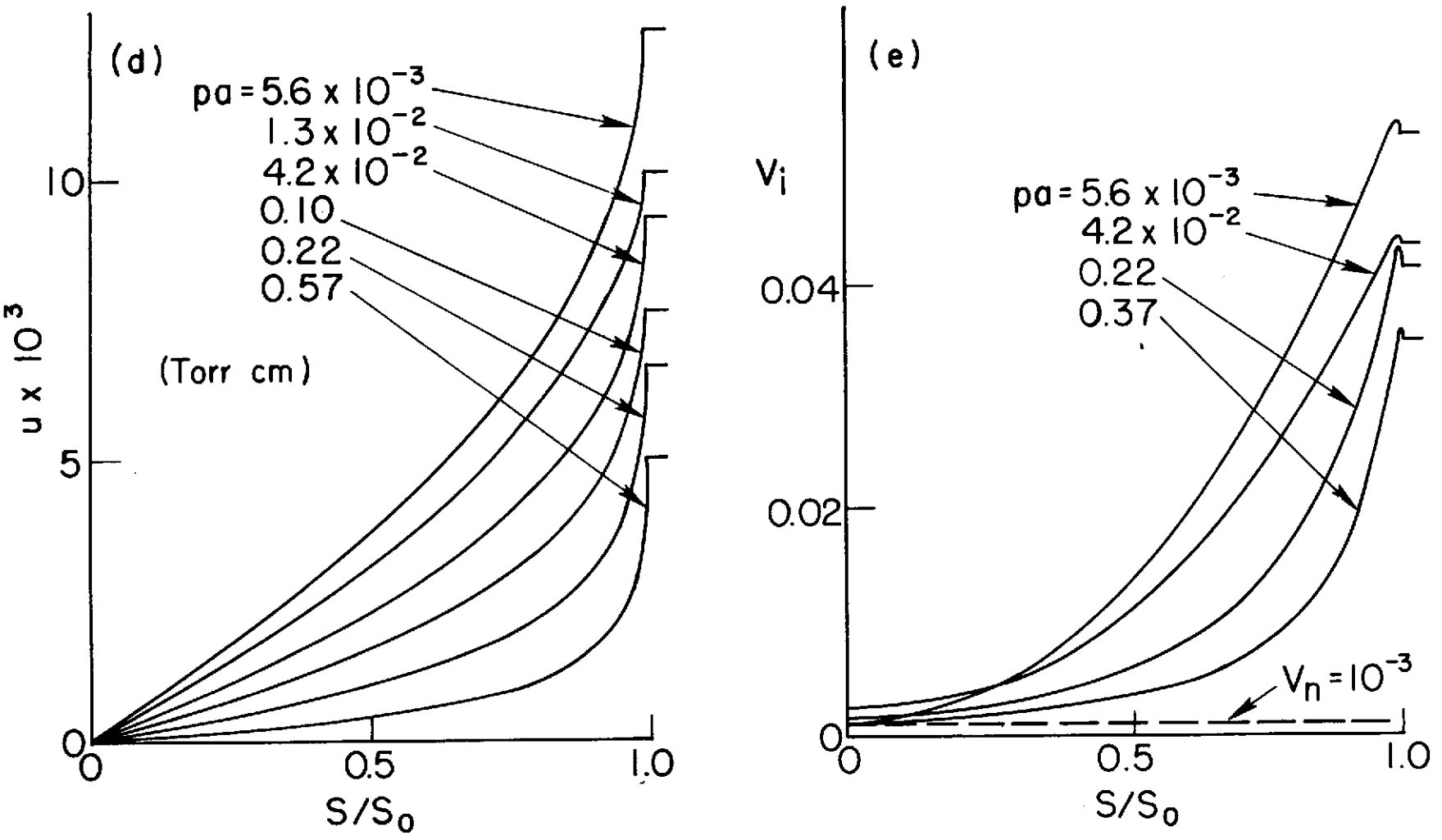

FIG. 2.6. The radial variations of normalized values of (d) ambipolar radial velocity; and (e) ion temperature for various values of pa.

Finally the variation of ionization rate, α, with radius is not shown, because it follows closely the variation of electron temperature, dropping off sharply as V_e starts to decrease. The actual radial dependence of α may be deduced by combining Figs. 2.1, 2.2 and 2.6(c).

2.3.2. Magnetic field effects

Similarity laws: The presence of a static axial magnetic field affects neither our ionization frequency nor our energy equations, so that Figs. 2.1 and 2.2 still hold. The presence of magnetic field terms in the momentum equations causes the normalized radial velocity to become equal to the normalized adiabatic sound speed much closer to the axis than without the magnetic field, so that the value of s_0 is decreased. Computer runs were made for He in order to determine the similarity relations equivalent to Figs. 2.3 and 2.4 for non-zero magnetic field. The result is shown in Fig. 2.7 with T_{e0}(pa) plotted for various values of M. The corresponding dependence of E_z/p on pa may be obtained by combining Fig. 2.2 for He with Fig. 2.7. Thus, in the presence of magnetic field, T_{e0}, E_z/p and $n(0)/J$ are functions of pa and B_z/p.

Our theory introduces magnetic field effects through M, which is directly proportional to the ratio of magnetic field to the pressure (see Table 2.1). Thus, the magnetic field itself is not constant for a curve with constant M in Fig. 2.7 when the pressure varies. Once the column radius is specified, however, Fig. 2.7 may be used together with Fig. 2.2 to see how T_{e0} and E_z/p are affected by the presence of magnetic field. As an example, for a hypothetical 1 cm radius discharge at a pressure of 10 mTorr, the axial electron temperature will be 17.2, 17.0, 14.5 and 10.0 eV for magnetic fields of 0, 13, 65 and 130 G, respectively. The corresponding E_z is 1.60, 1.55, 1.10 and 0.50 V/cm, respectively.

It follows from Eqs. (2.20)-(2.22) that $n(0)/J$ should increase with increase in magnetic field, since both E_z/p and the value of the integral in Eq. (2.22) decrease with increase in magnetic field. The solutions presented in Fig. 2.5 show the anticipated behavior, as do measurements of Ref. 28.

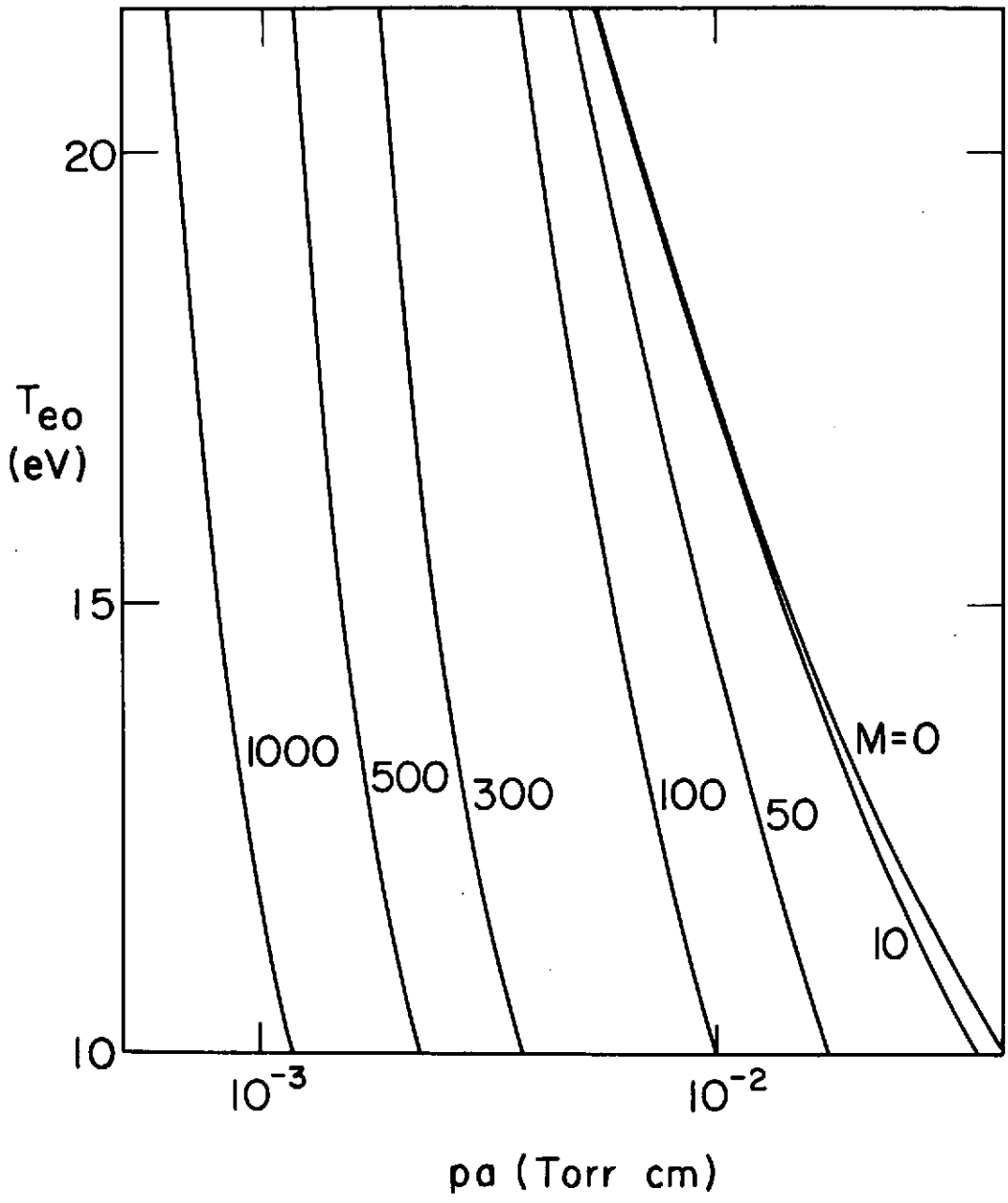

FIG. 2.7. The dependence of T_{eo} on pa for He in the presence of an axial static magnetic field.

The experimental data on the positive column in a magnetic field are not as abundant as for the case of no magnetic field. Bickerton and von Engel[28] present results of measurements on a He column, but in a range of fairly high pa values. They show that both E_z/p and T_{e0} decrease with magnetic field and pressure, as is also shown by our Figs. 2.7 and 2.2. Thus, their observations agree qualitatively with results of our theory, but no direct comparison similar to the previous section can be made because of computational difficulties we encounter at high pressures.

These numerical obstacles result from difficulties in performing the integration of Eq. (2.15) for low values of V_{e0}, which correspond physically to high pressures. The difficulty may be understood by noting from Eq. (2.10) that the slope of the radial velocity on axis is $\alpha/2$, which drops very rapidly as V_{e0} decreases. Thus, in starting the integration of Eq. (2.18) near the axis, the initial radial increase of u becomes less than the rounding errors of computation for low values of α, at which time the integration becomes impossible. The situation is more complicated since seven coupled equations are integrated simultaneously. Furthermore, in the presence of magnetic field, the interval of integration is reduced, and the integration has to start even closer to the axis, so that the limit of high pressure values, where the integration becomes difficult, is reached for much lower pressures than without magnetic field.

Radial profiles: Figures 2.8(a)-(e) show how the computed profiles of normalized density, electron temperature, potential, radial velocity, and ion temperature vary as the magnetic field is increased at constant pressure. As already shown by results of two-moment treatments,[3,19] the radial velocity profile flattens as the magnetic field is increased, [see Fig. 2.8(d)], while the density variation with radius becomes steeper as the magnetic field is increased [Fig. 2.8(a)]. Similar steepening of the density profile has been observed experimentally by Little and Jones in a mercury-vapor column.[29] The variation of potential is similar to that described by the ECS theory.[3] The lowest value of magnetic field at which potential inversion occurs corresponds to

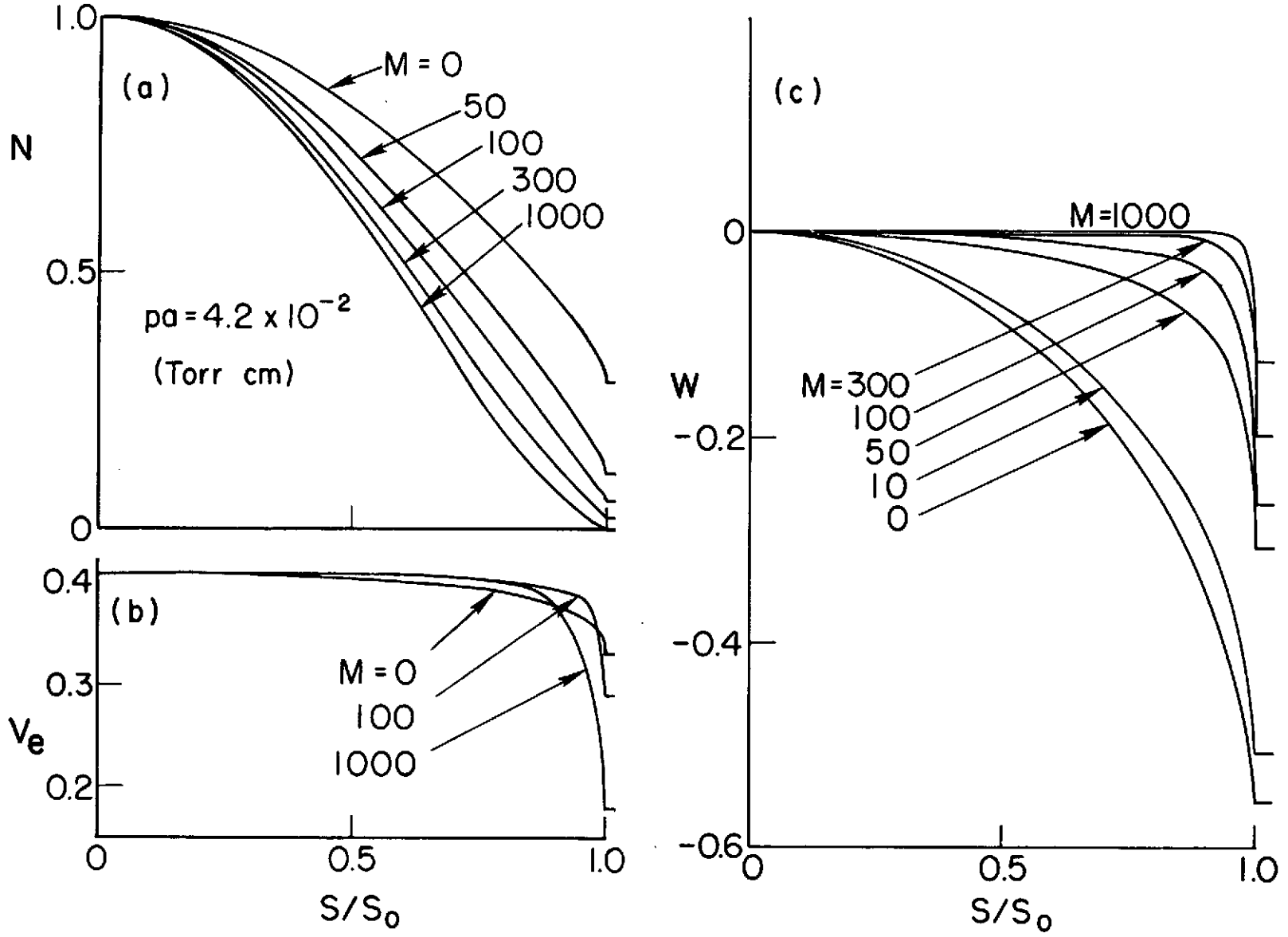

FIG. 2.8. The radial variations of normalized values of (a) plasma density; (b) electron temperature; (c) potential, for He at pa = 4.2×10^{-2} Torr cm and at various magnetic field values.

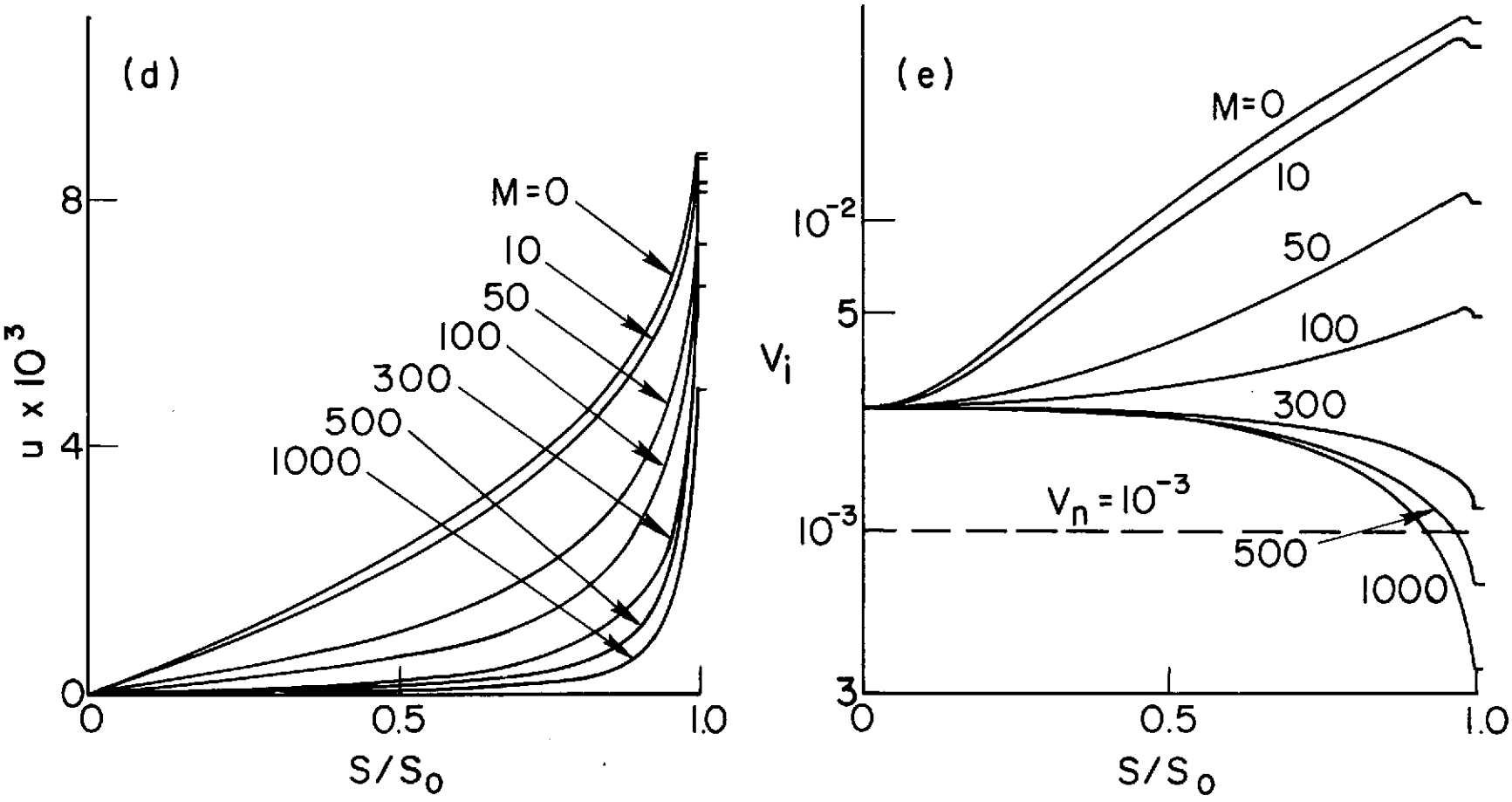

FIG. 2.8. The radial variations of normalized values of (d) ambipolar radial velocity; and (e) ion temperature, for He at pa = 4.2×10^{-2} Torr cm and at various magnetic field values.

$d^2W/ds^2 > 0$ at $s = 0$ in the Taylor expansion of Eq. (2.13). This flattening of potential has been observed by Bickerton and von Engel[28] as magnetic field is increased. The variation of ion temperature with magnetic field in Fig. 2.8(e) resembles the result of Self[20] obtained for the radial component of the ion pressure tensor. No quantitative comparison is possible, however, since Self takes $T_n = \nu_i = 0$ in his model. The change of sign in the slope of the ion temperature is related to the potential inversion, as may be seen by comparing Figs. 2.8(c) and 2.8(e): when the radial electric field changes sign, the ions are no longer attracted to the wall, but actually give up energy as they move to the wall against the radial electric field.

The value of the ion temperature on axis has a strong influence on the magnetic field value at which the potential starts to increase radially. This may be deduced from the Taylor expansions of the momentum and energy equations which connect together the second derivatives of electron temperature, potential, and ion temperature on axis [expansions of Eqs. (2.11)-(2.14)], with the second derivative of the density variation on axis. A more direct way is to assume uniform ion temperature and vary it as an input parameter. In this way, it is seen that as ion temperature is increased, the potential inversion sets in for progressively lower magnetic fields, with the negative radial electric field becoming progressively stronger. For example, it is possible to obtain negative radial fields of the order of several volts per centimeter with $T_{i0}/T_{e0} \sim 0.1$. This may be important for intense, low-pressure, hollow cathode arcs in a strong magnetic field, in which such strong negative radial electric fields have been observed.[11,18] Our theory implies that the ions in such arcs are very energetic with respect to the neutrals (see Sections 4 and 5).

The radial variation of electron temperature in Fig. 2.8(c) indicates that there is very little change as the magnetic field is increased. The radial profile becomes flatter near the axis, and the drop in temperature becomes somewhat steeper near the wall, as the magnetic field is increased at constant pressure.

Finally, it may be noted that all curves with $M \neq 0$ tend to the curve with $M = 0$ at very low pressures in Figs. 2.5 and 2.7. This may be explained by noting that as the pressure is decreased along a curve of constant M, the magnetic field also has to decrease. Thus, even for very high values of M at low pressures, the magnetic field tends to be very low; conversely, at high pressures, even small values of M may describe substantial magnetic fields.

2.4. Discussion

2.4.1. Limitations of the model

Fluid equations average out the detailed distribution functions of electrons and ions, and cannot be accurate when the scale lengths of the variables are comparable to the mean free paths of the charged particles. On the other hand, the results of measurements by probes also represent averages of detailed dynamics of charged particles, and typically indicate Maxwellian or near-Maxwellian electrons within the pressure range of this theory.[14] Since this theory is meant to explain the results of experiments, we feel justified in using the fluid approach. A kinetic treatment along similar lines would be much more complicated.

We have introduced some approximations in the fluid equations in order to simplify the analysis, but also because we do not know of any calculations of the transport coefficients for a weakly ionized plasma, which would be as precise and as detailed as the corresponding calculations for a fully ionized plasma.[22] We investigate now the consequences of these approximations for He, Hg and Ar, in the pressure range where we expect our theory to be valid.

In approximating the pressure tensors by scalars, we have assumed nearly isotropic distributions of electrons and ions. This is to be expected if the drift velocities are considerably smaller than the thermal velocities in the discharge. Comparison of Figs. 2.6(c) and 2.6(d) shows this to be true for electrons in all cases, while Figs. 2.6(e) and 2.6(d) demonstrate the inapplicability of using the ion scalar pressure near the boundary. This problem is resolved by Self,[20] who calculates the elements of the ion pressure tensor, and obtains results very similar to our Figs. 2.8(c)-(e), as discussed above.

By using the adiabatic assumption for the electrons, we have neglected the radial component of $\underline{Q}$ with respect to $(5/2)n\, v_r T_e$, to get Eq. (2.3). Since a precise expression for $\underline{Q}$ for our conditions is not available, we use the result of gas kinetic theory for heat transfer in a collisional regime,[22,30,31]

$$\underline{Q} = -\kappa \nabla T \ , \qquad \kappa = \frac{nT}{m\nu} \ . \tag{2.23}$$

At the high-pressure limit of our theory, with $pa = 0.57$ Torr cm, $p = 1$ Torr, and midway between the axis and the radial wall [see Fig. 2.6(d)], dT_e/dr must be 0.3 eV/cm or greater, for the heat flux term to become equal to or larger than the $(5/2)nv_rT$ term. Thus, the approximation $\nabla \cdot \underline{Q} = 0$ implies a small temperature gradient, and is marginally satisfied at the high-pressure limit of our theory [see Fig. 2.6(c)]. As the pressure is decreased, Eq. (2.23) no longer holds, and the thermal conductivity coefficient, κ, decreases, due to marginally-collisional conditions,[30] so that the heat flux may be neglected. Furthermore, the presence of magnetic field decreases κ by a factor $M^2 (M^2 \gg 1)$, reducing the heat flux even further. Similar consideration of the ion heat flux shows it to be negligible under all experimental conditions.

There is ample experimental evidence available to show that the electron drift velocities in He and Hg are proportional to E_z/p in a wide range of E_z/p values, which justifies the approximation of ν_e independent of velocity.[24,25] For Ar, however, experimental results show that this is not the case, and even very small amounts of impurities significantly change the dependence of v_{De} on E_z/p .[24] In the case of ions, the situation is more complicated, due to the deviations of the ion distribution function from Maxwellian in the low-pressure regime. As we have already concluded above, the present model of ion motion must be viewed with caution. However, the existing experimental results on ions in the positive column are insufficient to enable us to treat the ions differently.

The neglect of radiation losses in the energy equations is justifiable at very low pressures, where electrons obtain large drift

velocities between two successive collisions, so that a large percentage of the collisions are ionizing. This is especially true in He, where the first excitation level (19.8 eV) is relatively close to the ionization potential (24.5 eV).[25] A derivation of the similarity laws for He, which includes the radiation loss, gives results which are very similar to our Figs. 2.3, 2.4 and 2.5,[27] so that we do not consider it necessary to include radiation loss in analyzing He in our range of pressures. On the other hand, Hg and Ar have excitation levels which are relatively much lower with respect to the ionization level than in the case of He,[25] so that radiation and multi-stage ionization processes should be important in the pressure range which our theory considers for these two gases. A derivation of similarity laws, including radiation processes, for an isothermal and uniform positive column in Hg shows this to be true,[26] since the agreement with experiment is better than that demonstrated in our Figs. 2.3, 2.4 and 2.5 for Hg. Forrest and Franklin[32] discuss the relative importance of single- and multi-stage ionization processes, and conclude that the multi-stage processes become increasingly important as pressure is raised. Similar arguments apply to Ar.

2.4.2. Comparison with experiments

In conclusion, we have derived the radial profiles of electron and ion temperatures in the positive column, and have shown that the profiles of radial velocity, density, and potential are consistent with results of two-moment theories. In addition, the electron energy equation has enabled us to derive similarity laws for a positive column.

It is felt that the agreement with experiment demonstrated for He is very satisfactory over a wide range of pressures. The discrepancy at high pressures in Fig. 2.5 may be attributed to the neglect of radiation losses and heat conduction losses.

The discrepancies between theory and experiment for Hg and Ar are not serious for the calculation of electron temperature (Figs. 2.2 and 2.3), probably because small changes in temperature effect large changes in ionization frequency, Eq. (2.7). However, the large discrepancies in Figs. 2.4 and 2.5 indicate that the basic elementary processes are not sufficiently precisely described by our model for Hg and Ar. In the

case of Hg, the process of multi-stage ionization effectively decreases the ionization potential, and increases the ionization frequency. It follows from Eq. (2.16) that V_{e0} will decrease, and the agreement with experimental data will improve. It would seem that in addition to the inclusion of radiative processes, it is necessary, for Ar, to take account of the dependence of ν_{De} on E_z/p which is not linear, due in part to the presence of a strong Ramsauer effect.[25] However, there are not sufficient experimental data to model $\nu_{De}(E_z/p)$ in a wide enough range of E_z/p values with satisfactory accuracy.

It is impractical to extend our theory in its present form to higher pressures by including heat conduction, heat convection, and radiative processes, due to computational difficulties. It may be possible, however, to develop such a comprehensive theory without magnetic field by using our approach, together with a numerical method for solving Eq. (2.15) which would converge better at high pressures than the present one, or by extending the high-pressure ambipolar diffusion theory.

The comparison of theory with experiment is further restricted by the presence of instabilities, which may saturate at a high enough level to affect the steady state. Current-driven ion-acoustic turbulence is often present in the positive column (see Section 3), while at high pressures ($p > 0.6$ Torr in case of He[27]), striations occur and produce local changes in T_e and in the ionization rate.[14,31] The presence of a magnetic field introduces additional destabilizing effects, resulting in the excitation of numerous additional instabilities.[4,29,33] In the case of the drift instability, for example, the radial diffusion rate increases.[34]

3. ION ACOUSTIC INSTABILITY ON THE POSITIVE COLUMN

The instabilities of the positive column in a magnetic field may be classified into two basic types: macroscopic and microscopic.[7] Macroscopic instabilities are described by fluid equations, and are the subject of extensive theoretical and experimental work reported in the literature.[4,31,33,34] This section deals with another type of wave, a microscopic instability occurring in the positive column in the absence of magnetic field. It is driven by the deviation of the electron distribution function from a local Maxwellian which results from the presence of the applied electric field and associated current which maintains the positive column (see Section 2). Since fluid equations do not consider the details of the distribution function, they predict damped ion acoustic waves for typical positive column conditions.[33] Consequently, kinetic equations must be used to describe the observed excitation characteristics of the ion acoustic instability on the positive column.

Early investigations of this instability studied the transition from the unstable to the stable régimes (the instability boundary) for a collisionless model.[35,36] Subsequently, it was shown that although electron-neutral collisions are negligible, ion-neutral collisions are important for determining the instability boundary.[37-39] Measurements made on self-excited,[35-37,39,40] and on externally-excited waves,[36] yield the predicted values of wavelength, and the instability boundary.[39,40] The phase velocity of the waves in the long wavelength ($k\lambda_D \ll 1$), low frequency ($\omega \ll \omega_{pi}$) limit is equal to the ion sound speed; hence the name of the wave.

A comprehensive analysis of the excitation of ion acoustic instability in a helium positive column has appeared recently.[40] The model includes collisions of electrons and ions with neutrals in the linearized kinetic equations through a BGK-type collision integral.[41] The resulting dispersion relation is analyzed in the approximation of negligible electron-neutral collisions, zero ion drift, and negligible ion Landau damping ($T_i \to 0$), and it is shown experimentally that the observed saturated frequency spectrum displays a maximum where the linear spatial growth rate maximizes.

The present work extends the study of the above dispersion relation, and shows that the instability is convective for typical positive column conditions. It is further shown that under typical experimental conditions the ion Landau damping is not negligible. The full dispersion relation is solved numerically to obtain the variation of the spatial growth rate with frequency and with ion temperature. Comparison is made with frequency spectra measured on positive columns in helium and argon.

The linear theory is presented in Section 3.1., the experimental details in Section 3.2., and the comparison between them in Section 3.3. The chapter closes with a discussion of nonlinear theories which deal with the ion acoustic instability, in Section 3.4.

3.1. Linear Theory of Ion Acoustic Instability in a Weakly Ionized Plasma

Consider a uniform, infinite, isothermal, weakly ionized plasma immersed in a uniform field, E_z. The evolutions in time of the electron and ion velocity distribution functions are described by Boltzmann equations with BGK collision terms. These have the property of preserving the local number density of particles, as well as their momentum and energy, in close binary elastic collisions.[37, 41] The linearized kinetic equations for electrons and ions, for propagation along the z-axis, and the Poisson equation, are[40]

$$\frac{\partial f_{1j}}{\partial t} + w \frac{\partial f_{1j}}{\partial z} + \frac{q_j E_1}{m_j} \frac{\partial f_{0j}}{\partial w} = - \nu_j \left(f_{1j} - \frac{n_{1j}}{n_{0j}} f_{0j} \right), \qquad (j = e,i) \ , \tag{3.1}$$

$$\frac{\partial E_1}{\partial z} = \frac{e}{\epsilon_0} (n_{1i} - n_{1e}) \ , \tag{3.2}$$

where $q_i = e$, $q_e = -e$; ν is the effective momentum transfer collision frequency for charged particle collisions with neutrals, and linearization is performed assuming that the perturbed quantities vary as exp i(ωt-kz).

The effect of the static electric field is included in the f_{0j} , which are assumed to be drifting Maxwellian functions,

$$f_{0j} = (n_{0j}/v_{tj})\pi^{-1/2} \exp\left[-(w-v_{Dj})^2/v_{tj}^2\right]. \qquad (3.3)$$

It is shown in Ref. 38 that Eq. (3.3) differs from a more exact result by terms of the order of $(v_{De}/v_{te})^2$, where $v_{Dj} = q_j E_z/m_j \nu_j$ and $v_{tj} = (2T_j/m_j)^{1/2}$. The ratio v_{De}/v_{te} is small ($\sim 10^{-1}$) under typical positive column conditions. Furthermore, it is shown in Ref. 40 that retaining the $(q_j E_z/m_j)(\partial f_{0j}/\partial v)$ terms, which are neglected in Eq. (3.1), introduces only a small correction to the dispersion relation. The effect is one of adding to v_t a small imaginary part which is proportional to E_z. The consequence of the additional terms is to effectively reduce ν_i, and thus cause the spatial growth rate of the instability to be slightly larger (by about 10% under typical positive column conditions).[40]

The kinetic equations are next solved for n_{1j}, using the relation

$$n_{1j} = \int f_{1j}\, dw\,, \qquad (3.4)$$

resulting in

$$n_{1j} = \frac{-i\,\dfrac{q_j E_1}{T_j}\displaystyle\int\left(\frac{w-v_{Dj}}{\omega-i\nu_j-kw}\right)f_{0j}\, dw}{1 + i\,\dfrac{\nu_j}{n_{0j}}\displaystyle\int\frac{f_{0j}\, dw}{\omega-i\nu_j-kw}}\,. \qquad (3.5)$$

Combining Eqs. (3.2) and (3.4), we obtain the dispersion relation

$$D(\omega,k) = 1 + \frac{\omega_{pi}^2}{k^2 v_{ti}^2}\left[\frac{G'(\zeta_k)}{1 + i\,\dfrac{\nu_i}{kv_{ti}}\,G(\zeta_i)}\right] + \frac{\omega_{pe}^2}{k^2 v_{te}^2}\left[\frac{G'(\zeta_e)}{1 + \dfrac{i\,\nu_e}{kv_{te}}\,G(\zeta_e)}\right] = 0\,, \qquad (3.6)$$

where

$$\omega_{pj}^2 = e^2 n_{0j}/m_j \epsilon_0 \ , \ \zeta_j = (\Omega_j - i\,\nu_j)/k\,v_{tj}, \ \Omega_j = \omega - kv_{Dj} \ ,$$

$$G(\zeta) = \pi^{-1/2} \int_C \frac{\exp(-\xi^2)}{\zeta - \xi}\, d\xi \ . \qquad (3.7)$$

Here, C is the Landau contour of integration, and $G'(\zeta)$ is the derivative of G with respect to the argument. The contour C is the real axis if $\mathrm{Im}[\zeta] < 0$, and the real axis indented above $\xi = \zeta$, if $\mathrm{Im}[\zeta] \geq 0$.[41]

Relation (3.6) is the dispersion relation which was analyzed in the collisionless approximation in Refs. 35 and 36, and with the inclusion of ion-neutral collisions in the ion rest frame, neglecting ion Landau damping terms, in Refs. 37-40.

3.1.1. The approximate dispersion relation

In the range of experimental interest for the positive column, the ion acoustic wave phase velocity is roughly equal to the ion sound speed, $\omega/k \simeq v_s \ [= (T_e/m_i)^{1/2}]$. As noted in Ref. 40, the following velocity ordering is established in the positive column: $v_{ti} \ll v_s \ll v_{De} \ll v_{te}$. This implies $\zeta_i \gg 1$, $\zeta_e \ll 1$, so that the functions G and G' in Eq. (3.5) may be approximated by the appropriate asymptotic and power series expansions.[41] When the exponential term (which introduces ion Landau damping) is neglected in the asymptotic expansions of $G(\zeta_i)$ and $G'(\zeta_i)$, Eq. (3.6) becomes

$$D(\omega,k) = 1 - \frac{\omega_{pi}^2}{\Omega_i(\Omega_i - i\nu_i)} + \frac{2\,\omega_{pe}^2}{k^2 v_{te}^2}\left\{1 - i\,\frac{\Omega_e}{kv_{te}}\left[\pi^{1/2} + (\pi-2)\,\frac{\nu_e}{kv_{te}}\right]\right\} . \qquad (3.8)$$

This relation, with the approximations of v_{Di}, $\nu_e = 0$, was shown to yield temporal growth when solved for real k in Refs. 37 to 39. Relation (3.8) may be solved for complex or real ω and k, where $k = k_r + ik_i$, $\omega = \omega_r + i\omega_i$, so that temporal growth implies $\omega_i < 0$, while spatial growth in the + z direction implies $k_i > 0$. Reference 40

considers both the solutions ω(k real) and k(ω real), and concludes that the latter are appropriate to the experiment, since the positions of the maxima of the observed frequency spectra agree better with the maxima of $k_i(\omega$ real) than with the minima of ω_i(k real).

The answer to the question of which solution of the dispersion relation is appropriate for describing the experimental situation is dictated by the physical conditions of the particular system. As discussed by Rognlien and Self,[42] special care is required in applying the dispersion relation to a bounded physical system. We take the point of view that the instability is a purely propagating wave, so that the stability criteria derived in Refs. 43 and 44 for an infinite system may be applied. This is justified by experimental data of Ref. 40, which show that the instability grows in space away from a grid which shorts out the wave, becomes saturated, and remains constant further down the tube.

The criterion of Briggs[43] consists in investigating the behavior of the complex maps of either ω(k) or k(ω), in the vicinity of certain special points. Once it is shown that unstable waves are possible, by showing that ω_i(k real) < 0 for some range of parameters, further study is required to determine whether the instability is convective or absolute. The significance of making the distinction between the two types of instabilities lies in the fact that the asymptotic time response to a delta-function perturbation localized in time and space approaches infinity at every point in the case of an absolute instability. A linear analysis is consequently inappropriate for describing the experiment, and some sort of nonlinear mechanism must be introduced to lead to saturation. In the case of a convective instability, however, the response to the delta-function excitation grows in space away from the source, while the asymptotic time response is zero at every point. Thus, a convective instability may describe the experimental situation of a signal excited by a grid at frequency ω and growing in space away from the grid, up to the point where the signal is so large that nonlinear effects must be introduced to lead to saturation. In this way, solutions k(ω real) will predict the spatial propagation characteristics of a wave close to the instability boundary.

Strictly speaking, the exact dispersion relation, Eq. (3.6), should be analyzed for instability by the criteria for warm plasmas in Ref. 44. However, this would present a formidable computational problem, due to the transcendental nature of that equation. Even the analysis of the polynomial approximation [Eq. (3.8)] must be done numerically. Consequently, we present an analysis of an approximation to Eq. (3.8), which has the property of being the least stable case, and it will be shown that the ion acoustic wave is indeed convectively unstable for typical experimental conditions.

Following Refs. 37-40, we consider the ion rest frame, taking $\nu_e \ll k\, v_{te}$, and $\omega/k \ll v_{De}$, which are valid for the positive column. The resulting dispersion relation,

$$D(\omega,k) = 1 - \frac{\omega_{pi}^2}{\omega(\omega - i\nu_i)} + \frac{2\,\omega_{pe}^2}{k^2 v_{te}^2}\left[1 + i\pi^{1/2}\frac{v_{de}}{v_{te}}\right] , \tag{3.9}$$

is easily analyzed according to the criteria described by Briggs.[43] Briefly, these state that an absolute instability exists if: (1) there is a saddle-point in the complex k-plane, formed by the merging of two poles which originated in opposite half-planes, as the Laplace contour is analytically continued from $\omega_i \to -\infty$ to the real ω axis; and (2) that the saddle-point corresponds to a value of ω with negative imaginary part, $\omega_{si} < 0$. If these conditions are not satisfied, the instability is convective.

The saddle points in the k plane are located by simultaneous solution of the equations

$$\frac{\partial D}{\partial k} = 0 , \qquad D = 0 . \tag{3.10}$$

The result for Eq. (3.9) is

$$|k_s| \to \infty , \qquad \omega_s = \pm \omega_{pi} \left(1 - \frac{\nu_i^2}{4\omega_{pi}^2}\right)^{1/2} + i \frac{\nu_i}{2} . \tag{3.11}$$

We see immediately that $\omega_{si} > 0$, and that the instability is convective, since Condition (2) above is not satisfied. Equation (3.11) shows that the ion-neutral collisions are stabilizing. The electron-neutral collisions make the wave slightly less stable, as is shown by numerical results of the next subsection. This may also be seen from Eq. (3.8), where ν_e and the Landau growth terms are of the same sign.

Equation (3.9) does not contain the ion Landau damping of the instability, but has the electron drift term, which causes instability. Furthermore, the approximations used in deriving Eq. (3.9) are consistent with (3.11). Thus, since the main destabilizing effect is retained in Eq. (3.9), while some stabilizing effects are neglected, it follows that the convective instability of Eq. (3.9) implies the same type of instability for Eq. (3.6).

To show explicitly the destabilizing effect of the electron drift velocity, let us neglect all collisions, while retaining the full Ω_e term in Eq. (3.8). It may then be shown that

$$\mathrm{Im}\left[\omega_s^2\right] \sim \left[3 - \pi \left(\frac{v_{De}}{v_{te}}\right)^2\right], \tag{3.12}$$

which implies that when $v_{De}/v_{te} = (3/\pi)^{1/2} \sim 1$, ω_{si} crosses the real axis. While this by itself does not imply absolute instability, because more study is essential to demonstrate that Condition (1) is satisfied, it confirms that the electron drift velocity is a destabilizing effect. We should note that $v_{De}/v_{te} \lesssim 0.2$ for typical positive column conditions.

3.1.2. The exact dispersion relation

The approximate dispersion relation, Eq. (3.8), may be used to predict the frequency in the ion rest frame at which the spatial growth rate, k_i , maximizes, but it is not useful for calculating

$k_i(\omega)$ in the laboratory frame. This follows from the fact that as ω is increased from zero, the Doppler shift term, $k_r v_{Di}$, increases more rapidly than ω (see Fig. 3.1.). Consequently, the Re [Eq. (3.8)] = 0 [Eq. (3.13)], which is used for calculating k_r, becomes a divergent expression for $\omega/\omega_{pi} \to 1$, $k_r\lambda_D \gtrsim 1$, where $\lambda_D = (T_e\epsilon_0/ne^2)^{1/2}$ is the electron Debye length. This is often the range of frequencies where k_i maximizes, so that Eq. (3.8) cannot be used for mapping the full range of $k_i(\omega)$, when $v_{Di} \neq 0$. In addition, the asymptotic expansion of the ion part of Eq. (3.6), used in deriving Eq. (3.8), neglects the important effect of ion Landau damping, which depends on the temperature ratio T_e/T_i.

In order to compare experimentally measured frequency spectra [see Section (3.2)] with the linear growth rates, it is necessary to solve Eq. (3.6) exactly, for k complex and ω real. In doing so, we note that $G(-\zeta) \equiv Z(\zeta)$, where $Z(\zeta)$ is the well known plasma dispersion function,[41] applicable when the convention $\exp[-i(\omega t-kz)]$ is used for the perturbed variables, and solve for $Z(\zeta)$ by numerical methods, outlined in the Appendix of Ref. 45. Equation (3.6) is solved by assigning the value of one of the two complex arguments, and generating the corresponding value of the other complex argument, by a numerical iteration procedure, so that $D(\omega,k) = 0$ holds.

The unstable ion acoustic wave propagates in the direction of the electron drift, and we take E_z to be in the -z direction, to get growing wave propagation in the + z direction (the wave propagating in the opposite direction is found to be strongly damped). Utilizing the results of Section 2 for the relevant steady-state parameters of a helium positive column, we find that the numerical solutions indicate increasing spatial growth ($k_i > 0$), as the discharge current is increased, or the pressure decreased. This is consistent with the results of Section 3.1.1. Figure 3.1 shows the dispersion relation, $k_r(\omega)$, for three values of the pa product (the dependence of normalized variables, $k_r\lambda_D(\omega/\omega_{pi})$, on current at a fixed pressure is very slight), together with the approximate relation,

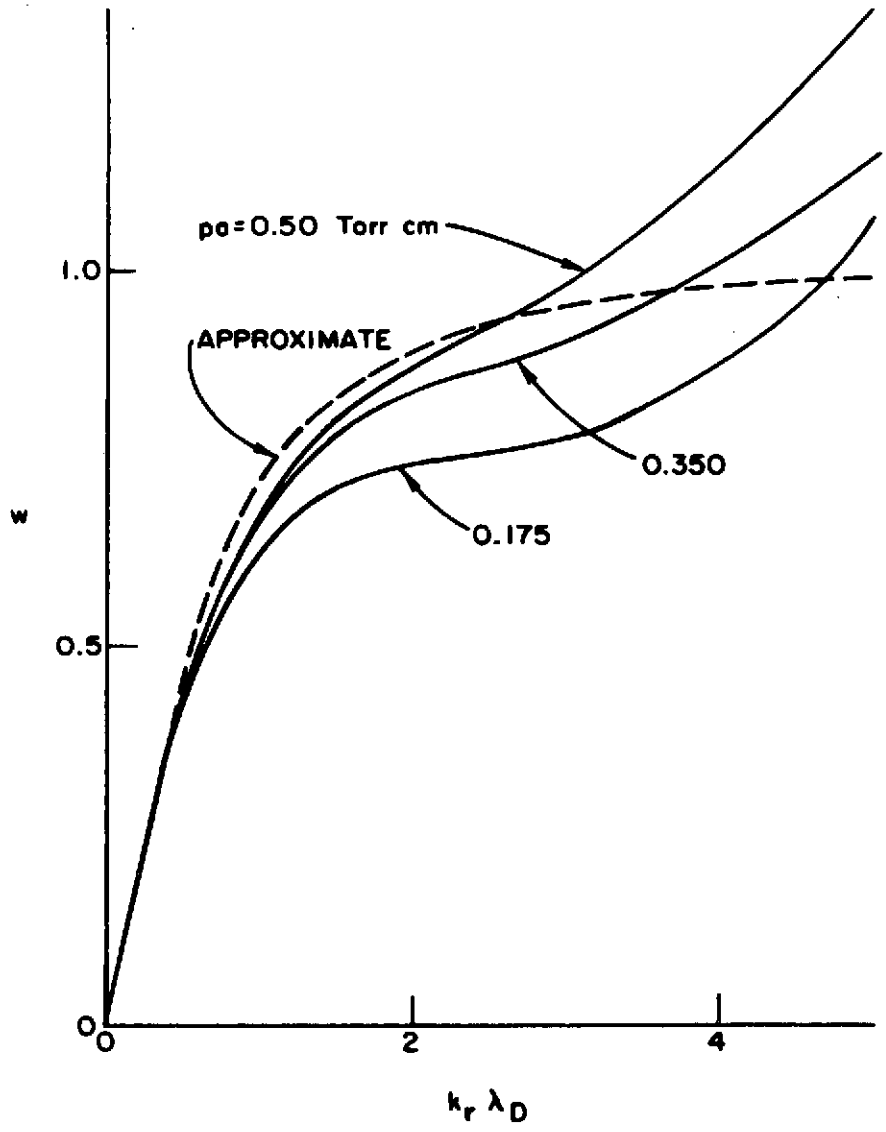

FIG. 3.1. The solution $k_r(\omega$ real) of Eq. (3.6) for He and various values of pa product. The broken line represents Eq. (3.13); $w \equiv \omega/\omega_{pi}$.

$$\frac{\omega}{\omega_{pi}} = \frac{k_r\lambda_D}{\left[1 + (k_r\lambda_D)^2\right]^{1/2}} \quad , \tag{3.13}$$

obtained from $Re[D] = 0$ in Eq. (3.9), with $\nu_i \ll \omega$. The approximation is seen to become progressively worse as $k_r\lambda_D$ increases. The calculated variation of the spatial growth rate with frequency is shown in Fig. 3.2. It is seen that as the current is raised at constant pressure, the frequency range of instability is increased, and the most unstable frequency also increases.

Figure 3.3 shows the stabilizing effect of increasing the ion temperature. The stabilization is caused by collisionless (Landau) damping of the wave, which interacts with an increasing number of particles in the tail of the ion distribution function as the ion temperature rises. Note that Eq. (3.8) does not depend on T_i, and consequently does not contain the ion Landau damping.

3.2. Experimental Results

3.2.1. Apparatus and steady-state diagnostics

The experiment is carried out using a continuously pumped Pyrex tube, 5 cm I.D. and about 1 m long, the exact length of the discharge depending on the position of the movable anode (see Fig. 3.4). The plane cathode is an indirectly-heated oxide-coated cylinder, 2.5 cm in diameter. It was found that the standard mixture containing carbonates of alkali metals painted onto a nickel substrate performs much better, and is much less susceptible to poisoning, than a commerical dispenser-type cathode consisting of porous tungsten impregnated with barium oxide. The helium gas is leaked in from the cathode end, next to the throttled pumping station, consisting of an oil diffusion pump with a liquid nitrogen trap. The base pressure of the system is about 10^{-6} Torr. Discharge current is varied from 0 - 10 A.

The pressure in the system is monitored by an ionization gauge and a Pirani gauge at each end of the tube. A long shielded probe, enclosed in glass, is inserted along the bottom of the tube, through a Wilson seal at the anode flange, and is used to measure discharge characteristics

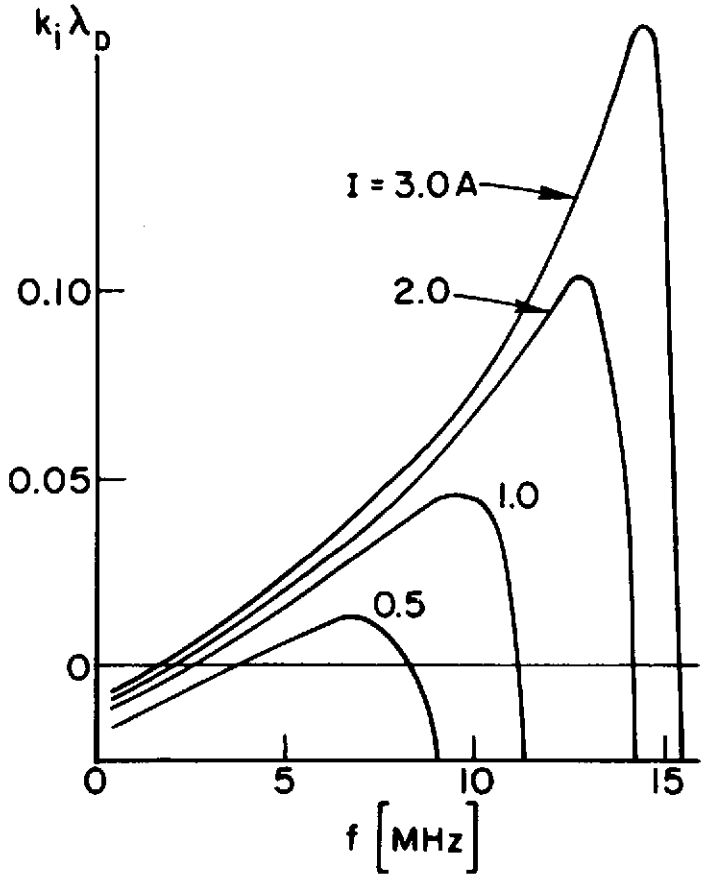

FIG. 3.2. The solution k_i(ω real) of Eq. (3.6) for pa = 0.25 Torr cm, T_i = 0.1 eV and various values of discharge current in He.

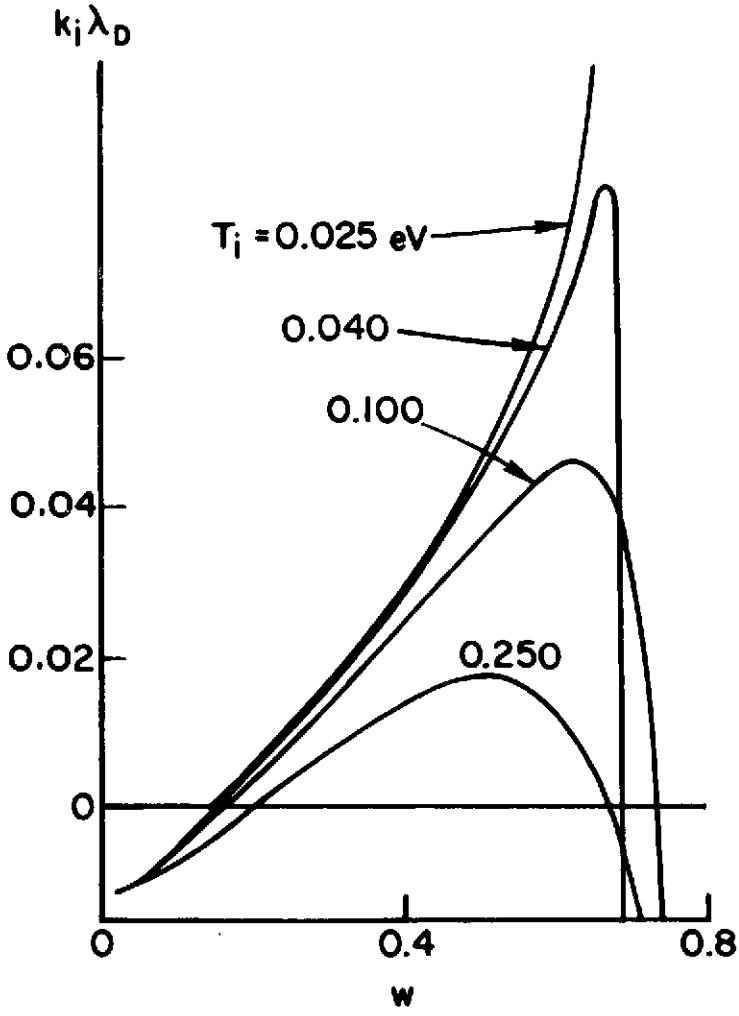

FIG. 3.3. The influence of ion temperature on the normalized spatial growth rate calculated from Eq. (3.6); pa = 0.25 Torr cm, I = 1 A, $w \equiv \omega/\omega_{pi}$ in He.

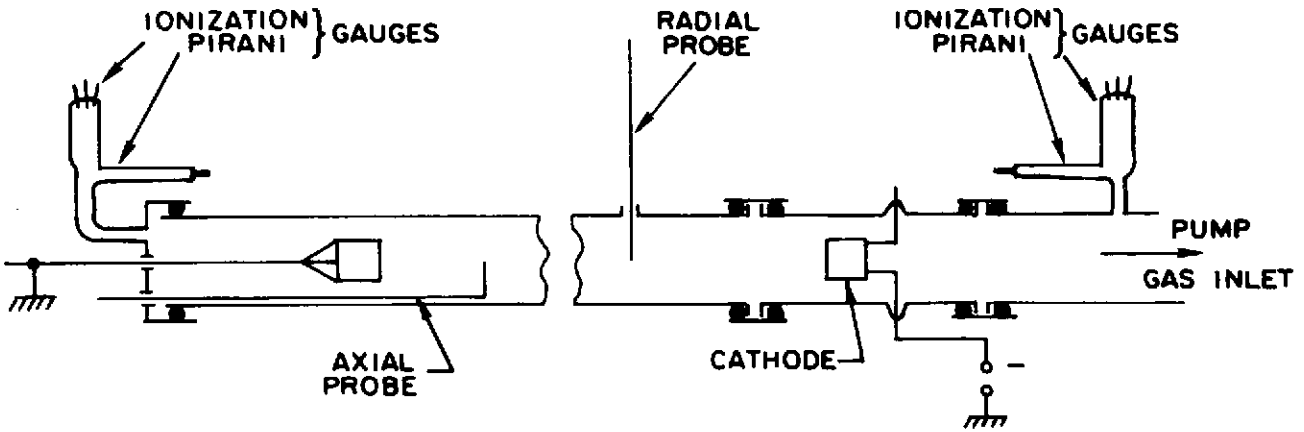

FIG. 3.4. Sketch of the positive column experiment.

along the whole length of the system. It ends with a 3 mm long, 0.4 mm diameter cylindrical tungsten tip, which is normally located on axis, but may be used to sample all radial positions by rotating the probe body. A radially movable probe is located at a fixed axial position 30 cm from the cathode, and can accommodate cylindrical, plane, or double probe tips, used for the various types of measurements.

The discharge tube is cooled by water circulating through a jacket surrounding the tube (not shown in Fig. 3.4). This is important for the region around the cathode (the cathode absorbs about 70 W of heating power) and for the whole tube when it runs at high currents (> 3A for He and > 6A for Ar, since E_z is lower in Ar).

Certain low-frequency ($\sim$ 1 MHz in He) noise with wavelength of the order of the discharge length is excited near the cathode. This noise obstructs the detection of the low-level ion acoustic instability (near the instability boundary) under certain discharge conditions in He. It may be suppressed by applying a local magnetic field of several tens of gauss to the cathode region. Consequently, a magnetic field, generated by a solenoid wound around the cathode region, was used during some measurements of the instability boundary.

A cylindrical microwave cavity, 30 cm long and 23 cm in diameter, operating in the TM_{010} mode,[46] is used in conjunction with a swept frequency generator for measuring mean electron density. The cavity does not fit around the water jacket, and comparisons of microwave cavity and Langmuir probe measurements can be made only when the water jacket is removed and the cavity installed.

On the basis of the theory of Section 2, curves of $\bar{n}/n(0)$ were calculated (see Fig. 3.5), where the mean density

$$\bar{n} = \frac{2}{a^2}\int_0^a r\, n(r)\, dr \,, \tag{3.14}$$

is evaluated numerically in the course of integrating Eq. (2.15).

Langmuir probe data were analyzed by using the theory of Laframboise for a cylindrical probe, including the correction due to finite λ_D with

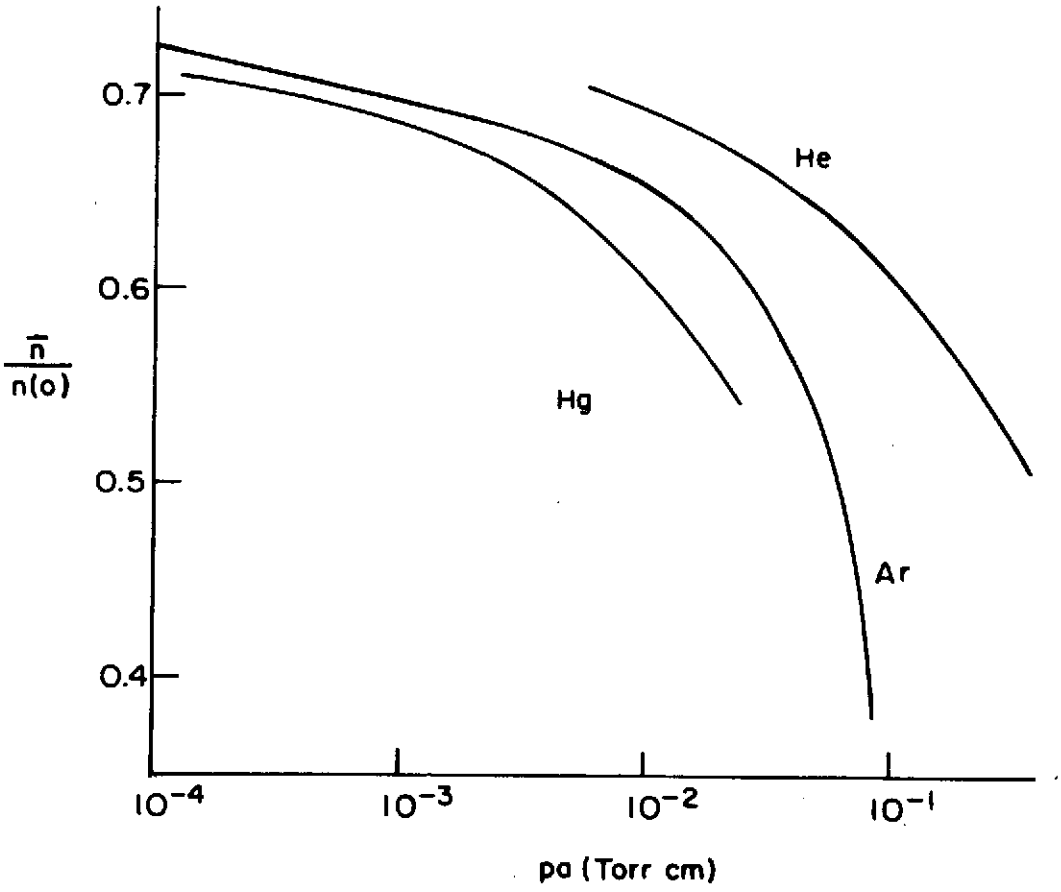

FIG. 3.5. The ratio of mean electron density to density on axis, calculated from Eq. (3.14) and used for comparing microwave and probe measurements.

respect to probe radius.[47] The density was determined from the ion saturation current drawn by the probe, while electron temperature was deduced from the slope of the electron collecting part of the characteristic drawn to a semi-logarithmic scale.[47,48] Plasma density data obtained from microwave cavity measurements ($\bar{n}$) and from probes on axis [n(0)] agree within experimental error (typically 10 - 20%) when the correction of Fig. 3.5 is employed. Electron temperature data obtained from probes agree so closely with Fig. 2.3, that theoretical temperature data are used in calculating the dispersion relation, Eq. (3.6).

The theory of Section 2 does not take into account the variations of steady-state parameters with discharge current. This is a good approximation for T_e. However, since the ion acoustic instability is especially sensitive to the exact value of v_{De}, Eq. (2.11) is not sufficiently precise. Instead, a mean value of electron drift velocity is obtained from

$$\bar{v}_{De} = \frac{J}{e\,\bar{n}} \quad , \tag{3.15}$$

and is found to increase slightly with current. This value is substituted into Eq. (3.6) in order to compare the observed spectra with theoretical predictions.

3.2.2. Observations of ion acoustic waves

The self-excited signals from the probes are displayed on a spectrum analyzer, and it is noted that for a particular pressure there is a certain value of discharge current above which the waves are excited. For maximum detected signal,[49] the detecting probe is biased near electron saturation, when the sheath around the probe practically disappears, and electron current fluctuations through a 100 Ω biasing resistor are monitored. It is noted that the instability is maximum on axis, and decreases radially. When a plane detecting probe is used, the signal maximizes sharply when the probe is oriented to face the cathode at all radial positions. This implies that the waves are essentially plane waves propagating in the direction from the cathode to the anode.

Most of the observations were made in He. The computed theoretical curves in Figs. 3.1 - 3.3 also refer to He. Some measurements made in Ar will be described at the end of this section.

Measurements in He: Measurements of the phase difference between the fixed radial probe and the moving axial probe indicate wavelengths of the order of 1 mm in He, with phase velocity equal to the ion sound speed, v_s . Measurements are performed with a tunable phase-meter, and indicate no radial phase shift. The measured phase velocity agrees with the long wavelength limit of Fig. 3.1. Results of calculations for ion acoustic wave propagation in cylindrical geometry by Woods[50] also predict this low frequency limit. Together with the radial decrease of the wave, this points to the possible presence of a finite transverse wavenumber at low frequencies.

The experimental frequency spectra are drawn on a logarithmic scale in order to make all of the spectra fit on a single diagram, Fig. 3.6. Figure 3.2 was calculated for the dc discharge parameters measured when Fig. 3.6 was taken, so that direct comparison of the two is intended. The ion temperature was taken to be 0.1 eV (see Fig. 3.3), which is about 4 T_n , in order to obtain best agreement with Fig. 3.6. This is consistent with the results of Section 2 [see Fig. 2.6(e)], as well as with the studies of the dependence of the stability boundary, $\mathrm{Im}[D] = 0$, on the ratio T_e/T_i in the collisionless approximation.[35]

In order to compare the shapes of the observed and the calculated spectra, the curves of Fig. 3.2 are displayed on a logarithmic scale, for $k_r\lambda_D \geq 0.005$, in Fig. 3.7. The curves are also displaced vertically by 10 dB, to conform to those of Fig. 3.6.

It was also noted that increasing the pressure had a stabilizing effect on the instability, the upper limit being set by the appearance of striations,[14] at about 200 mTorr in He. The lower pressure limit was set by the discharge being extinguished at about 20 mTorr, with strong cathode-generated noise just above that. Clearly defined instability, as in Fig. 3.6, appears between about 70 and 150 mTorr.

Figure 3.6 shows that, as the current is increased, the observed instability spectra become broader, and the maxima increase in frequency. This agrees with the result of linear theory, which predicts maximum

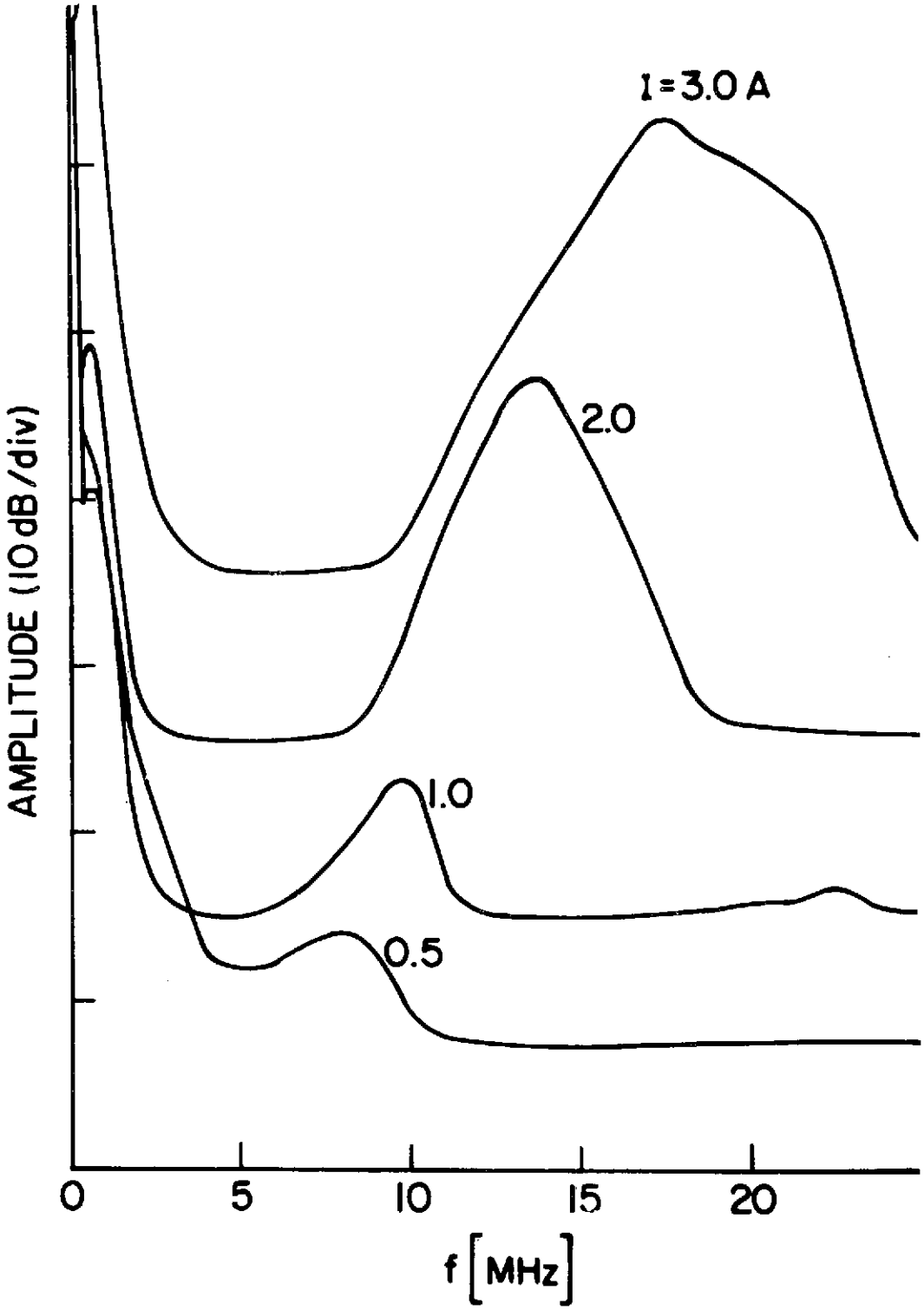

FIG. 3.6. Experimental frequency spectra for various discharge currents. Log reference is displaced vertically 10 dB for each curve; pa = 0.25 Torr cm in He.

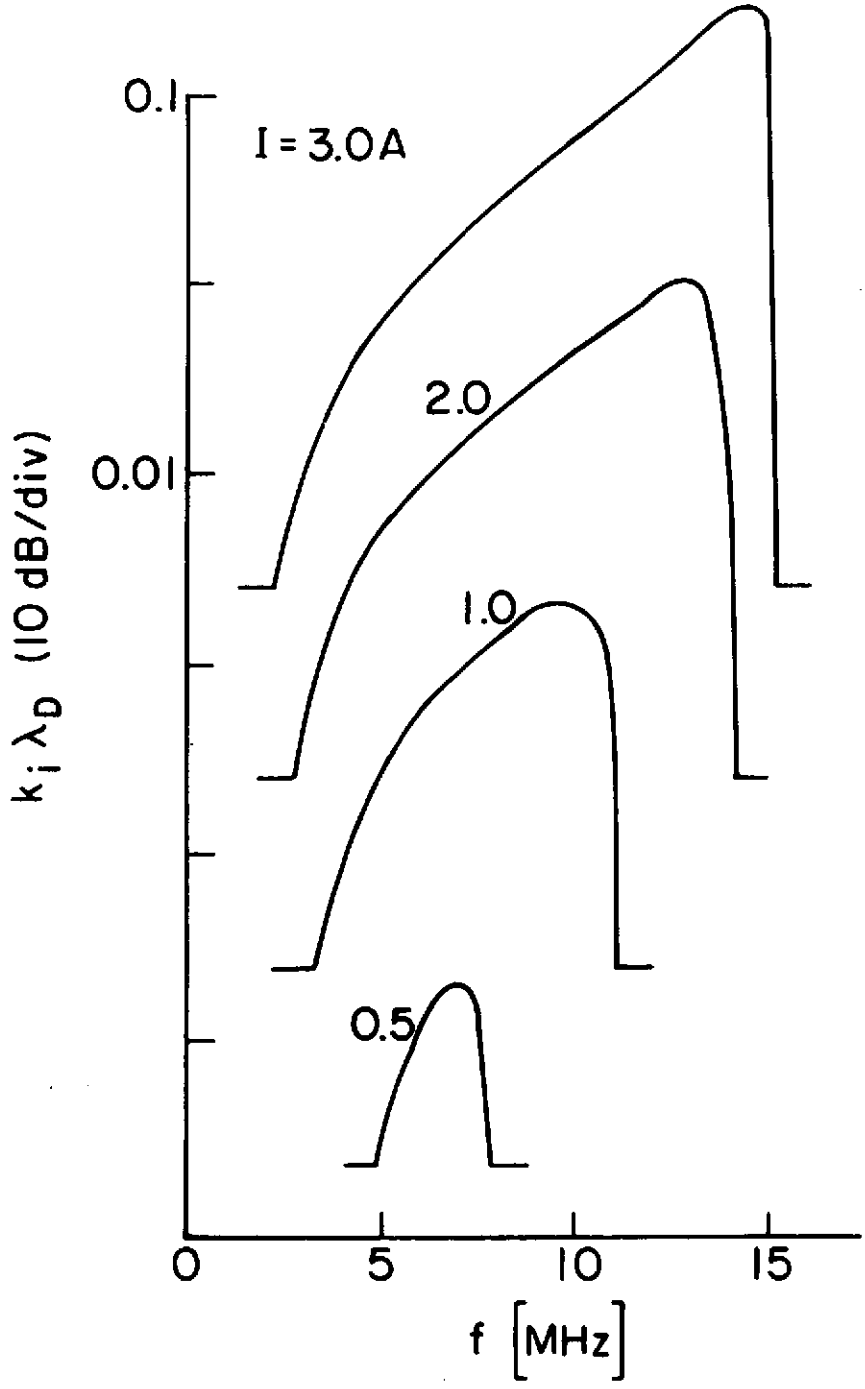

FIG. 3.7. Growth rates of Fig. 3.2 redrawn to logarithmic scale for $k_i\lambda_D \geq 0.005$. Log reference is displaced vertically 10 dB for each curve; the marked values of the ordinate refer to the I = 3 A curve.

spatial growth when $\omega = \omega_{pi}/3^{1/2}$.[40] Similar trends are observed for decrease of pressure. Very low pressure (< 70 mTorr in He) or very high current (~ 5 A at 0.1 Torr) cause the observed spectra to spread out, and no well-defined upper and lower cut-off frequencies are observed. The destabilizing effect of the electron drift becomes so large that one should expect an increasing departure between the saturated spectrum and the linear growth rate. A discussion of nonlinear effects is presented in Section 3.4.

The observed amplitude of current fluctuations through the probe biasing resistor is about 0.1 μA, which corresponds to a few millivolts of potential fluctuations in the plasma, when the probe impedance is taken into account (~ 30 kΩ). The ratio of fluctuating to steady-state electron probe current ranges from 0.01 - 0.1% in He.

The low-frequency instability in Fig. 3.6 is the cathode-generated noise. It has long wavelength compared to the tube length, and is affected by the application of a magnetic field of a few tens of gauss to the cathode region,[51] as pointed out in Section 3.2.1.

Measurements in Ar: Data in argon were taken in the pressure range of ~ 1 - 10 mTorr. The results follow qualitatively those for He, except that the detected signal level is higher in Ar (the ratio of fluctuating to steady electron probe current is typically 0.1 to 1%). This may be related to a smaller value of collisional damping, evidenced by the lower value of ν_i in Ar than in He, for the typical pressure ranges of operation (see Table 2.1).

Figure 3.8 shows frequency spectra detected in Ar. The spectra closely resemble those in Fig. 3.6, except that the maxima are located at lower frequencies than in He. This is because ω_{pi} is lower in Ar, due to the heavier ions, and there is also somewhat lower n under the conditions shown.

The considerable spreading of the spectra at 4 and 8 A in Ar is similar to the spreading of the 3 A curve in He. It is observed that the instability spectra at high currents (see Figs. 3.6 and 3.8) saturate in amplitude, so that further increase of current causes broadening of the instability, and, in some cases, breaking up of the main peak into

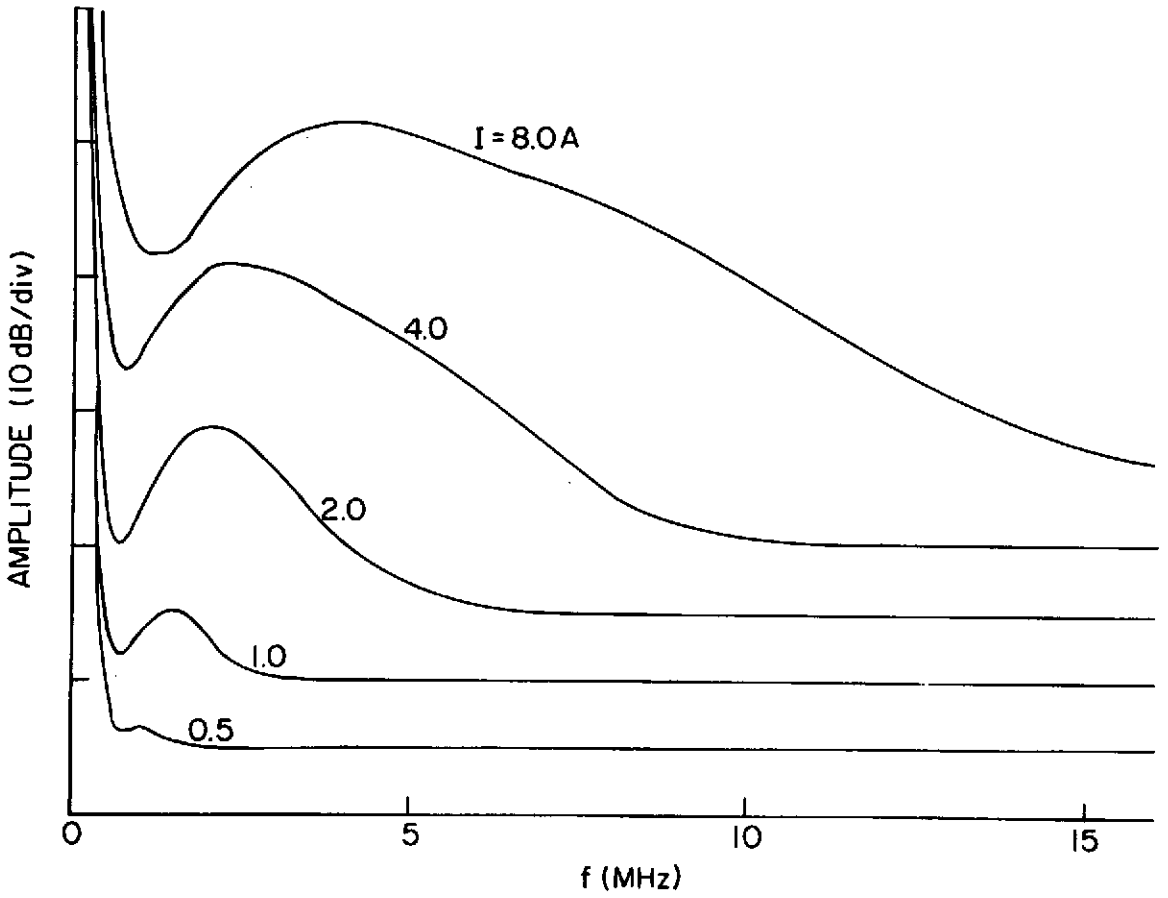

FIG. 3.8. Experimental frequency spectra for various discharge currents. Log reference is displaced vertically 5 dB for each curve; pa = 5×10^{-3} Torr cm in Ar.

two peaks. Thus, a mechanism exists which limits the amplitude of the wave, and it would be desirable to include it in the theory. This topic is discussed in Section 3.4.

3.3. Discussion of Experiment and Theory

The experimental results of Section 3.2 reproduce most of the data reported in Ref. 40 for He. In addition, measurements in Ar show the presence of the ion acoustic instability with qualitatively similar features to those measured in He. The relatively higher amplitude of the instability in Ar means that Ar may be more suitable than He for studying plasma heating due to the presence of ion acoustic instability.

The theory in Section 3.1 has shown that $k(\omega$ real) solutions describe properly the linear régime expressed by the dispersion relation formulated in Refs. 37, 38 and 40. Solution by numerical methods of the full dispersion relation, Eq. (3.6), has enabled the calculation of $k_r(\omega$ real) and $k_i(\omega$ real) to be made in the laboratory frame, which can be directly related to the observed spectra. Furthermore, by comparing the measured with the calculated spectra, it is concluded that ion Landau damping is important for typical positive column conditions, and that the ion temperature must be considerably higher than the neutral temperature for satisfactory agreement of theory and experiment.

Comparison of Figs. 3.6 and 3.7 shows that the positions of the maxima and the high cut-off frequencies are predicted by the theory. The agreement of theory and experiment at the high-frequency cut-off is a significant demonstration of the important role of ion Landau damping, because this type of collisionless damping is the dominant mechanism of wave energy loss at high frequencies (near ω_{pi}). The relatively poorer agreement at the low-frequency cut-off signifies that the collisional damping, which is the dominant loss mechanism at low frequencies, is not sufficient to account for the observed large damping at these frequencies.

As noted in Section 3.2.2., the ion acoustic wave is observed to propagate axially with a wavelength typically much smaller than the transverse dimensions of the discharge. It appears that the one-dimensional model of the linear theory, Section 3.1., should be a good approximation for describing the instability boundary. However, the

lack of success of the theory in predicting the low-frequency cut-off may indicate that there is an additional loss mechanism at low frequencies. This may result from the finite transverse dimensions of the discharge: as noted by Yamada,[40] the loss of particles to the wall represents an effective loss of energy, which is not contained in the model of an infinite plasma. Additionally, there may be effects due to finite transverse wavelength, as well as damping due to ion streaming and velocity spread in the radial direction, shown in Fig. 2.6(e). However, an extension of the theory of Section 3.1 to include the effects of finite transverse dimensions and also plasma inhomogeneity in the radial direction, would be very difficult.

In concluding this section, it is noted that many of the observed features in the linear régime of an ion acoustic wave on a positive column can be explained in terms of convective instability; it is driven by the inverse Landau effect due to the deviation of the electron velocity distribution from a local Maxwellian in the presence of an electric field. The observed spectra correlate well with calculated spatial growth rates; the destabilizing effect of electron drift, and the stabilizing effect of ion Landau damping, are clearly demonstrated for a positive column whose steady-steady characteristics are consistent with the results of Section 2.

3.4. Discussion of Nonlinear Effects

As noted in Section 1, nonlinear effects lead to saturation of linear instabilities at a level which may be so high with respect to the thermal level as to affect the steady-state characteristics of the plasma. Two basic types of nonlinear behavior appear, depending on the spectrum of wavelengths of the linear instability as compared to dimensions of the experimental system. In the case of a discrete spectrum, when one or a few low order eigenmodes are present, nonlinear saturation leads to single large amplitude waves. This is the case of macroscopic instabilities of the positive column in a magnetic field,[4,34] and also the flute instabilities discussed in Sections 4 and 5. These instabilities are often responsible for the enhanced diffusion of charged particles across magnetic field lines (Section 4.2.3.).

The second type of nonlinearly saturated spectrum appears when the linear instability has a continuous spectrum of high order (short wavelength) modes. The saturated spectrum in this case is said to be turbulent, and the resistance of the plasma may be enhanced (anomalous resistivity) due to collisions of electrons with the random potential fluctuations in the continuous spectrum of ion waves. This can lead to turbulent heating by the current-driven ion acoustic instability.

The physical situations and the corresponding mathematical descriptions are very different in the two cases. The first case involves the saturation of a single mode and possibly the interaction and competition among a few discrete modes. In the second case, there is coupling between the different parts of the spectrum, and energy flow through the spectrum; a major part of theory is to calculate the spectrum dependence on ω and k by using the random phase approximation.

The turbulent state of the current-driven ion acoustic instability has been the subject of several different theoretical descriptions,[52-55] depending on which basic nonlinear mechanism is assumed to lead to saturation. Various wave-particle and wave-wave interaction mechanisms have been proposed and the resulting turbulent spectra and saturated amplitudes have been calculated. However, the theoretical models often do not have much resemblance to the experimental situation. For example, they typically consider one-dimensional and collisionless plasmas, periodic boundary conditions, and the initial value problem, where either a drifting Maxwellian is assumed to exist at $t = 0$ or a voltage or electric field is applied at $t = 0$, and the time evolution of the instability is followed. Since the experiment is typically much more complicated than such theoretical models, it is not surprising that there is still no general consensus about the appropriate theory for a given experiment, or a satisfactory experimental confirmation of any theory. The question of which nonlinear effects are dominant and which are negligible for a given experiment is still open, and more experimental data, in conjunction with realistic theoretical models, are needed to answer it.

Kadomtsev,[52] Sagdeev and Galeev,[53] and Davidson[54] give comprehensive discussions of nonlinear plasma theory, with ion acoustic turbulence as a particular case. Plasma heating by ion acoustic turbulence is also reviewed as a special case of the general subject of turbulent heating by Self.[55] We present here a brief survey of recent papers, not covered in Self's review, dealing with the nonlinear state of ion acoustic instability.

3.4.1. Theory

The first description of the nonlinear state of the ion acoustic instability is based on the nonlinear kinetic equations in the approximation of weak turbulence (quasilinear theory), as discussed by Kadomtsev.[52] The saturation is due to nonlinear Landau damping on the ions, and the saturated spectrum of potential fluctuations is found to vary as ω^{-1}, k^{-3}. The energy flows from high to low values of ω and k, where it is dissipated by collisions.

The quasilinear approach has also been used to calculate the additional influence of effective electron collisions with ion waves, resulting in increased effective collision frequency and in anomalous resistivity.[53] Numerous other theories along similar lines have been developed, and are discussed in the review by Self.[55]

It has been found that the nonlinear Landau damping on ions is too weak a mechanism, so that the level of turbulence predicted by quasilinear theory is too high.[55] Consequently, other mechanisms which may lead to saturation have been studied recently, especially a variety of models of strong wave-particle interaction.

Rudakov and Tsytovich[56] generalize the weak turbulence, quasilinear theory of Kadomtsev[52] to include the effects of perturbation of particle orbits by the turbulent fields. For the special case of ion acoustic turbulence, the authors demonstrate that the quasilinear interaction is always more important than the strong interaction of the turbulent wave with electrons.

It was shown in Ref. 57 that electron trapping can also be responsible for saturating the ion acoustic instability. When the amplitude of the ion acoustic wave becomes large enough, electrons are trapped in potential

troughs of the wave. The effect becomes important when the bounce frequency exceeds the wave frequency and the electron collision frequency. The frequency spectrum in the saturated state is shown to vary as $\omega^{-7/3}$, $k^{-13/3}$.

Reference 58 considers the effect of ion trapping, i.e., the modification of ion orbits by finite amplitude waves. It is shown that the effect leads to saturation of the ion wave, and the level of saturation, but not the detailed dependence on ω and k , is calculated. The calculated value is shown to be of the same order of magnitude as the experimental value from Ref. 59.

Thus, even though ion and electron trapping effects can by themselves lead to saturation of the ion acoustic wave, it follows from the results of Ref. 56 that the quasilinear interaction is expected to be more important than strong wave-particle interaction with electrons. It should be emphasized that a proper theoretical treatment must consider the relative importance of all the possible nonlinear mechanisms for a particular experimental situation, and base the final model on the combination of those mechanisms which are shown to be important.

3.4.2. Experiments

There is considerable interest in the study of ion acoustic turbulence in connection with turbulent heating of plasmas for fusion.[55] For example, a recent pulsed experiment in toroidal geometry[59] reports measuring ω^{-1} dependence of the ion acoustic turbulent spectrum, as predicted by quasi-linear theory. However, the paper emphasizes that the experimental situation is more complex than the model of Ref. 52, and that additional effects, such as finite correlation time of the fluctuations, must be considered.

Smaller scale experiments are also very difficult to explain in terms of a particular theoretical model. In the case of a positive column experiment similar to Section 3.1., Yamada[40] concludes that the observed nonlinear spectra are better explained by theory based on electron trapping than on ion trapping. The points of comparison include the slope of the frequency dependence of the observed spectra, and the saturated level of the instability, which is shown to correspond better to that predicted by the electron trapping than the ion trapping model.

An important obstacle to understanding the turbulent state in experiments is the lack of accurate diagnostics,[55] especially for studying the k spectrum. In case of probes, measurements of short wavelengths are limited by finite dimensions of the probe and of the accompanying sheath. A promising method may be the use of laser scattering from turbulent waves, which has been used for measuring small wavelengths (2 to 0.75 mm) of cyclotron harmonic waves.[60]

Another small scale experiment[61] in a diffusion plasma reports measurements of the lifetime of density fluctuations of ion acoustic waves, which is a measure of the auto-correlation time. The evolution of the instability from the linearly unstable régime into the nonlinearly saturated (turbulent) régime is followed as the electron drift velocity is increased by increasing the potential of a grid immersed in the plasma. The lifetime is found to depend strongly on boundary conditions in the linear régime, but becomes constant and independent of electron drift velocity and boundary conditions in the turbulent state.

Finally, Ref. 62 presents evidence from laboratory and computer experiments that there exists a class of wave-particle processes which can lead to turbulent final states of ion acoustic waves, and which occur in time scales intermediate between those of hydrodynamic and trapping processes.

Thus, the theory and observations of the nonlinear turbulent state of the ion acoustic instability are still far apart. Theoretical models which can lead to saturation have not been developed to the point where it is possible to judge the relative importance of several possible mechanisms for a given experimental situation. In a similar way, experimental observations still cannot provide firm evidence for the understanding of the basic processes which lead to and govern the turbulent state. Refined experimental diagnostics have to be developed in order to yield detailed data, which are needed for a complete description of the turbulent state of the ion acoustic instability. It is intended that these shall be developed at Stanford in future studies arising from our work.

4. HOLLOW CATHODE ARC DISCHARGE: REVIEW OF LITERATURE

We turn now to a plasma source which is very different from the positive column: the gas-fed, magnetically-confined hollow cathode arc discharge (HCD). As we have seen in Sections 2 and 3, the important processes for determining the characteristics of the positive column are the interactions of charged particles with neutrals; Coulomb collisions are neglected. In contrast, in the HCD the presence of neutrals is only important in the cathode region, and elsewhere Coulomb-type interactions are of primary importance. Although electron temperatures in both sources are typically several eV, comparison of typical values of the degrees of ionization (more than 10% in the HCD compared with 1% or less in the positive column) and electron number densities (10^{13} cm^{-3} compared with 10^{10} cm^{-3}) demonstrate the basic differences which make it necessary to use radically different theoretical models in describing the HCD and the positive column.

As an introduction to Section 5, where our own work on the HCD will be reported, this section presents a review of observations made elsewhere of steady-state and time-dependent quantities in HCD discharges. Some theoretical work is also discussed, with an emphasis on applications to experimental results.

While a general review of the HCD would properly include spectroscopic light sources with low discharge currents,[9] we shall consider only intense HCD arcs of the type described by Lidsky et al.[63] These arcs were developed originally at Oak Ridge for dissociating molecular hydrogen,[8] and have come into wide use since as convenient plasma sources for ion lasers,[64,65] low-frequency wave propagation studies,[66,67] and studies of turbulent heating.[68]

Section 4.1. reports on measurements of steady-state quantities, and on the diagnostic methods used in studying the HCD; Section 4.2. considers the measurements of time-dependent quantities; and Section 4.3. closes the review with a brief summary.

4.1. Steady-State Parameters and Diagnostics

4.1.1. Steady-state parameters

The hollow cathode discharge is formed at a neutral pressure of several Torr inside a hollow cylinder made from a refractory material (W, Ta, C). The plasma then diffuses out into a highly evacuated vacuum chamber, which is made of glass or metal, and where the pressure is typically less than 10^{-3} Torr.[63] The charged particles are confined by the magnetic field and form a bright core near the axis, with a tenuous external plasma surrounding the core (see Fig. 4.1). The steady-state characteristics of the external plasma depend strongly on the boundary conditions at the wall, e.g., whether the chamber is made of glass or metal. This will be discussed in more detail in Sections 4.2.1. and 5.1.4.

The combination of a relatively high pressure arc diffusing into a region of low neutral pressure results in the formation of a highly ionized, high density (up to 10^{14} cm^{-3}) core of plasma with $T_e > T_i$. The radial profile of the bright core near axis is determined by the balance between the radial diffusion of plasma particles across the magnetic field lines and the geometric limit of the cathode diameter.

Figure 4.1 shows the experimental configuration of an early HCD apparatus.[63,69] The cathode is a tantalum cylinder about 10 cm long and several mm in diameter. Almost all reported experiments are in argon, and the background pressure in the vacuum chamber is between 10^{-4} and 10^{-3} Torr. The anode does not have any significant effect on the plasma formation; it is merely a collecting electrode for the plasma.

The HCD is started by inducing an rf discharge, which causes heating of the cathode by ion bombardment.[63] Once the cathode reaches a temperature of about 2500 K, the discharge is self-sustained, and a bright region several cathode tube diameters in length forms inside the cathode, where the discharge is generated. Measurements of the temperature of this active zone suggest that thermionic emission alone cannot yield the observed high values of emission current densities. This has led to the conclusion that secondary, photoelectric, thermionic and field emissions may all play a significant role.[64] Theoretical consideration

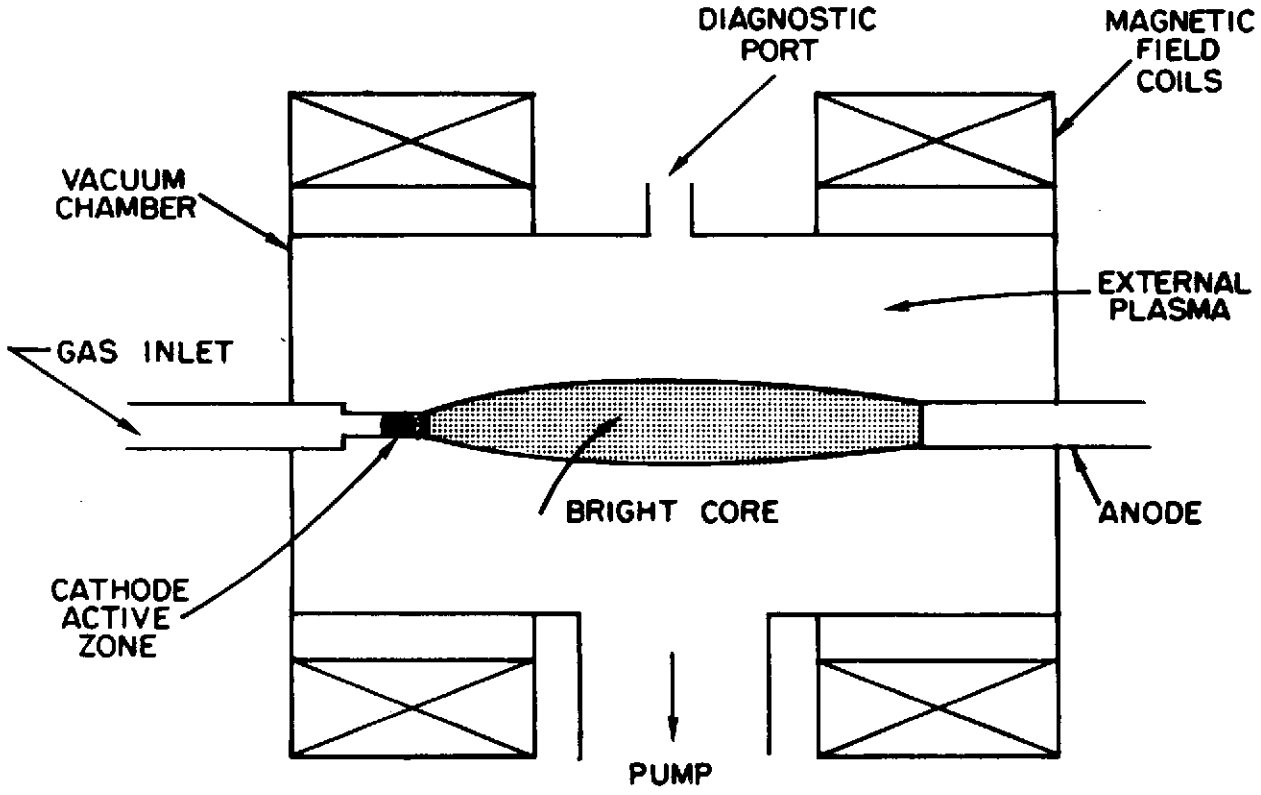

FIG. 4.1. Sketch of a typical HCD.

of heat transfer from the hot metal wall of the cathode to the gas flowing through it show that the active zone is established at an optimum value of pressure, $p \sim 4$ Torr.[70] Furthermore, a calculation of the balance between the plasma formation by collisions of electrons with metastable atoms and the loss by volume recombination, shows the existence of a local overpressure in the active zone, bounded by the formation of a sheath.[71]

In considering the origin of the bright core, there are two limiting cases. Figure 4.1 illustrates the first, in which there is significant axial potential drop in the core, so that the plasma is generated by ionization processes in the volume, driven by E_z and I. This is similar to the positive column (Section 2), where the hollow cathode acts as a cathode for the bright core. The bright light emitted by the core indicates that there are significant excitation and probably ionization processes taking place in the core.

The second case is illustrated in Fig. 4.2, in the case when the baffle and the plate anode are at the same potential. The baffle acts as an extracting electrode for the plasma diffusing out from the hollow cathode through the baffle, and following the magnetic field lines into the experimental region. There is no external power input to the column in the experimental region, so that the plasma in the experimental region is diffusion generated. In practice, a combination of the two cases exists in every experiment, depending on the exact discharge conditions.

The basic HCD configuration described above has undergone several improvements in recent years. In the case of low-pressure, high-current operation, the single large cathode tube may be replaced by an array of thin tubes. This lasts longer, operates at lower temperature, and has a lower cathode potential drop than a single tube.[72] The lifetime of the hollow cathode (10-30 h) may be further extended (up to 1000 h[64]) by using low work-function tubes made of porous tungsten impregnated with oxides of alkali metals,[65,73] or of thoriated tungsten,[64] which operate at about 1200 K. Also, the rf starting method, which is very sensitive to pressure, cathode alignment, and gas flow rate at the time that ignition is attempted,[74] may be replaced by a magnetron-type

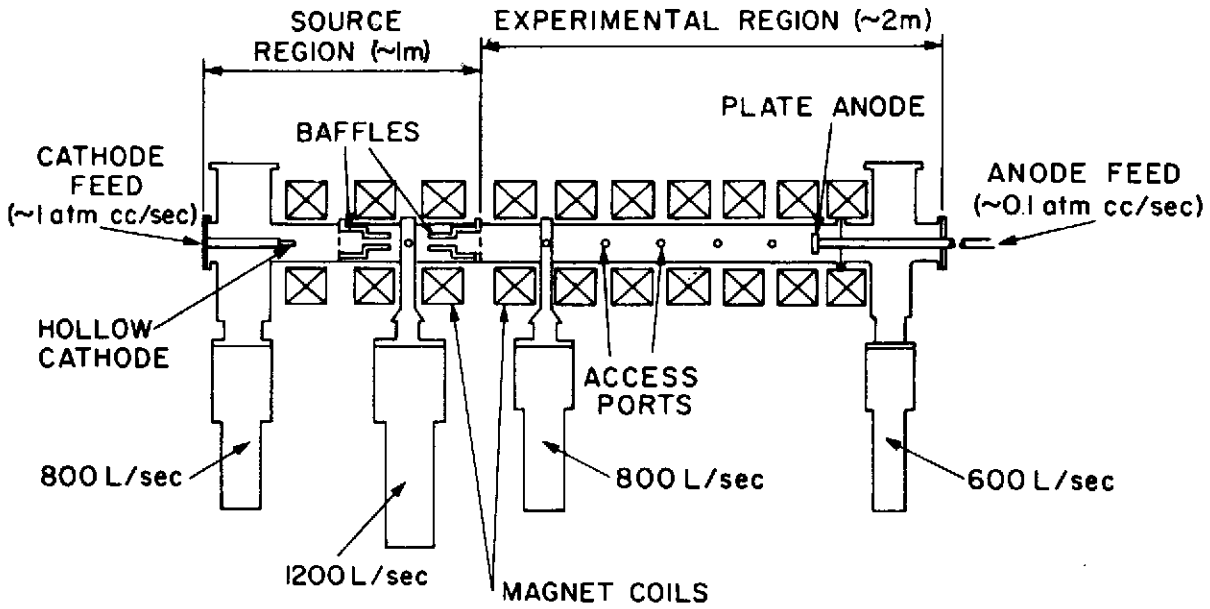

FIG. 4.2. Schematic of a HCD used for wave experiments (from References 76 and 77).

subsidiary discharge, which heats up the cathode sufficiently for the arc to start.[75]

In this review of the HCD, we are interested primarily in the characteristics of the external plasma, formed by the diffusion of plasma particles from the bright core across the magnetic field (see Fig. 4.1). The vacuum chamber of the experiments reviewed is typically long with respect to the transverse dimension. A static axial magnetic field is applied. Often, limiting electrodes are provided, with the aim of achieving a large drop of background gas pressure between the source and the experimental region (see Fig. 4.2). In this way, a high degree of ionization is obtained in the experimental region. Figure 4.2 shows such a plasma source, developed by Woo and Rose.[76,77] It is a typical example of a highly-ionized (up to 99%) discharge, suitable for studies of waves on plasmas. The additional anode gas feed, indicated in Fig. 4.2, affects the observed instability spectra in some experiments[78] (see Section 4.2.).

The HCD operates in the approximate current range from 5-300 A, with a voltage drop of about 50 - 150 V, depending on the arc length, for Ta cathode and Ar gas, and about 30% less for oxide-impreganted cathodes. Most of the measurements reported have been made at a fixed current of about 20 A.[77,79] Homogeneous and inhomogeneous (such as mirror) magnetic field configurations have been used. It is found that the presence of an axial magnetic field is not essential for arc operation in the case of a refractory cathode,[63] while a minimum value of about 300 G is required for continuous operation of a discharge with an oxide-impregnated cathode.[65]

While the flow of gas is essential to the mechanism of arc generation for the class of HCD discharges we are discussing here, Jennings et al.[65] report that an arc can be sustained even when the gas flow is reduced to zero. In that case, however, it is very likely that the discharge becomes a cold cathode arc, rather than a true HCD.

4.1.2. Measurements of plasma density and electron temperature by probes

The Langmuir probe has been the most popular diagnostic tool for investigating the properties of the HCD plasma. In the absence of magnetic field effects, the ion saturation current, I_s, drawn by a spherical probe of area S and radius much larger than the Debye length is[48]

$$I_s = \frac{neS}{2}\left(\frac{T_e}{m_i}\right)^{1/2} . \qquad (4.1)$$

Once the electron temperature is determined from the slope of the semi-logarithmic plot of the electron collecting part of the probe current (Fig. 4.3), Eq. (4.1) yields the ion density.[48] In the presence of a static magnetic field the probe characteristic changes (Fig. 4.3), because the charged particles gyrate about the field lines. At moderate magnetic fields, when the ion Larmor radius is larger than the probe dimension, the ion saturation current is still predicted accurately by Eq. (4.1). Furthermore, comparisons with measurements by several other methods indicate that accurate electron temperature data may still be obtained from the logarithmic slope of the transition from the ion saturation to the electron collecting part of the characteristic, at magnetic fields when Eq. (4.1) holds.[80]

In practice, a spherical probe of 1 mm diameter usually satisfies the conditions of being smaller than the ion Larmor radius and larger than the Debye length, and the resulting plots are easily interpreted on the basis of the above simple theory.

There are certain difficulties associated with probe measurements in the bright core. The heat of the discharge melts the insulation of the probes, so that they have to be constructed with refractory insulators, such as alumina or boron nitride, for measurements near the core.[81] Also, a hot probe emits electrons which affect the probe characteristic.[82] Consequently, the reported measurements mostly deal with the external plasma.

The results of measurements of the radial profiles of electron temperature and plasma density in a source such as the one sketched

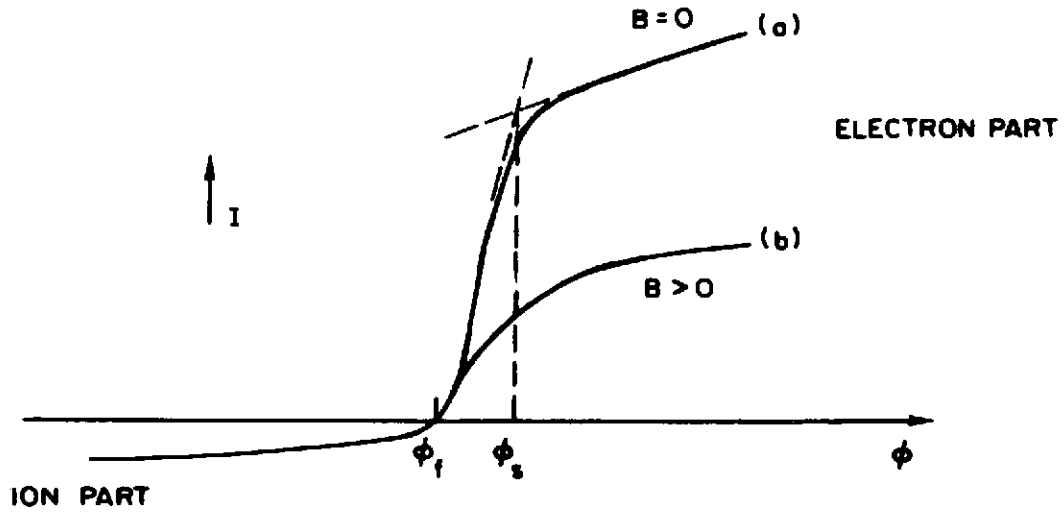

FIG. 4.3. Typical Langmuir probe current-voltage characteristic drawn to a linear scale (a) without, and (b) with magnetic field present.

in Fig. 4.2 show that there is a high-density (10^{12} - 10^{14} cm^{-3}) plasma with electron temperature of several eV on axis, surrounded by a layer of lower density (external) plasma. The density falls off radially much more rapidly than the electron temperature. The exact values on axis depend on the pressure, current and magnetic field.[77]

4.1.3. Other measurements by probes

The plasma space potential in the absence of magnetic field is relatively easily determined as the potential of the probe characteristic at which electron saturation current is drawn (ϕ_s in Fig. 4.3).[48] However, this part of the probe characteristic is strongly affected by the presence of even very weak magnetic fields, so that some other method must be used.

The floating potential, ϕ_f, which is easily determined as that potential at which the probe draws no current, may be related to the space potential by[48]

$$\phi_s = \phi_f + cT_e/e \ , \qquad (4.2)$$

where c is a coefficient which depends on the effective probe area for electron collection. The second term in Eq. (4.2) introduces a correction due to the presence of the sheath, and varies radially because T_e is a function of position. In the presence of magnetic field, there is no theoretical analysis available for calculating c. A value of $c = 4$ is often assigned,[48,81] with the justification that it is an average of various values calculated[81] for argon without magnetic field. By differentiating the space potential profile, given by Eq. (4.2), the radial electric field profile is obtained, with accuracy which Hudis and Lidsky[81] estimate to be only within a factor of three. Thus, the radial electric field measurements leave much to be desired.

Measurements on typical HCD external plasmas have indicated that ϕ_f has a pronounced minimum on axis and increases radially, while T_e decreases monotonically with radius. When Eq. (4.2) is applied, a negative radial electric field is obtained near the axis, which is inverted compared to the unmagnetized positive column, Fig. 2.6(b).

Thus, the plasma on axis is confined by magnetic field effects on the electrons, and by negative space-charge field effects on the ions. The potential profile at large radii is governed by the conditions at the wall, as will be shown and discussed in Section 5.1.3.

Attempts to measure space potential with emitting probes have been reported,[67] but they are subject to serious limitations in the presence of magnetic field, since the part of the probe characteristic near electron saturation is used for determining ϕ_s.[82,83] Morse[69] has reported measuring positive radial electric field by this method in a rather short arc. It is not clear whether the high end losses to be expected in this case strongly modified the potential distribution, or whether it was the dubious measuring method which was responsible for the difference in sign of the electric field with respect to the results of other work.[73,77,79]

Directional Langmuir probe measurements have also been reported. Such probes effectively measure the variation of ion current drawn as the probe orientation is varied, and the corresponding theory gives the ion drift velocity in terms of the difference of ion currents drawn in two opposite directions. The azimuthal velocity of ions rotating around the axis in the external plasma has been measured in this way.[79,81] The weak point of the method is that the interpretation of measurements is based on a theoretical model which makes numerous simplifying assumptions about the ion motion (e.g., that the ions are monoenergetic and with a uniform drift velocity) which are difficult to justify for the HCD.

4.1.4. Spectroscopic diagnostics

Since the light output of the external plasma is very low, only the results of spectroscopic measurements of charged particle temperatures at or near the bright core have been reported. By measuring the Doppler broadening of certain ion lines, the ion temperature can be deduced. Conventional line broadening measurements with prism or grating spectrometers are limited by instrumental broadening. If taken literally, they provide excessive values ($T_i \sim 30$ eV in Ref.78).

The application of Fabry-Perot interferometer techniques, together with careful consideration of Zeeman splitting in the presence of the

external magnetic field, provide the best data currently available. The values of ion temperature thus obtained increase with magnetic field and discharge current, and range from 0.4 eV[84] to 2.5 eV.[85] No detailed radial ion temperature profiles have been reported in the literature, perhaps partly because of the difficulties of isoloating light from a small region, and separating the broadenings due to different ion drifts along the line of sight.

Electron temperature may be determined by measuring relative intensities of two spectral lines.[85-87] The results of the values on axis are reported, and agree with probe data extrapolated into the core.

Spectroscopic methods have also been used to measure the velocity of rotation of ions and neutrals, by measuring the Doppler shift of a corresponding spectral line.[85,88] Radial variation of the ion azimuthal velocity ($\sim 10^5$ cm/sec) up to about 3 cm from the axis is determined in Refs. 85 and 88. Reference 85 also determines the azimuthal velocity of neutrals, which are dragged by the rotating ions, to be about one-fifth of the ion velocity, up to about 2 cm from the axis.

4.1.5. Other diagnostic methods

Microwave methods have been used by several workers to check the values of electron density in the core.[77,84,85,88] Reported results refer to a single measurement of phase shift or of transmitted power of a microwave beam passing through the plasma, as a check of the measured mean or cut-off electron density against probe data.

Incoherent Thompson scattering of ruby laser light has also been used for measuring electron density and temperature.[89,90] A salient advantage of the method is that the electron temperatures parallel and perpendicular to the magnetic field can be measured separately. While some early measurements yielded results which are up to 50% lower than probe data,[89] a recent paper reports improved agreement of some preliminary results for T_e and n_e.[90] The data refer to the plasma in the bright core, and further refinement of the experiment is expected to extend the application of the method to the external plasma.[90]

A metal pendulum suspended in the external plasma and deflected by the rotating plasma particles is the basis of another technique for measuring the azimuthal velocity of ions.[79,88] The deflection of the pendulum is interpreted to be due entirely to the ions. The values of the ion azimuthal velocity thus obtained are about 30% higher than the spectroscopically measured ion rotation velocity in the transition region between the core and the external plasma.[88] The method is subject to doubt because the presence of a metal surface inside the plasma may cause significant perturbation in the discharge conditions. Additionally, the pendulum is deflected by the combined impulses from all plasma particles, while the interpretation considers only the ions.

The data on the ion azimuthal velocity taken by the three different methods (directional probe, Doppler shift of ion lines and pendulum) indicate an order of magnitude agreement ($\sim 10^5$ m/sec). This is good agreement in view of the fact that the data were taken on three different experiments. It indicates that the ion azimuthal drift is the important effect in plasma rotation, as assumed in the theoretical interpretations of measurements by the three methods.

4.1.6. Discussion of steady-state parameters of the HCD

The conditions under which the arc is formed inside the hollow cathode have been studied thoroughly for the combination of a tantalum cathode and argon.[70,71] A similar analysis remains to be done for an oxide-impregnated cathode, which will clarify the observed differences between the two types (Section 4.1.1.).

The radial profiles of plasma density and electron temperature in the HCD are well-documented. Reliable data on the radial profile of the ion temperature and accurate space potential data in the external plasma are lacking. It would be desirable to develop a theoretical model of the HCD which would provide a complete description of the spatial variations of all physical quantities, as is possible for the positive column (Chapter 2). However, as noted in the Appendix, the presence of the strong magnetic field emphasizes the effects of end losses; the axial motions of charged particles are nearly collisionless, while their radial motions are effectively collision-dominated, due to

the confining effect of the magnetic field. Thus, even though the discharge may be physically very long with respect to the radial dimensions, it must be treated as a finite cylinder. This is shown for the positive column in the Appendix.[6] The implications of the strong magnetic field for the HCD depend on whether the walls are insulating or metal. In the first case, the radial diffusion of charged particles is ambipolar, since electron and ion fluxes must be equal at the wall. In the second case, Simon diffusion[91] is important: the electrons flow freely to the axial boundary along the magnetic field lines, while the ions flow radially across the magnetic field to the conducting wall, and then to the axial boundary to recombine with electrons.

Since the exact geometric configurations of the various HCD experiments differ considerably, and the various biased baffles cause further differences in the number density distributions of both the neutral and charged particles, it is practically impossible to develop a single theoretical model which would be capable of predicting the steady state of the various experimental systems. Instead, it is necessary to develop a specialized model for each particular system, to take into account the important end effects of that experiment.

Further complicating factors encountered in describing the external plasma theoretically include the inapplicability of the isothermal approximations for electrons and ions, the importance of including Coulomb collisions and radiation processes in the model, and the presence of instabilities which may be so strong as to affect the steady state.

Since all of these effects are difficult to model, it is not likely that a realistic model of a HCD will be developed soon. Further refinement of the diagnostic methods, especially for deducing the spatial variations of ion temperature and space potential, are needed before a thorough understanding of the HCD can be reached.

4.2. Measurements of Low-Frequency Instabilities

It is seen from the measurements of Section 4.1. that the HCD is a highly ionized plasma with magnetic field and current in the axial direction, and electric field and charged particle density and temperature inhomogeneities in the radial direction. Consequently, there are several kinds of charged particle drifts present which may lead to the excitation of instabilities.

First, there is drift in the axial direction due to the axial current. Then, the combined effects of E_r and B_z cause electrons and ions to drift azimuthally with velocity E_r/B_z (Hall drift). In the presence of collisions with neutrals, charge separation results between electrons and ions from their different collision rates with neutrals, and the charged particles drift azimuthally at different velocities (neutral drag effect). Finally, an equivalent drift of electrons relative to ions appears in fluid equations due to the electron density (or pressure) gradient normal to B_z (diamagnetic drift).[34]

Each one of these drifts represents a source of free energy in plasma which can lead to the excitation of instabilities. These instabilities are classified and named according to which effect plays the dominant role in exciting them. A discussion of the various kinds of instabilities which have been observed in general is outside the scope of this work. Such a thorough treatment, including a variety of microscopic and macroscopic destabilizing effects additional to the drifts described above, is to be found in the review by Lehnert.[7]

We concentrate here on the instabilities observed in the HCD, for which it is sufficient to consider the macroscopic destabilizing drifts listed above. Fluid treatments of low-frequency instabilities in magnetoplasmas have recently been given by Self[34] for the weakly ionized case, and by Rognlien[10] for fully ionized plasma, and they include discussions of most of the instability types relevant to the HCD.

The HCD is especially rich in self-excited oscillations in the frequency range up to 100 kHz (the ion cyclotron frequency is 50 kHz for argon at about 1.3 kG), with practically no self-excited noise above 1 MHz. Langmuir probes at floating potential are often used to

detect potential fluctuations, while probes biased into ion saturation (usually 50 V negative with respect to the floating potential) yield density fluctuation data. Probes are easy to use, they offer spatial resolution, and they do not perturb the plasma appreciably, since the sheaths covering them are very thin under typical experimental conditions. Furthermore, there is a great variety of instruments for measuring amplitude and phase of signals at these low frequencies, so that the spatial characteristics of the instabilities may be investigated easily (see Section 5.1).

4.2.1. Measurements of self-excited waves

A summary of the results of observations of low-frequency self-excited waves in HCD experiments is presented in Table 4.1. Measurements are performed at about 20 A discharge current, except Ref. 78, which reports data measured at 150 A.

Morse observed rotating flutes (no axial dependence) in a short HCD (see Fig. 4.1) by time-resolved measurements of density fluctuations using a Langmuir probe.[69] He detected an $m = -1$ mode at about 2 kHz, where m is the azimuthal mode number such that negative m denotes the left-hand direction with respect to the magnetic field (see Fig. 4.4). His theory invoked the neutral drag driving mechanism for the flutes,[92] and the calculated eigenfunctions in slab geometry agreed with the observed frequency, but not with the observed shape of the flutes. The theory uses electric field values as determined from the electron saturation of Langmuir probe characteristic, which is a dubious method in the presence of magnetic field (see Section 4.1.3.).

Chung and Rose[77] report observing two instabilities, at 8 and 50 kHz. The higher frequency mode[93] is localized in the bright core and propagates radially. Its frequency varies linearly with magnetic field, and does not vary with the discharge length. It is identified as the electrostatic ion cyclotron instability, on the basis of a model of an axial current-driven cyclotron wave in a homogeneous, collisionless plasma. The wave is predicted to have the highest growth rate at a frequency of $1.2\ \omega_{ci}$, where ω_{ci} is the ion cyclotron frequency, which agrees with the experiment.

TABLE 4.1

Summary of low-frequency instabilities observed in HCD

(L = arc length; k_z = axial wavenumber)

Reference	Frequency [kHz]	m	k_z	Radial location:	Type of instability
Morse (69)	2	-1	≈ 0	near axis	neutral drag
Chung and Rose (77,93,94)	50	propagates radially		core;	ion cyclotron;
	8	1	?	external plasma, at large ∇n	drift
Kretschmer et al. (78)	14	0	$\pi/2L$	external plasma	slow Alfvén;
	12	1	0		drift;
	80	1			
	45	1,2	0		modified torsional Alfvén
Gunshor et al. (73)	8	1	?	external plasma;	drift;
	5	1	π/L	external plasma	ion acoustic
Aldridge and Keen (79)	15	1	0	external plasma	rotationally-convected drift
Wheeler (95)	2	-1	0	near wall;	centrifugal flute;
	30	1	0	near axis	centrifugal flute

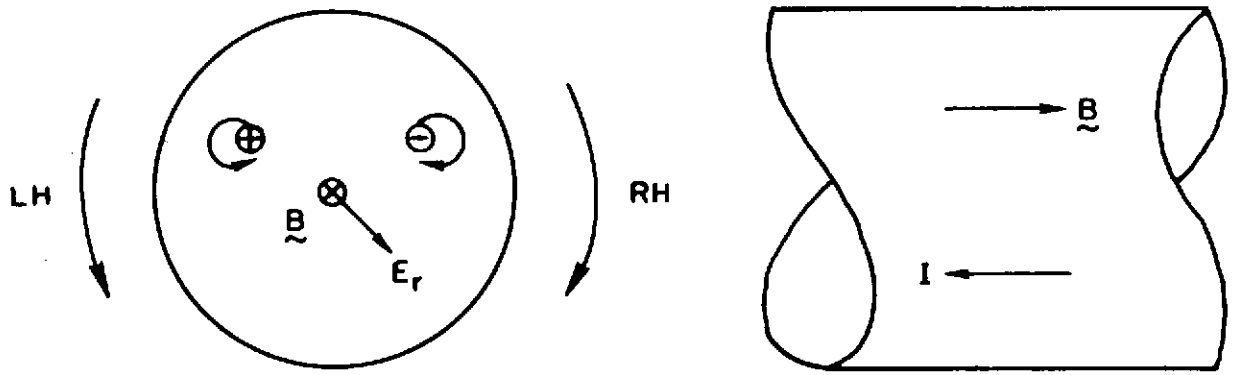

FIG. 4.4. The azimuthal directions with respect to the magnetic field: left-hand (LH) and right-hand (RH).

The lower frequency mode[94] propagates azimuthally with $m = 1$ and occurs in the external plasma, in the region of large density gradient. The mode is identified as a drift wave, described by a slab model with density gradient normal to the magnetic field, B_z. The use of a local approximation in the theory ($k_\perp \gg (1/n)(dn/dx)$, where $k_\perp$ is the wavenumber for propagation perpendicular to B), which implies that the wave is localized in a space much smaller than the scale length for density fall-off, is not experimentally justified. As discussed by Self,[34] a drift wave requires finite k_z in order to provide the necessary phase shift between potential and density fluctuations via the electron longitudinal motion. However, no data on k_z are reported, and no attempt to explain the radial profiles of fluctuations is presented. The identification is based only on the agreement of calculated and observed frequencies, which leaves it open to doubt.

Kretschmer et al.[78] report observing a variety of modes in a high-current experiment (see Table 4.1). They present measurements of the frequency dependences of the various modes on the static magnetic field, and base the identification of the modes listed in Table 4.1 on a qualitative agreement of the frequencies observed with predictions of several models which may be applicable to their discharge. However, there is little experimental justification presented for using these models; their identifications must be viewed only as plausibility arguments about the existence of the various waves in their discharge, rather than convincing identifications.

Gunshor et al.[73] observe the drift wave described by Chung and Rose,[77] and also an additional mode at about 5 kHz. The measured frequency of the latter depends inversely on the length of the discharge, when it is varied by about 30%, and the frequency for four noble gases is inversely proportional to $m_i^{1/2}$. The mode varies azimuthally as $m = 1$. It is identified as a standing ion acoustic wave in the z-direction on the basis of the agreement of the observed frequency with that of a model of an ion acoustic wave propagating at an angle to the magnetic field in a collisionless plasma slab. The identification again must be viewed as doubtful, because there is no instability analysis presented for the

wave and no attempt to measure or relate to theory the radial profile of the instability.

Aldridge and Keen[79] report the measurements of the radial profiles of potential fluctuations of an $m = 1$, $k_z = 0$ instability. They find agreement between the measured frequency in a wide range of magnetic fields and that predicted from a model for an instability in a weakly ionized plasma slab (in the local approximation). The wave is identified as a rotationally convected drift wave on the basis of the frequency agreement. The identification is open to doubt because a drift wave must have $k_z \neq 0$; their theory for $k_z = 0$ actually represents a form of the neutral drag instability.[10,11] Furthermore, their measurements clearly indicate that the local approximation is inapplicable. The authors state that the full calculation in cylindrical geometry is required for a more complete theoretical model.

Wheeler observes two azimuthally propagating flutes:[95] at large radii, a 2 kHz, $m = -1$ instability exists in the region of positive radial electric field, while a 30 kHz, $m = 1$ mode is localized close to the axis, where the radial electric field is negative. The electric field data are deduced from Langmuir probe theory, neglecting magnetic field effects, so that they are open to doubt, as discussed in Section 4.1.2. The two modes are identified as centrifugal flute modes by comparison with a slab model, including an equivalent gravity to account for centrifugal effects. The theory predicts the observed frequencies and directions of propagation, the observed growth rates, and assumes $k_z = 0$, as observed experimentally. It also predicts that the energy density of centrifugal motion is peaked near the axis and also near the wall, which agrees qualitatively with the observed radial locations of the modes.

In concluding this section, we note that all of the above papers report observing an azimuthally-propagating instability, and identify it on the basis of the agreement of the observed frequency and direction of propagation with a plasma slab model. The experiments are performed in systems with glass (Refs. 79 and 73) or metal walls (Refs. 69, 77, 78 and 95), and the boundary conditions significantly affect the radial

electric field profile (see also Section 5.1.). This is demonstrated by the fact that the ions rotate around the axis in the left-hand direction when the vacuum chamber is metal,[88] and in the right-hand direction when glass vacuum chamber is used.[79,85] Thus, the various experiments differ significantly from one another in the spatial distributions of space potential and in the charged and neutral particle density variations, as discussed in Section 4.2.1. Consequently, it is difficult to judge whether or not the instabilities with similar characteristics observed in different experiments are geometrically modified versions of the same modes.

In order to decide whether the observed instabilities are in fact one mode, altered by the particular geometry and discharge conditions, it is necessary to provide a more complete identification than was presented by the papers reviewed. The full problem in cylindrical geometry should be solved, instead of using the localized slab model. Measured steady-state characteristics of the discharge should be used in calculating the eigenfunctions for the model, and a proper stability analysis included. In this way, the measured profiles of amplitude and phase of the instability can be checked against the computed eigenfunctions. This approach is used in the identification of two modes observed in our HCD, to be presented in Section 5.

4.2.2. Radial diffusion of plasma

Classical diffusion occurs when plasma particles diffuse across the magnetic field lines due to scattering by collisions. In the presence of low-frequency instabilities ($\omega \ll \omega_{ci}$), the diffusion is enhanced above the classical value because of E_{1r}/B_z particle drifts, where E_{1r} is the radial component of the fluctuating electric field of the instability. The phenomenon is referred to as anomalous or wave-enhanced diffusion, though it is not strictly a diffusion process. Several authors have reported that the radial flux of plasma particles increases when instabilities are excited.[77,93,95,96]

Chung et al.[77,93] report an increase in the axial plasma density and a decrease in the scale length of the radial density profile when their ion cyclotron instability is quenched. Noon et al.[96] show that their radial scale length varies as B^{-1} when their "ion acoustic" mode is suppressed, and increases to $B^{-1/2}$ variation in the presence of the wave; power input to the arc at constant current also increases when the instability is excited. Finally, Wheeler also observes enhanced radial transport of ions in the presence of the 2 kHz flute mode, which is excited at large radii in his experiment[95] (see Table 4.1).

Flannery and Brown modulate the current of their discharge at 400 Hz and at a low value of magnetic field, when no significant instabilities are present.[66] They follow the radial propagation of the resulting diffusion wave by measuring the radial variations of phase and amplitude of the density fluctuations. By comparing the results with a theory for radial ion diffusion, including a provision for axial end loss of particles, they conclude that the diffusion proceeds at a classical rate, without evidence of anomalous diffusion.

Thus, the radial transport of plasma particles is governed by collisional effects in the quiescent régime; the presence of low-frequency instabilities causes an increase in their radial diffusion rates.

4.2.3. Suppression and enhancement of low-frequency waves

It has been noted above that particular modes may be strongly excited or damped by suitable choice of discharge conditions. Woo and Rose determine that the self-excited instabilities are generated in the high-pressure cathode region, where large gradients of potential and neutral density and pressure exist.[76] They separate the highly collisional cathode region from the low pressure collisionless experimental region by a baffle of such dimensions that a slightly collisional discharge exists there (see Fig. 4.2). This effectively damps out the self-excited instabilities.

A corresponding theory for a partially ionized, collisional plasma slab shows that the difference between the electron and ion axial drifts provides a destabilizing effect, and the baffle dimensions have to be

chosen in such a way that $\omega_{ci} \simeq \nu_i$, where ν_i is the ion-neutral collision frequency, for the baffles to be effective for noise suppression.[97]

Feedback circuits have also been utilized for influencing the excitation of a particular mode.[95,98,99] By varying the gain and phase of the feedback signal, it is shown that a drift instability at 5 kHz may be completely suppressed or enhanced,[98] and a corresponding nonlinear theory explains the measured results.[99] In a similar way, Wheeler reports stabilization of the low frequency flute instability responsible for enhanced radial diffusion.[95]

4.2.4. Experiments with externally-excited waves

In addition to the diffusion wave experiment of Flannery and Brown[66] described above, Keen and Aldridge also excite externally a low-frequency drift wave by a system of electrodes in a discharge in helium, which has a constant radial density scale length, $(1/n)(dn/dr)$.[67] The electrodes enable selective excitation of $m = 0, \pm 1$ modes, and the wave dispersion is measured in the range from 20 to 220 kHz. Reasonable agreement is found with a localized drift wave dispersion relation based on a slab model, which includes the effects of radial electric field and ion-neutral collisions.

4.3. Summary

The external discharge of the HCD represents a source of high density, inhomogeneous and highly ionized plasma which is often subject to a variety of low-frequency, self-excited instabilities. These instabilities may be suppressed by varying the discharge parameters, or by using external stabilization methods, so that a quiescent source for studying waves on highly ionized plasmas at low B_z may be obtained.

A complete identification of these instabilities, including prediction of spatial variations of amplitude and phase of potential and density fluctuations, is hampered by lack of data on the spatial variations of steady-state electric field and ion temperature (see Section 4.1.6.), which have important roles in exciting the instabilities. However, even with the data which are now available, it is possible to

provide much more complete identifications of the observed modes than are presented in the reviewed papers.

Section 5 presents such a complete identification of two centrifugal flute modes in our HCD experiment, using the approach outlined at the end of Section 4.2.1.

5. FLUTE INSTABILITIES OF A HOLLOW CATHODE ARC DISCHARGE

This section presents the experimental results obtained on our HCD. Steady-state characteristics are determined, and two observed instabilities are identified as centrifugal flute modes, driven by $\underset{\sim}{E} \times \underset{\sim}{B}/B^2$ drift in the presence of a radial electron density gradient. The identification is based on comparison with eigenfunctions calculated from a linear theory for a collisionless, cylindrical plasma column, which was developed by Rognlien.[10]

Details of the experimental set-up, and the results of measurements of steady-state and time-dependent quantities are given in Section 5.1. Section 5.2. outlines the theory, which is compared with experimental results in Section 5.3. The section closes with a brief discussion in Section 5.4.

5.1. HCD Experiment

In the description of the experiment, special attention is paid to experimental results which lead us to the theoretical model of Section 5.2. In particular, the effects of the radial electric field on excitation of the two instabilities are noted, and parameter ranges are indicated where they are suppressed.

5.1.1. Apparatus and diagnostics

The HCD is enclosed in a cylindrical vacuum chamber with Pyrex glass walls of 10 cm inside diameter. Figure 5.1(a) shows schematically two metal wall sections, one a pumping port and the other a diagnostic port. The arc is confined by an axial magnetic field, homogeneous to ±2% over a length of 1 m, produced by ten coils. The system is pumped by three 700 ℓ/s diffusion pumps, and the pressure is measured by an ionization gauge located at the diagnostic port.

The hollow cathode is a tungsten tube impregnated with barium oxide (3.1 mm O.D., 0.4 mm wall thickness, and 7.6 cm long) through which argon flows. The HCD operates at axial plasma densities of 10^{12} - 10^{13} cm^{-3} and a background pressure of $\sim 2 \times 10^{-4}$ Torr in argon, so that the degree of ionization near the axis ranges from 10 to 50%.

The cathode, and the pumping and diagnostic ports, are grounded, while the anode runs at a positive potential. The main discharge starts

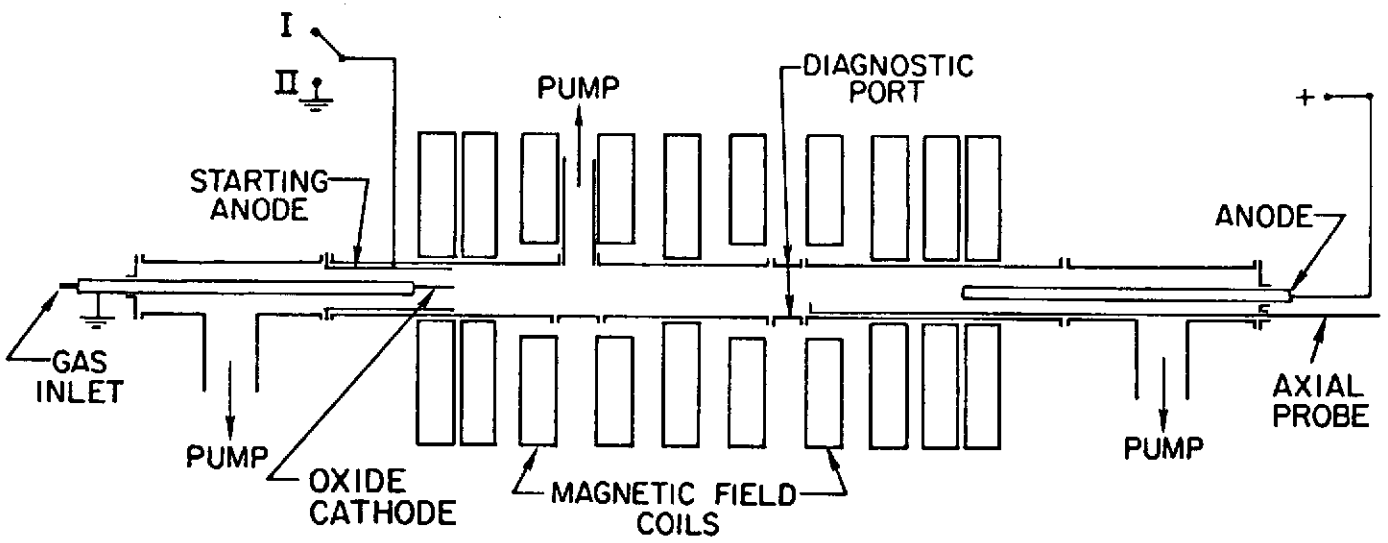

FIG. 5.1. (a) Sketch of the HCD.

easily once the cathode has been heated by a subsidiary magnetron-type discharge initiated between the starting anode and the cathode.[68,75] As shown in Fig. 5.1(a), the copper cylinder which constitutes the starting anode is very close to the glass wall. When left to float, it comes to the wall potential, which is normally close to the anode potential (see Fig. 5.5). When grounded, it draws about 0.8 A and causes the potential at the wall to decrease significantly. These observations show that the starting anode is in good electrical contact with the discharge. Since, at this radius, electrons move without collisions along the field lines, it effectively controls the potential at the wall along the entire length of the discharge. The discharge appears as an intense blue central core ($\sim$ 1 to 2 cm diameter, depending on discharge conditions) surrounded by a less intense external plasma extending to the tube walls, and has the typical gas-filled electron tube characteristic of constant voltage for a wide range of currents.

Typical running parameters of our arc are: current from 4 - 40 A; magnetic field from 0 - 3 kG; pressure from 10^{-4} - 10^{-3} Torr, and voltage from 30 - 50 V, depending mainly on the pressure. Current and magnetic field upper bounds are dictated by the power supplies available to us, while the ranges of pressure and voltage are characteristic of the arc.

The measurements reported here were performed in argon. Attempts to run a discharge in helium with the oxide cathode produced a discharge which was difficult to start and was easily extinguished. Other authors have reported similar difficulties for gases other than argon.[89]

There are four identical radially movable probes at the diagnostic port, located in the same axial plane, and at azimuthal positions indicated on Fig. 5.1(b). Two types of probes were constructed, as shown in Fig. 5.1(c). Shielded coaxial probes were used for ac diagnostic studies. Langmuir probes which were used for dc diagnostics were insulated with a layer of cataphoretically deposited alumina fired in an atmosphere of hydrogen.[46] This particular construction proved to be very resistant to the high temperature near the axis of the discharge, which tends to destroy less thermally resistant insulating materials. Since the probe diameter is much larger than the Debye length, and much smaller than the ion Larmor radius, the effect of the magnetic field

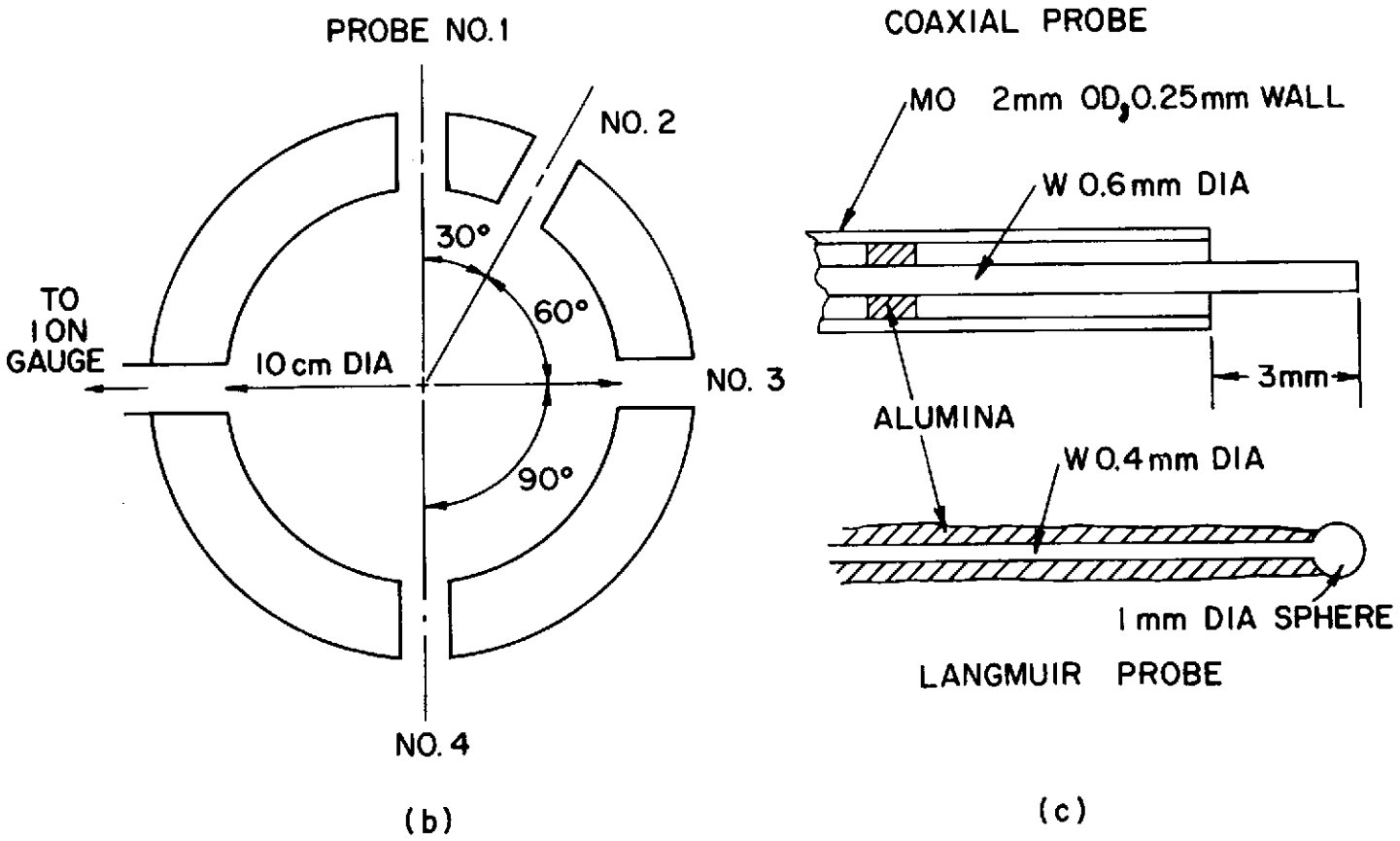

FIG. 5.1. (b) Cross-sectional view of the diagnostic port.
(c) Details of coaxial and Langmuir probe constructions.

on the ions can be neglected. Simple probe theory for the ion saturation part of the probe characteristic can then be applied, and electron temperature can be deduced by plotting the electron current, corrected for the effect of ion current(see Section 4.1.2.).

Axial variations of the discharge parameters were measured using a long coaxial probe lying along the bottom of the glass chamber and motor driven from the anode flange. Like radial Probe No. 3, the axial probe is provided with an electrical position indicator. It could also be rotated about its axis to check radial variations at various axial positions. The time-dependent quantities were investigated with the shielded probes, as well as with the Langmuir probes. Both types yielded similar results for low-frequency instabilities.

5.1.2. Measurements of instabilities and radial profiles

Under certain conditions of pressure, the voltage-current characteristic exhibits step jumps in voltage which correspond to excitation of low-frequency instabilities. The spectra of instabilities are observed as potential fluctuations on a floating probe, or as density fluctuations on a probe biased into ion saturation. They are found to exhibit complicated dependences on the external parameters of pressure p, current I, magnetic field B, and starting anode potential V_a.

Since the arc is highly ionized, the pressure varies significantly when current is varied at a constant gas flow rate. The instabilities investigated here are excited when the pressure falls below about 2×10^{-4} Torr, while increase of pressure above that value is generally stabilizing. Increase of discharge current, the pressure being kept constant by increasing the gas flow, is also stabilizing. Observations made at magnetic fields above about 1 kG indicate that increasing the magnetic field causes the general noise level to increase, and with it the arc voltage at constant current.

For $I \sim 10$ A, $B \sim 1.3$ kG, when the pressure is reduced below $\sim 1.4 \times 10^{-4}$ Torr, certain strong coherent modes are excited. These include a strong oscillation in the neighborhood of 10 kHz, plus its harmonics, and another at about 70 kHz. The former has significant amplitude outside the core, is sensitive to the starting anode potential,

and is the subject of detailed study in what follows. The latter, which is confined to the core region, tunes with B, and is probably the ion cyclotron mode observed by Chung and Rose.[77]

In view of the complex dependence on the four external parameters, attention was focussed on the lower frequency instabilities occurring in the neighborhood of the following standard conditions: $p \sim 1 - 4 \times 10^{-4}$ Torr, $I = 10$ A, $B = 1.3$ kG, and with the starting anode either floating or grounded. Under these conditions the instabilities have sufficient amplitude and coherence for good measurements.

The radial and axial dependences of the amplitude and phase of the fluctuating potential, ϕ_1, and density, n_1, were measured with probes using the circuits of Fig. 5.2. For ϕ_1 the floating probe potential is taken, while n_1 is measured by the fluctuating current when the probe is biased into ion saturation. The phase measurements from the phasemeter were consistent with the cross-correlation data from the correlator.

A strong instability at about 9 kHz is easily excited by lowering the pressure below 1.4×10^{-4} Torr with the starting anode floating. When the starting anode is grounded, a somewhat weaker instability at about 7 kHz develops. We label these Mode I and Mode II, respectively. As shown in Figs. 5.3 and 5.4, both modes are strongly excited outside the high density core, with significant radial variation of the amplitude and phase of potential and density fluctuations. Such measurements, made with radial probes at various azimuthal and identical radial positions, indicate that Mode I has an $m = 1$, while Mode II has an $m = -1$ azimuthal variation. Positive m-numbers indicate azimuthal propagation in the right-hand direction with respect to the magnetic field (the direction of electron gyration), and negative m-numbers indicate the left-hand direction. Measurements of the axial dependence of $|\phi_1|$ for both modes, do not indicate the presence of a standing wave of finite wavelength. Both instabilities have nearly constant phase axially (less than $\pm 5^\circ$ change over a length of 70 cm), which justifies the assumption $k_\parallel = 0$ of our theory.

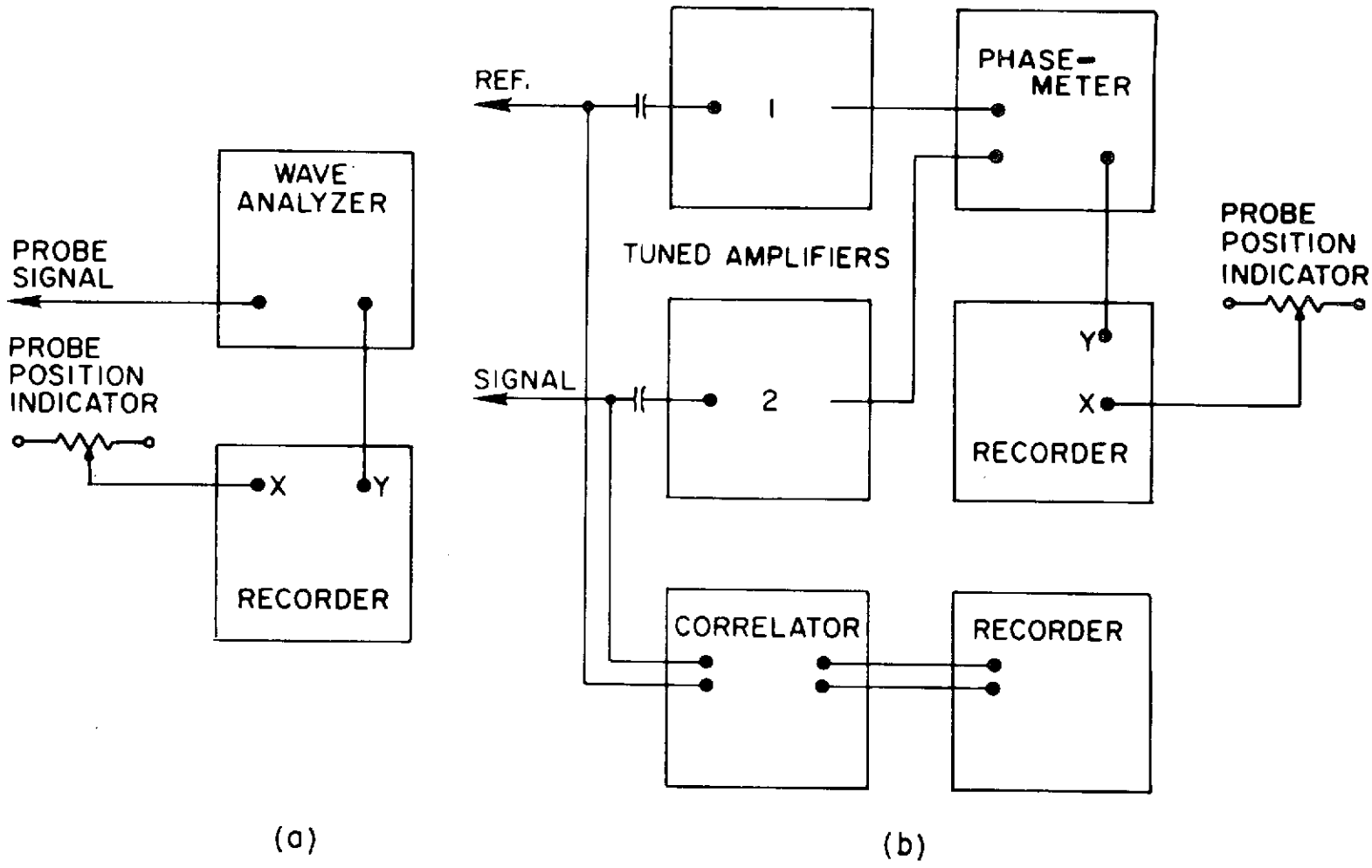

FIG. 5.2. Schematic of (a) amplitude and (b) phase measuring circuits.

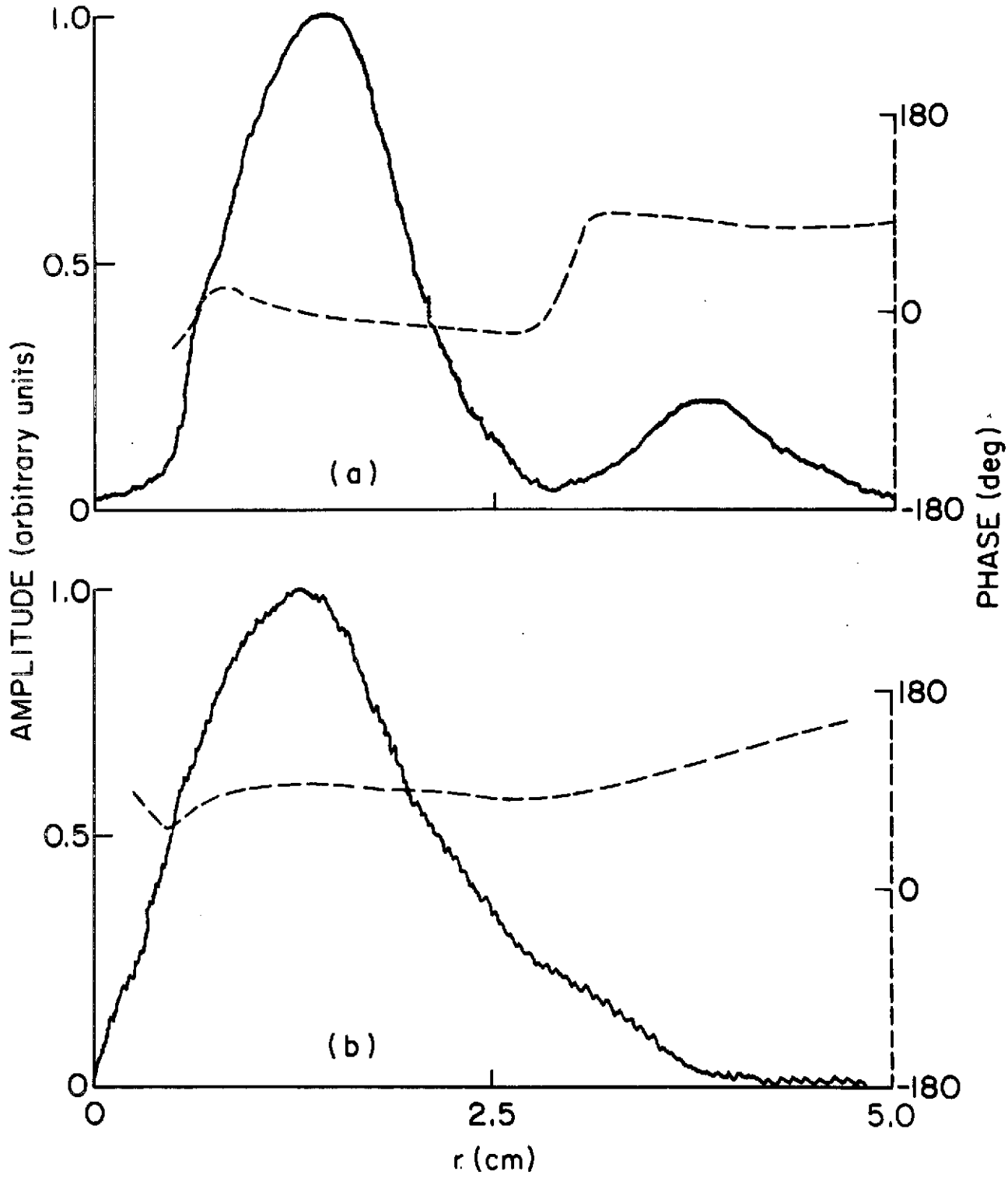

FIG. 5.3. The experimental radial variations of amplitude and phase of (a) potential, and (b) density fluctuations of Mode I. Discharge parameters are: $p = 8 \times 10^{-5}$ Torr, I = 10 A, B = 1.3 kG.

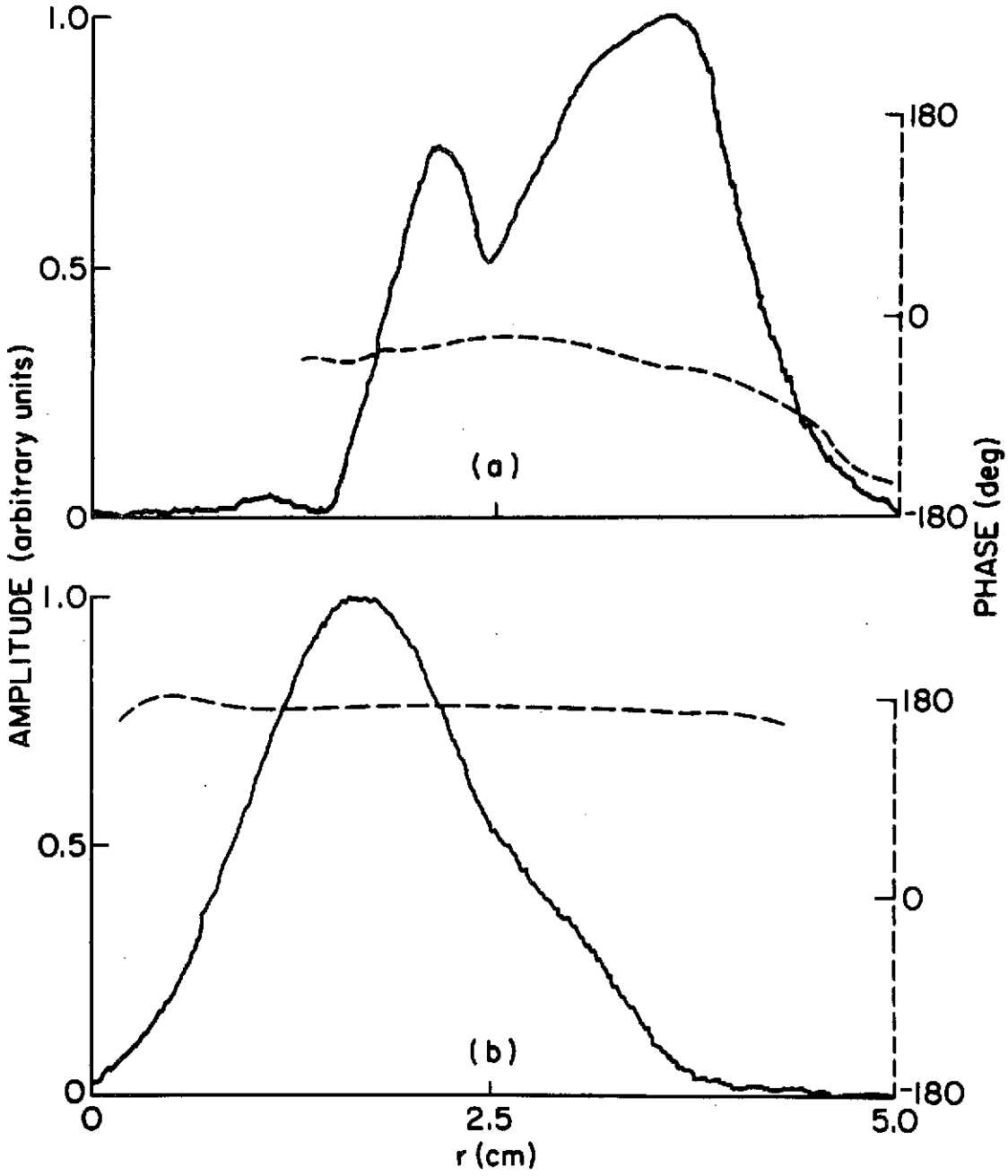

FIG. 5.4. The experimental radial variations of amplitude and phase of (a) potential, and (b) density fluctuations of Mode II. Discharge parameters are: $p = 1.0 \times 10^{-4}$ Torr, I = 10 A, B = 1.3 kG.

The presence of Modes I and II influences the steady-state profiles of potential ϕ, density n, and electron temperature T_e. Figure 5.5 shows the profiles of floating probe potential for quiescent conditions at $p = 3 \times 10^{-4}$ Torr, and with instabilities present at $p = 1 \times 10^{-4}$ Torr, both for floating and grounded starting anode. The potential is inverted compared to that of the more familiar positive column[5] [see Fig. 2.6(b)]. This indicated that the electrons are confined better than the ions, which must have appreciable temperature. Thus, the ambipolar electric field acts to increase the electron radial current and reduce that of the ions to equalize them. The sharp rise in potential at small radii is associated with the rapid drop in n and T_e at the edge of the core (see Figs. 5.6 and 5.7). The depression of the potential due to grounding the starting anode is clearly evident. The increase of arc voltage, V_A, from 34 V to 45 V as the pressure is decreased is attributable largely to the increased radial plasma loss induced by the instabilities.

Figures 5.6 and 5.7 show the profiles of n and T_e for the same conditions as Fig. 5.5. The reduction of pressure and the onset of instability is accompanied by a reduction of central density and a broadening of the density profile, together with an increase in electron temperature. While it is difficult to separate the effects of pressure reduction and instability onset, it seems probable that the broadened density distribution, especially for Mode I, which is the more strongly excited, is attributable primarily to anomalous radial transport. The discharge becomes visibly more diffuse with the onset of both instabilities. Similar observations of the influence of instabilities on the steady state parameters have been reported by other authors.[66,77,96]

5.1.3. Determination of radial electric field

The parameter of most critical importance for our theory is the radial electric field, which can be obtained by differentiating the space potential ϕ_s. However, this is not directly measurable by a probe in a magnetoplasma, though the floating potential ϕ_f can be determined. To find the electric field, we must correct the measurements of ϕ_f for the sheath drop. The full procedure is discussed in detail in Section 4.1.3.

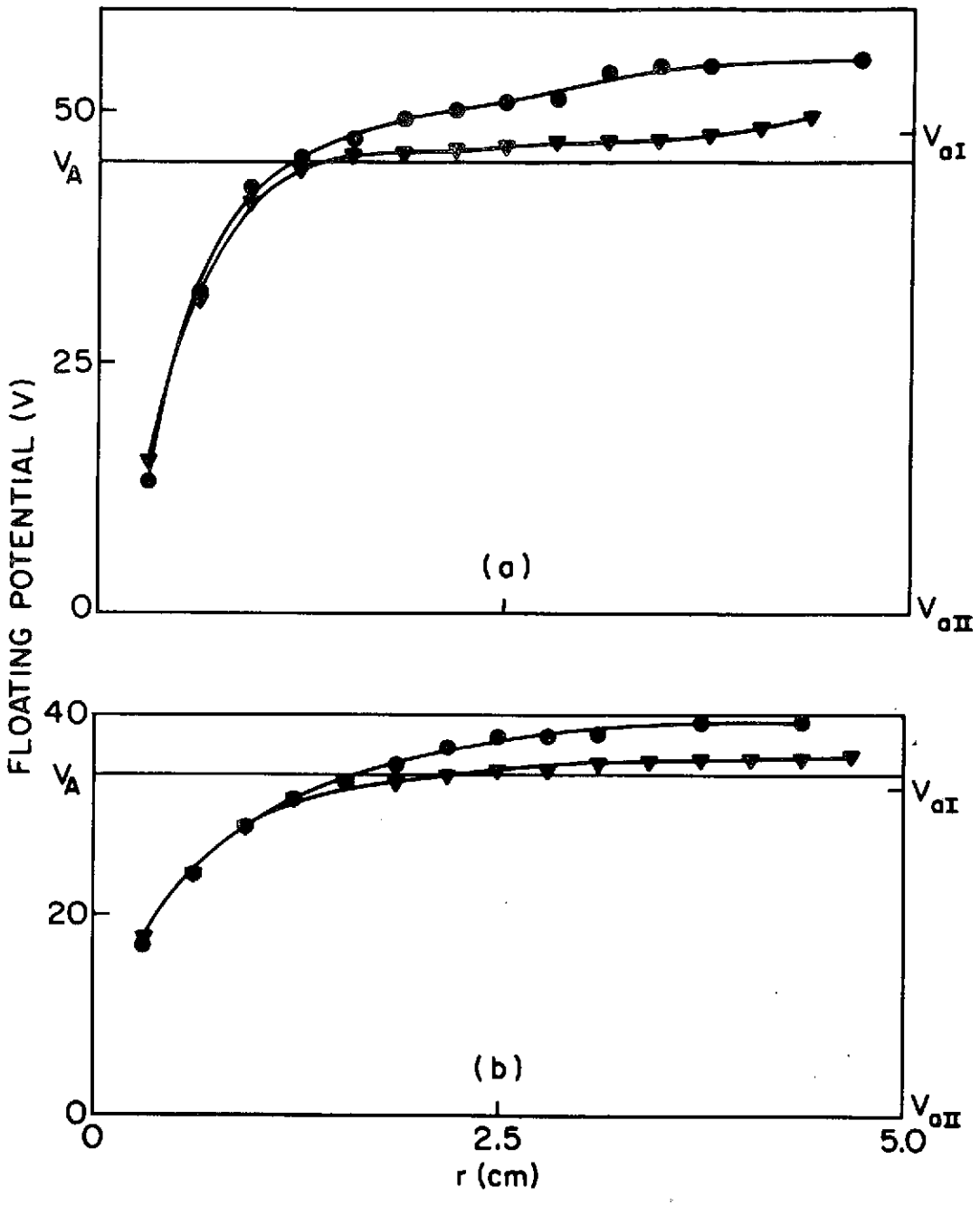

FIG. 5.5. The experimental radial variation of floating potential (a) with, and (b) without the presence of instabilities. V_A indicates the anode potential; V_{aI} and V_{aII} indicate starting anode potentials when floating and grounded, respectively; points ● and ▼ indicate floating and grounded starting anode, respectively. Discharge parameters are: (a) $p = 10^{-4}$ Torr, I = 10 A, B = 1.3 kG; (b) $p = 3 \times 10^{-4}$ Torr, I = 10 A, B = 1.3 kG.

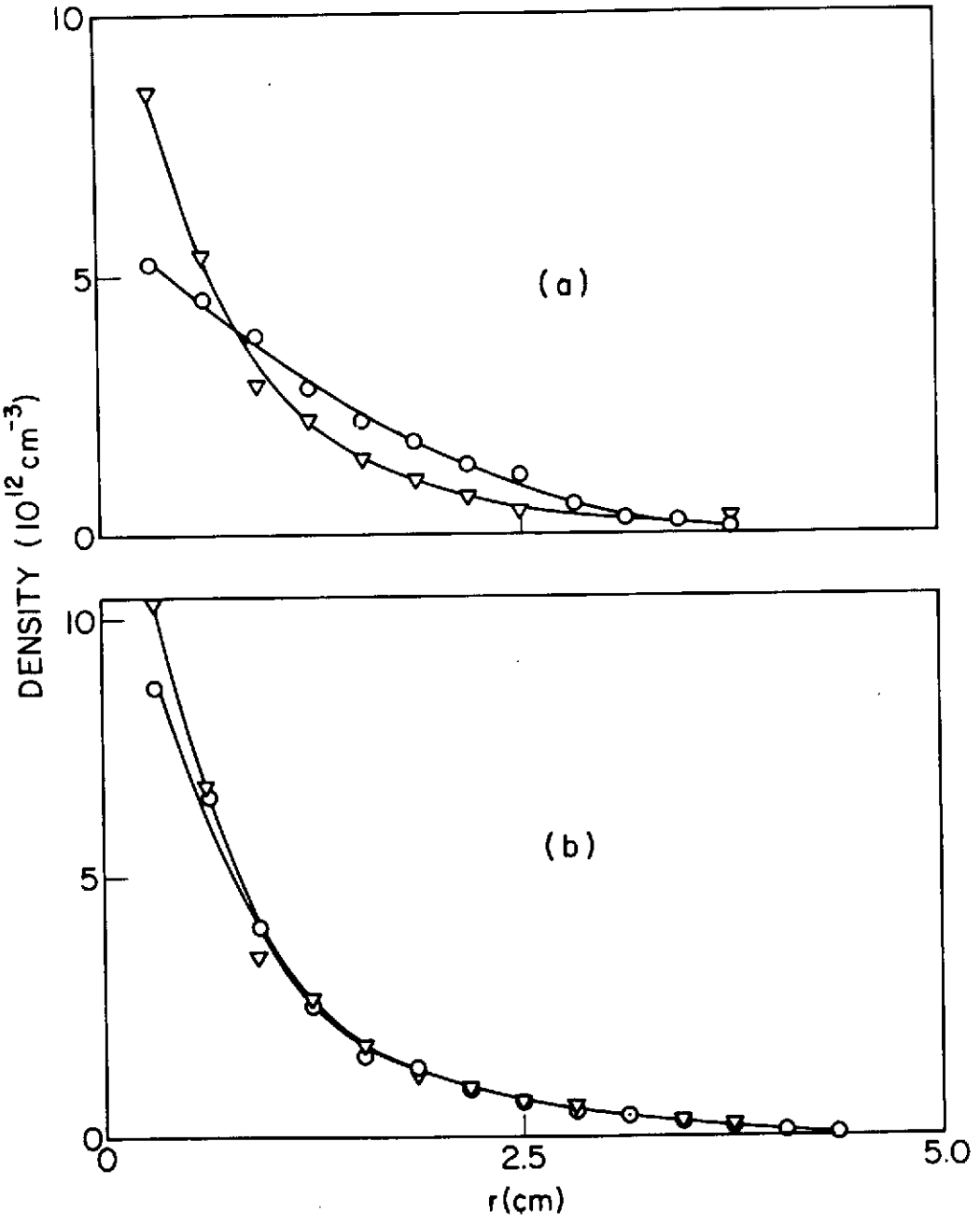

FIG. 5.6. The experimental plasma density radial variation, with starting anode (a) floating and (b) grounded. Points o indicate instability present, $p = 1.0 \times 10^{-4}$ Torr; ▽ no instability present, $p = 3 \times 10^{-4}$ Torr. Discharge parameters are: I = 10 A, B = 1.3 kG.

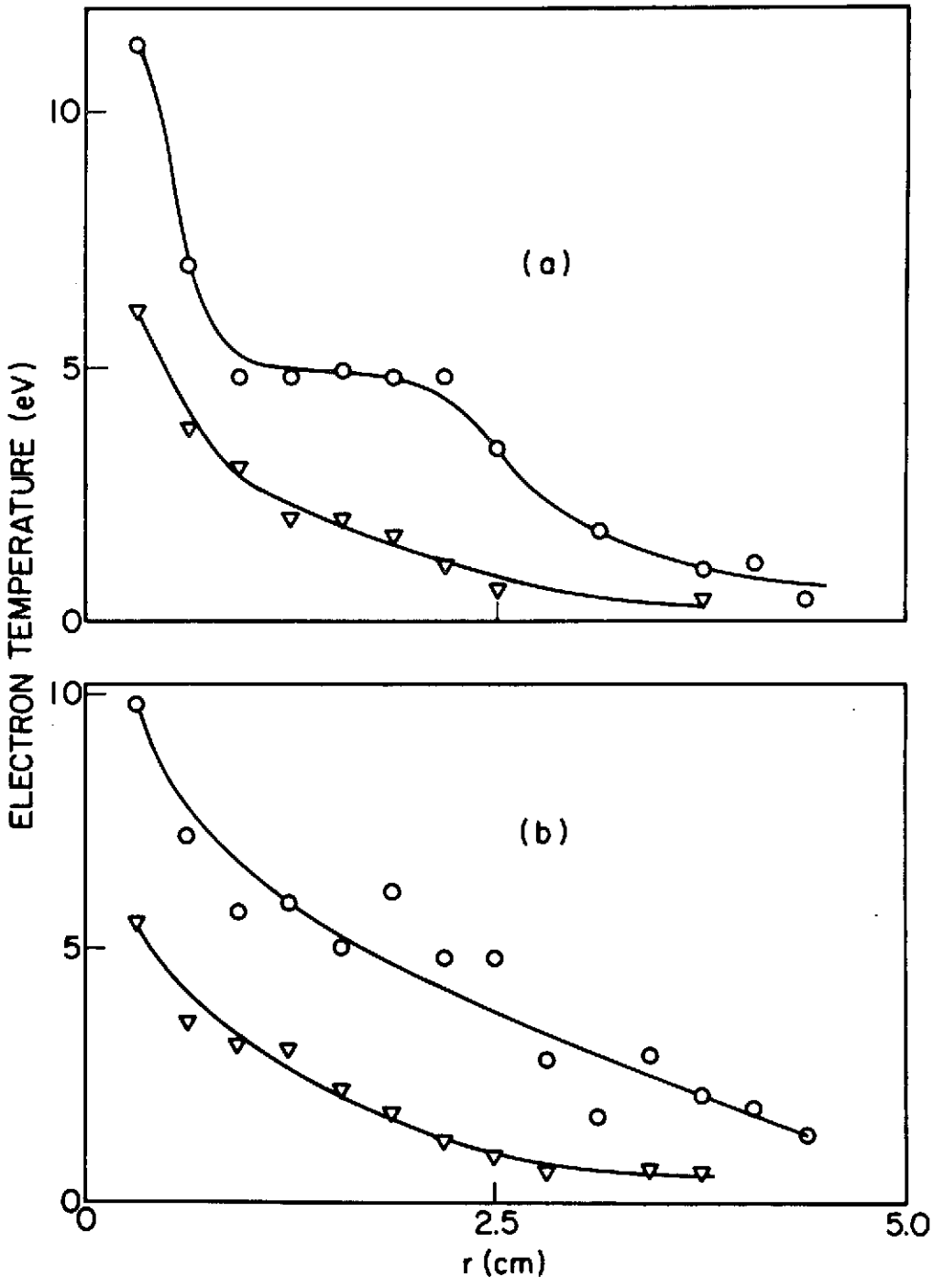

FIG. 5.7. The experimental radial variation of electron temperature with starting anode (a) floating, and (b) grounded. Discharge parameters and symbols are as in Fig. 5.6.

There is no precise calculated value available for the constant c in Eq. (4.2) for measurements in the presence of magnetic field, although a value of around 4 is often taken.[81] We have taken values of $c = 4$ and $c = 2$, and compared the results in Fig. 5.8, where we plot $-E/r$ proportional to the rotation frequency, as a function of radius. We plot $-E/r$ since a negative electric field corresponds to an $\underset{\sim}{E} \times \underset{\sim}{B}/B^2$ rotation in the right-hand sense. For Fig. 5.8 we have used the profiles of ϕ_f and T_e of Figs. 5.5 and 5.7 for the lower pressure, when the instabilities are present. It should be stressed that these curves must be considered only as approximate; they depend quite sensitively on the electron temperature measurements, and are subject to the errors of differentiation. We have not attempted to extend the determination of the electric field to very near the axis; there are large gradients in temperature and potential, and the measurements are less certain there. As symmetry dictates, the electric field tends to zero at the axis, and E/r tends to a constant value. The pronounced minimum of the $-E/r$ curve for Mode I is due primarily to the decrease of the electron temperature with radius after the plateau shown in Fig. 5.7. The apparent absence of this plateau, together with the flattening of the floating potential curve, causes the electric field for Mode II to be relatively uniform and slightly positive (negative rotation).

5.1.4. Influence of the electric field profile on the instabilities

It was suspected that Mode II might merge into Mode I if the starting anode potential were varied from zero to the value it assumes when floating (V_{aI} in Fig. 5.5). This was done, with the results that Mode II would disappear at a potential of several volts, and that Mode I would appear at about + 30 V. For potential profiles between those for the starting anode floating and grounded (see Fig. 5.8), the waves were stabilized.

Another method of influencing the excitation of Mode I was suggested by the fact that the starting anode floating potential was about 5% lower than V_A in the high pressure quiescent régime, and about 5% higher than V_A when the pressure was reduced to the value when Mode I appeared.

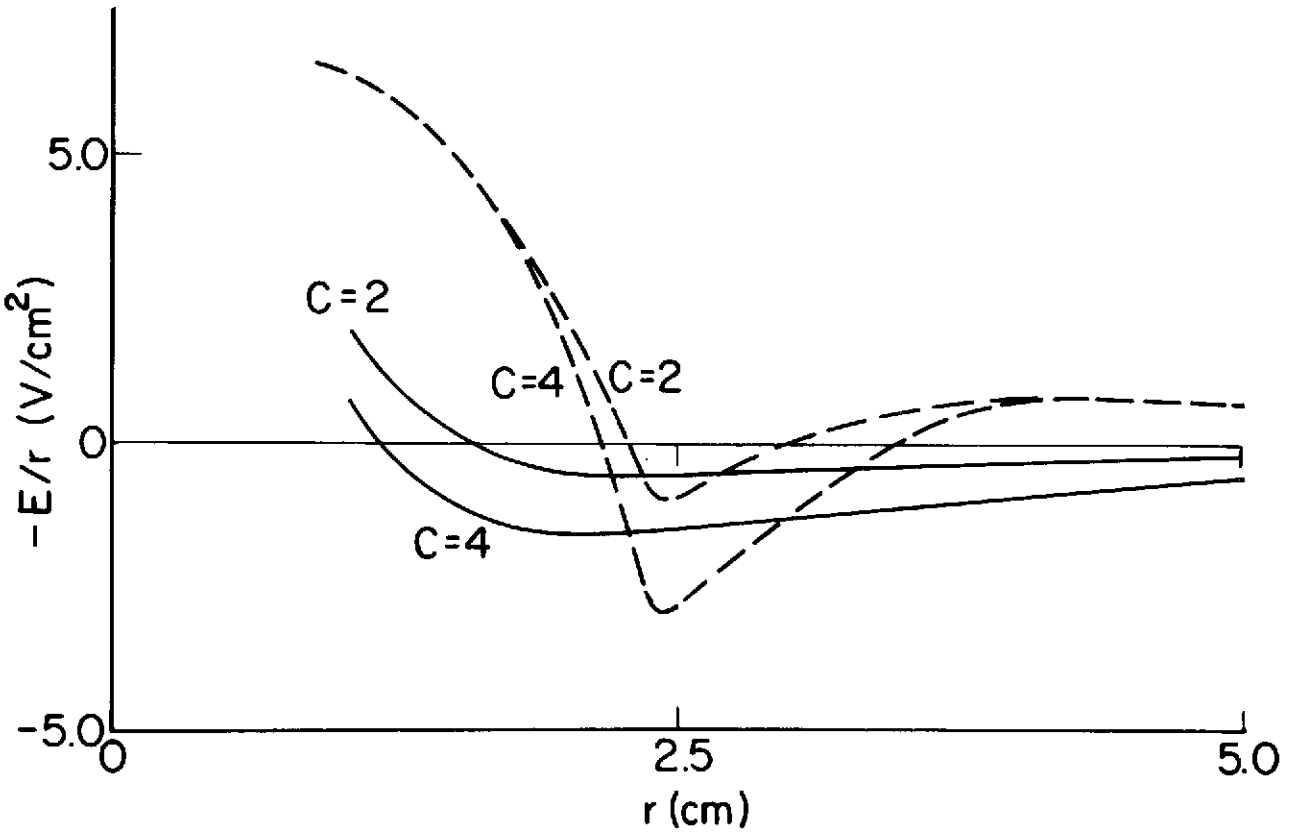

FIG. 5.8. Estimated electric field profiles in the presence of either Mode I (----), or Mode II (——), as determined from the experimental profiles of ϕ_f and T_e (Figs. 5.5 and 5.7) and Eq. (4.2).

The method consisted of setting the pressure at 2×10^{-4} Torr, so that the system was just quiescent, and increasing the starting anode potential from the floating value by about 5 V, at which point Mode I was excited at a frequency of 8 kHz. (This may be compared with 9 kHz under the standard conditions of 1.1×10^{-4} Torr with the starting anode floating). Its onset caused the pressure to decrease to 1.8×10^{-4} Torr. The radial profile of the amplitude of ϕ_1 had the same characteristic double-humped distribution as when the mode was excited under the standard conditions. Making the radial electric field more negative, by raising the starting anode potential, is evidently destabilizing for Mode I. It allows one to compensate for the stabilizing effect of increased pressure, and follow the instability threshold.

It was noted that the discharge would not run with the starting anode grounded for fields above about 2 kG. Furthermore, the stabilizing effect of increasing discharge current seemed to be sufficient to completely suppress Mode II at currents above 15 A. Thus, the $m = -1$ mode (Mode II) appears in a rather limited range of discharge parameters, whereas the $m = 1$ mode (Mode I) appears at fields above 0.5 kG under all discharge conditions, provided that the starting anode is allowed to float and the pressure is in the range $1 - 1.5 \times 10^{-4}$ Torr. The frequency of Mode I increased slightly at higher values of magnetic field and discharge current.

5.2. Theory

This section presents a brief outline of a theory for a fully ionized magnetoplasma model, together with a description of the numerical method of solving the resulting boundary value problem.[10,11] By resorting to a numerical solution which contains the experimental values of radial profiles of density and electric field, the spatial variations of amplitude and phase of potential and density fluctuations of two observed instabilities are predicted, and the instabilities are identified as centrifugal flute modes driven by the $\underset{\sim}{E} \times \underset{\sim}{B}/B^2$ drift in the presence of a density gradient, modified by the velocity shear due to non-uniform $\underset{\sim}{E} \times \underset{\sim}{B}/B^2$ rotation.

5.2.1. The model

We consider an infinitely long, collisionless plasma column immersed in a uniform axial magnetic field. The axially symmetric column is assumed to have a Gaussian number density profile and an arbitrary radial electric field. We assume no zero or first order axial variations in the column, i.e., $k_z = 0$. The waves are quasistatic, quasineutral, and low frequency ($\omega < \omega_{ci}$). The radial wave equation which describes these waves may be derived by using the two-species fluid equations[22] in the isothermal approximation. In using the fluid equations we neglect ion and electron collisions, electron inertia, and finite electron Larmor radius effects. The continuity equations for the electrons and ions are

$$\frac{\partial n}{\partial t} + \nabla_\perp \cdot (n \underset{\sim}{v}_{e,i}) = 0 \ . \tag{5.1}$$

The electron equation of motion is

$$0 = - \nabla_\perp (nT_e) - en(\underset{\sim}{E} + \underset{\sim}{v}_e \times \underset{\sim}{B}) \ , \tag{5.2}$$

while for the ions we have

$$nm_i \frac{d\underset{\sim}{v}_i}{dt} = - \nabla_\perp (nT_i) - \nabla_\perp \cdot \underset{\approx}{\pi}_i + en(\underset{\sim}{E} + \underset{\sim}{v}_i \times \underset{\sim}{B}) \ . \tag{5.3}$$

Here n is the number density, $\underset{\sim}{v}_{e,i}$ is the species velocity, $T_{e,i}$ is the species temperature in energy units, $\underset{\sim}{E}(= - \nabla_\perp \phi)$ is the electric field, $\underset{\sim}{B}$ is the magnetic field, m_i is the ion mass, and $\underset{\approx}{\pi}_i$ is the viscosity tensor. This collisionless viscosity tensor accounts for finite ion Larmor radius effects. In cylindrical geometry it can be written as[100]

$$\underset{\approx}{\pi}_{i\perp} = \frac{nT_i}{\omega_{ci}} \underset{\approx}{\alpha} \ , \quad \underset{\approx}{\alpha} = \begin{pmatrix} \alpha_{rr} & \alpha_{r\theta} \\ \alpha_{\theta r} & \alpha_{\theta\theta} \end{pmatrix} , \tag{5.4}$$

where

$$\alpha_{rr} = -\alpha_{\theta\theta} = -\frac{1}{2}\left(r\,\frac{\partial(v_{i\theta}/r)}{\partial r} + \frac{1}{r}\,\frac{\partial v_{ir}}{\partial\theta}\right),$$

$$\alpha_{r\theta} = \alpha_{\theta r} = \frac{1}{2}\left(-\,r\,\frac{\partial(v_{ir}/r)}{\partial r} + \frac{1}{r}\,\frac{\partial v_{i\theta}}{\partial\theta}\right). \tag{5.5}$$

We perturb the variables n, $\underset{\sim}{v}_{e,i}$ and ϕ in the form $n(r,t) = n_0(r) + n_1(r)\exp i(\omega t - m\theta)$, and eliminate among the resulting first order equations to obtain the radial wave equation[10]

$$\frac{d^2\psi}{dr^2} + \left(\frac{3}{r} - \frac{2r}{r_0^2} + \chi\right)\frac{d\psi}{dr} - \frac{m^2-1}{r^2}\,\psi - \frac{2}{r_0^2}\left(\frac{\omega^2}{(\omega-m\omega_E+m\omega_{di})(\omega-m\omega_E)}\right)\psi = 0\ , \tag{5.6}$$

where

$$\psi(r) = \frac{m\phi_1(r)}{rB(\omega-m\omega_E)}\ , \qquad n_0 = N\exp\left(-\frac{r^2}{r_0^2}\right),\ \omega_E(r) = \frac{-E_0(r)}{rB}\ ,$$

$$\omega_{di} = \frac{2T_i}{eBr_0^2}\ ,\quad \chi = -2m\,\frac{d\omega_E}{dr}\,\frac{\left(\omega-m\omega_E+m\omega_{di}/2\right)}{(\omega-m\omega_E+m\omega_{di})(\omega-m\omega_E)}\ . \tag{5.7}$$

Here, ω_E is the rotation frequency due to the $\underset{\sim}{E}\times\underset{\sim}{B}/B^2$ drift and may be positive or negative. The diamagnetic drift frequency of the ions, ω_{di}, is a negative constant for a Gaussian density profile and uniform ion temperature. In deriving this equation we used a simple relation between the perturbed density, n_1, and the perturbed potential, ϕ_1, as obtained from the electron equations alone, i.e. Eqs. (5.1) and (5.2). This relation is

$$\frac{2m}{Br_0^2}\,\phi_1 = (\omega-m\omega_E)\,\frac{n_1}{n_0}\ , \tag{5.8}$$

which can also be written as

$$\frac{e\phi_1}{T_i} = \frac{\omega-m\omega_E}{m\omega_{di}}\left(\frac{n_1}{n_0}\right). \tag{5.9}$$

Note that the electron temperature has cancelled out of the combined electron equations, i.e., Eq. (5.8). Thus, these waves do not depend on the electron temperature, even if it varies radially. This is true even if T_e is treated as a perturbed variable.[10] The result is an important simplification since the experimental set-up we are modeling does have a radial electron temperature variation.

5.2.2. Method of solution

Before we can solve Eq. (5.6), we must specify the boundary conditions. The equation has a regular singularity at the origin, so we must use the nonsingular solution. The second boundary condition is applied at the outer boundary ($r = a$) and is $\psi(a) = 0$. This is dictated by the fact that experimentally $n_1 = \phi_1 = 0$ at $r = a$, so by Eq. (5.7) $\psi(a) = 0$. Note that Eq. (5.9) demands that both n_1 and ϕ_1 be zero if one of them is.

To study cases where the rotation is not uniform, i.e. the electric field is not a linear function of radius, we must solve the radial wave equation [Eq. (5.6)] numerically. To do this, we have modified a predictor-corrector computer routine for solving ordinary differential equations to include complex eigenfunctions. In order to eliminate the singular solution we begin the numerical integration near the origin with the form of the nonsingular solution, i.e., $\psi \propto r^{m-1}$, and integrate outwards. We also integrate Eq. (5.6) inward from the outer radial boundary, using the boundary conditions $\psi(a) = 0$ and $d\psi/dr\big|_a = \psi'(a) = \text{constant}$. We then compare the values of ψ'/ψ from both integrations at some intermediate position. If they agree, we have found a proper eigenfrequency, ω, and we also have the eigenfunction. If they do not agree, we must guess a new eigenfrequency and integrate again. An interpolation procedure is used to converge on the proper eigenfrequency. Once we have the eigenfunction, we may use the definition of ψ [Eq. (5.7)] and Eq. (5.9) to find the radial forms of ϕ_1 and n_1, the two quantities which are measured experimentally.[10,11]

5.3. Comparison between Theory and Experiment

Comparison between theory and experiment is complicated by the difficulty of obtaining reliable measurements of the electric field, as mentioned in Sections 4.1.3. and 5.1.3. However, the measurements are consistent as to the basic forms of the electric field, and using approximations to them we can explain both the m = 1 and m = -1 instabilities observed experimentally, including good correlations between measured and computed eigenfunctions of density and potential.

To compare the theory and experiment in more detail, we have computed the eigenfunctions of density and potential as described in Section 5.3. The experimental parameters used in this calculation include a Gaussian number density profile with $r_0 = 2.2$ cm, and an ion temperature of 3 eV. The density profile is a good approximation to the measured data of Fig. 5.6, and although the ion temperature was not directly measured, there has been experimental evidence for values of this order.[85]

Due to uncertainty in the electric field measurements, the choice of the electric field profile used in the calculation was guided by the shape of the experimental curves in Fig. 5.8, and the profile which gave the best agreement between the theoretical and experimental eigenfunctions. The profiles selected, shown in Fig. 5.9 for both Modes I and II, are similar to the experimental curves of Fig. 5.8. For reference, the initial slope of the Mode I electric field profile of Fig. 10 is 4 V/cm^2 .

The computed eigenfunctions for the perturbed potential, ϕ_1 , and perturbed density, n_1 , for Mode I are shown in Figs. 5.10(a) and (b). They are to be compared to the measured eigenfunctions shown in Figs. 5.3(a) and (b). The forms of the two sets of curves are very similar. The potential amplitude has a two-humped profile for both the theoretical and the experimental curves, the inner maximum being larger. There is also a large phase-shift associated with the minimum in the potential curve. Given that n_1/n_0 varies slowly with radius [Figs. 5.6 and 5.10(b)], we can see from Eq. (5.9) that the potential profiles are controlled by the value of $(\omega-\omega_E)$. Thus the minimum in $|\phi_1|$, and the large phase shift, occur where $(\omega-\omega_E)$ has a minimum. There is also good agreement with the profile of n_1 . It has a single maximum close to the center of the column and a gradual phase-shift near the outer

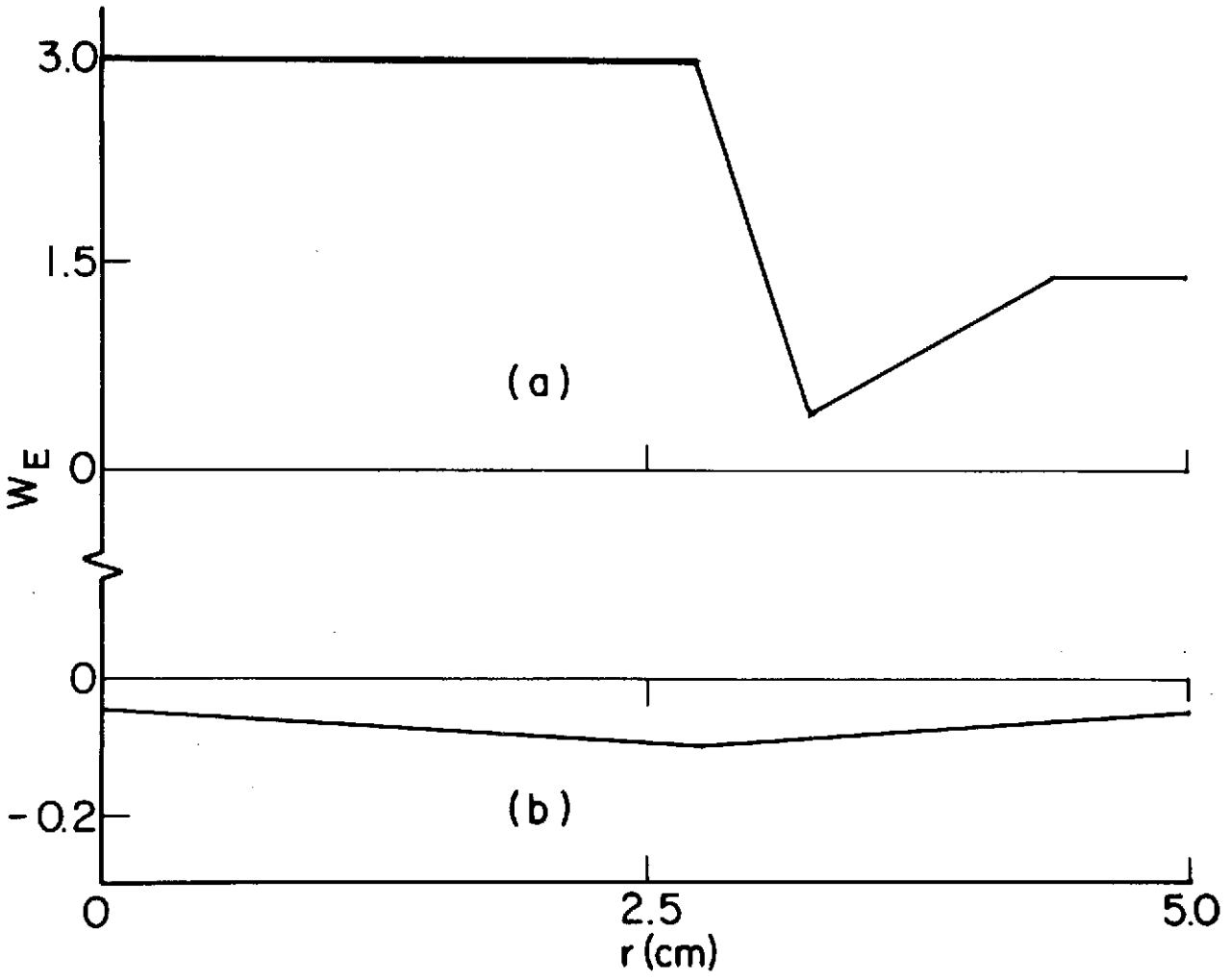

FIG. 5.9. Profiles of the rotation frequency, $w_E (= \omega_E/\omega_{di})$, due to the electric field, used to calculate the theoretical eigenfunctions from Eq. (5.6) for (a) Mode I, and (b) Mode II.

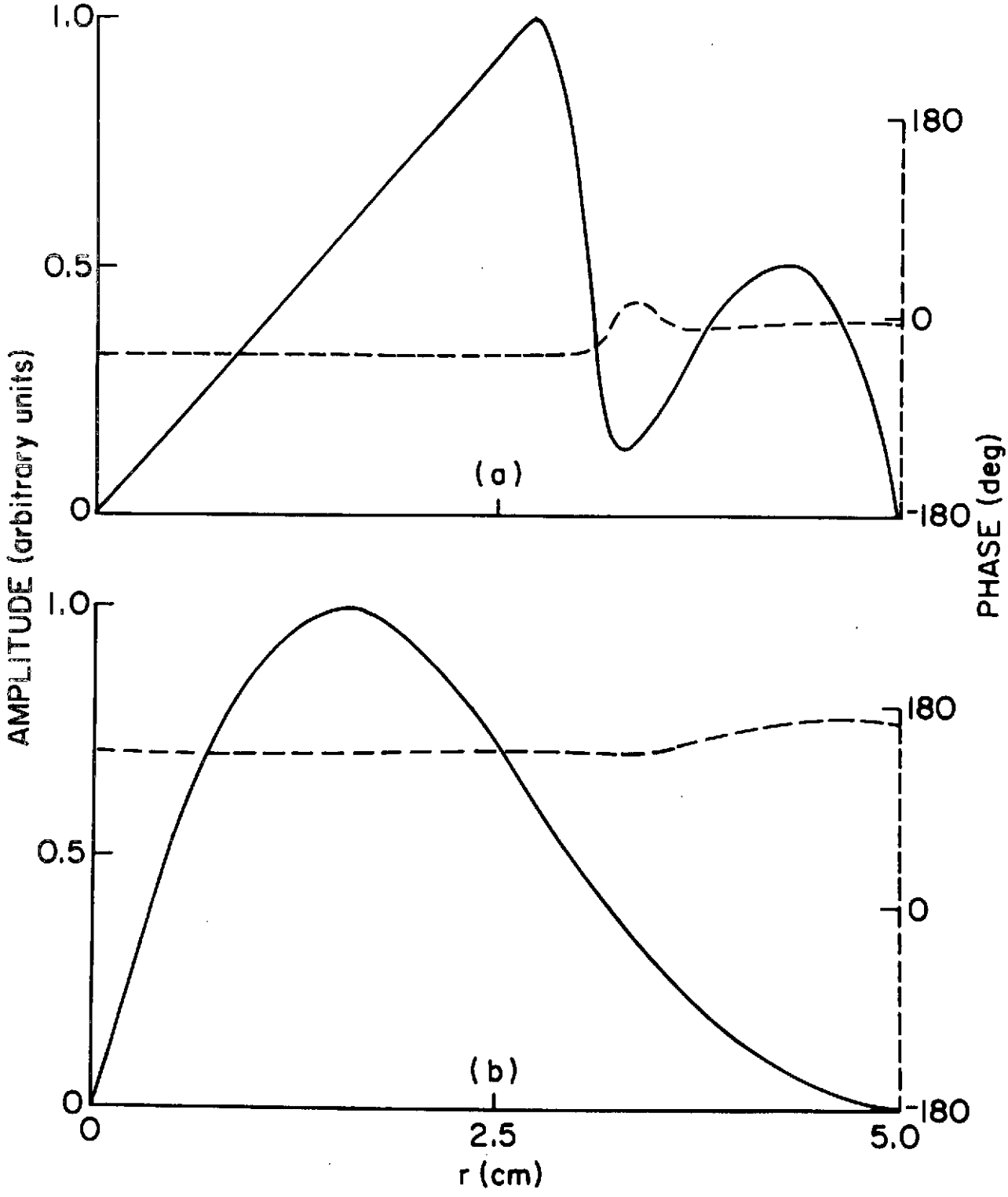

FIG. 5.10. Calculated eigenfunctions of (a) the potential, ϕ_1 , and (b) the density, n_1 , for Mode I (m = 1). Comparison to be made with the experimental eigenfunctions in Fig. 5.3.

——— amplitude; ------ phase.

boundary. The phase-shift between n_1 and ϕ_1 is in fair agreement with theory, the theoretical value being about 25% higher than the experimental value. The computed eigenfrequency is $\omega = (0.18 - i\ 0.24)\omega_{di}$ which gives a real frequency of $\sim$ 3 kHz as compared to an observed value of $\sim$ 9 kHz. However, in a rotating plasma the frequency is a very sensitive function of the electric field, a parameter that we could not measure accurately. This frequency is determined approximately by a weighted integral of ω_E from the origin to the outer boundary.[101] Also, especially for the m = 1 mode, the frequency is sensitive to the exact position of the radial boundary. In fact, if we assume that the wave amplitudes go to zero at r = 4.5 cm, rather than r = 5 cm, the frequency roughly doubles. Equivalently, the frequency doubles if we take a slightly more diffuse density profile with $r_0 \approx 2.5$ cm, instead of $r_0 = 2.2$ cm. Thus we do not consider the frequency discrepancy as serious.

For the m = -1 mode, a small, positive electric field will cause instability, which is indeed the type of profile we observe for this mode. We have reasoned that decreasing the potential at the discharge boundary is the cause of this field reversal. The electric field profile taken for Mode II, shown in Fig. 5.9, implies nearly uniform rotation. The other experimental parameters are the same as for the m = 1 mode. The computed eigenfunctions are shown in Figs. 5.11(a), (b), and should be compared with the experimental curves of Figs. 5.4(a),(b). In contrast to the m = 1 mode, both the experimental and theoretical potential profiles now have a single maximum located nearer the outer boundary. The phase shift is more spread out, and can again be attributed to the behavior of $(\omega-\omega_E)$, as seen from Eq. (5.9). The density has its maximum nearer the center, with only a gradual phase shift. The phase shift between n_1 and ϕ_1 is only about half of that measured. The computed eigenfrequency is $\omega = (0.10 - i\ 0.05)\ \omega_{di}$ which gives a real frequency of $\sim$ 2 kHz compared to an observed value of $\sim$ 7 kHz. This is consistent with the low value of frequency calculated for the m = 1 mode as discussed above.

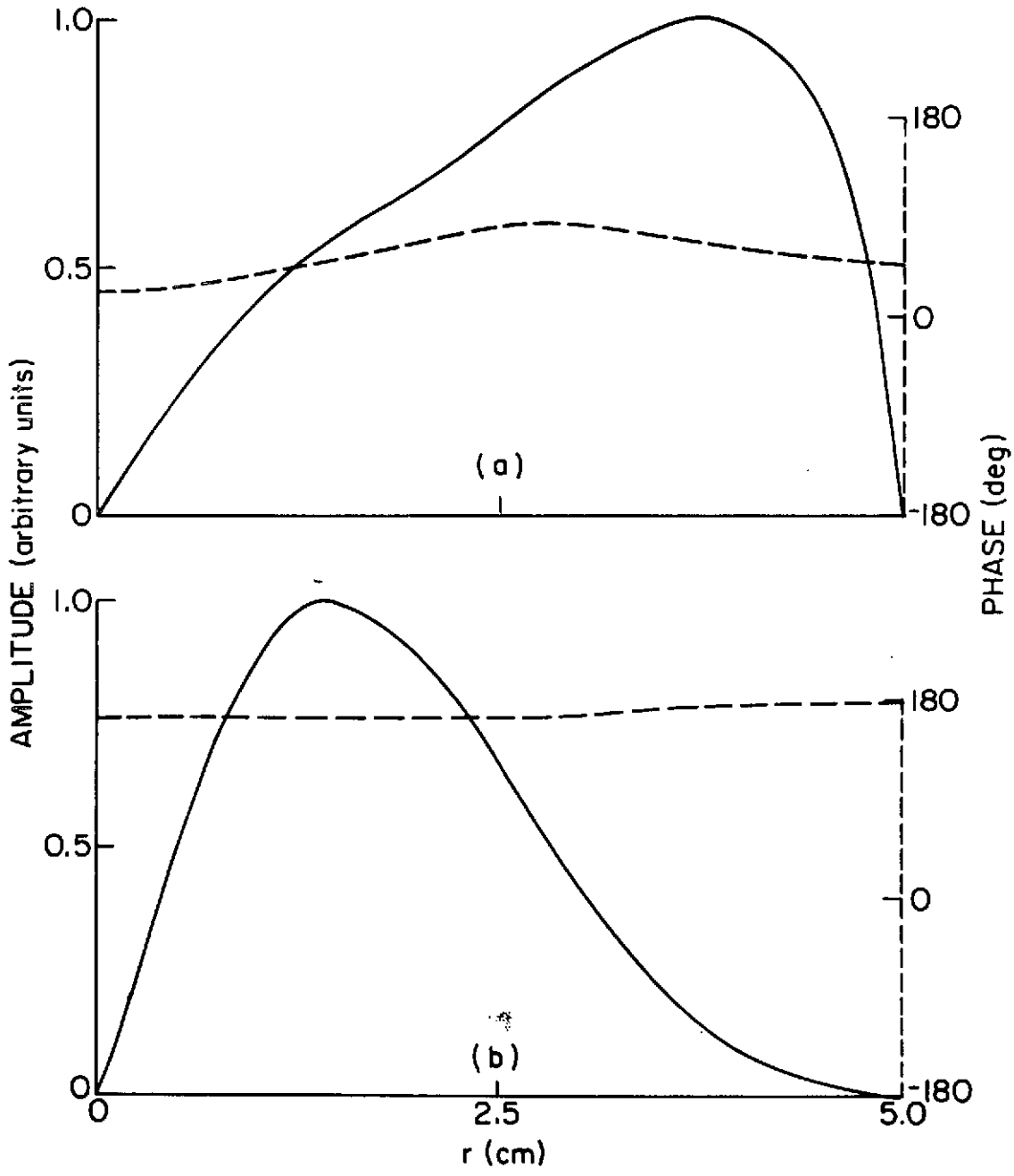

FIG. 5.11. Calculated eigenfunctions of (a) the potential, Φ_1, and (b) the density, n_1, for Mode II (m = -1). Comparison to be made with the experimental eigenfunctions in Fig. 5.4. ——— amplitude; ----- phase.

5.4. Discussion

From the results of Section 5.3., it is seen that the theory of Section 5.2. can reproduce the salient features of the two instabilities that we observe in the HCD and report here. Since the modes are not localized to a small radial portion of the column, we have not used a local approximation. Instead, we have treated the problem in cylindrical geometry and computed the eigenfunctions. The discrepancies between the theory and the experiment are in the precise values of certain quantities, particularly frequency and phase shift, rather than the qualitative behavior of the instabilities. In part, this may be due to the fact that the instabilities which we measure are nonlinearly saturated, while the theory considers only linear effects. In addition, we are working with a strong radial electric field (up to $\sim$ 10 V/cm); for the parameters of our experiment this implies that the $\underset{\sim}{E} \times \underset{\sim}{B}/B^2$ velocity is of the order of the ion thermal velocity. Thus, the ions do not act strictly like a guiding-center fluid: we believe it is this effect which makes the ion temperature appear to be as high as $\sim$ 3 eV, and gives the observed finite Larmor radius stabilization. Although a more precise determination of this effect would require a kinetic theory to accurately describe the ion orbits, we believe that the experimental and theoretical agreement shown here demonstrates that fluid theory accounts for the basic features of the instability. Good agreement has also been found between observed and calculated eigenfunctions for Kelvin-Helmholtz instabilities in other experiments[101] where the fluid description of the ions is not strictly justifiable. In this connection, it may be noted that while our rotation is nonuniform, especially for the m = 1 mode, we regard the velocity shear as modifying the simple centrifugal flute mode for uniform rotation, rather than giving rise to a Kelvin-Helmholtz type instability due to velocity shear. This is supported by the fact that the eigenfunction amplitudes do not have a maximum in the shear region, as in the Kelvin-Helmholtz instability used to explain edge-oscillations in Q-machines.[101]

While our theory neglects collisions, it seems probably that ion-neutral collisions are not entirely negligible under our conditions.

The important parameter here is ν_i/ω_{ci}, where ν_i is the effective ion-neutral collision frequency for momentum transfer. It is difficult to estimate ν_i in the various experiments with any precision, in view of the uncertainties of the ion distribution and the neutral concentration in the arc. On general grounds, we may expect ion collisions to have the following effects: as ν_i/ω_{ci} is increased from zero, the collisionless orbits will become increasingly disrupted as ν_i/ω_{ci} becomes comparable with unity. This would lessen the importance of ion inertia and centrifugal effects in causing a destabilizing ion drag relative to the electrons, and with it the finite Larmor radius stabilizing effect, and replace it by a destabilizing ion drag due to collisions. This hypothesis is supported by our observation that as the pressure is raised from $p = 1.0 \times 10^{-4}$ Torr, where we observe the m = 1 mode, the instability is quenched at $p \sim 2 \times 10^{-4}$ Torr, while at $p \sim 4\text{-}5 \times 10^{-4}$ Torr another one sets in. This, however, we have not investigated in detail.

A generalized theory is required, including both collisionless and collisional effects. It might be expected to disclose the transition between the two types of instability as the pressure is varied. It is also clear that to identify the instabilities of the HCD unequivocally, detailed consideration must be given to the critical steady-state parameters of neutral pressure, radial electric field profile and ion temperature.

6. CONCLUSIONS

We have presented a study of the positive column and the hollow cathode discharge (HCD), with an emphasis on the steady-state characteristics and low-frequency instabilities excited by sources of free energy in the two plasmas. A theory for the steady state of the positive column in the transition from the collisionless (low pressure) to collisional (intermediate pressure) régime was presented in Section 2. It is based on three moments of the Boltzmann equation in the presence of static axial magnetic field and axial current. In addition to the results obtained by the isothermal (two moment) theories,[3] Section 2 gave the radial profiles of electron and ion temperatures and demonstrated the similarity laws for the positive column. Good agreement between the calculated and measured similarity laws was shown for He. The ion temperature was shown to vary significantly with radius: it increases from close to neutral temperature near the axis to about 1 eV near the wall in He.[5]

Another aspect of the theory of the steady state of the positive column was treated in the Appendix, where it was shown that the results of isothermal theory for an infinitely long column can be easily applied to the column of finite length. This is important for the case of a magnetized column at low pressures, where the axial motions of charged particles are collisionless, while their radial motions are effectively collision-dominated, due to the confining effect of magnetic field. The axial end effects in such cases may be important, even though the column is physically much longer than its radius.[6]

The time-dependent characteristics of the positive column were considered in Section 3 through a study of the excitation characteristics of the ion acoustic instability driven by the axial current. Analysis based on a linearized kinetic model, with zero order discharge characteristics given by the results of Section 2, was shown to predict a convective instability (spatial amplification). The calculated spatial growth rate shows frequency dependence similar to the amplitude spectra of ion acoustic waves near the instability boundary, measured in our positive column experiments in He and Ar. The importance of ion Landau damping of the wave for typical experimental conditions was also demonstrated.

The literature dealing with HCD was reviewed in Section 4, and it was shown that measurements of steady-state and time-dependent characteristics are often incomplete. Furthermore, the theoretical models used in identifying the various observed instabilities are often so idealized that they cannot apply to the HCD. Section 5 presents results of meaurements of steady-state characteristics of our HCD, together with detailed observations of two low-frequency instabilities. The instabilities are identified as centrifugal flute modes, driven by Hall drift in the presence of radial density gradient and non-uniform radial electric field. The identification is based on the agreement of calculated and observed frequencies, azimuthal mode numbers, and radial profiles of phases and amplitudes of density and potential fluctuations.

The research presented in this work has led to an increased understanding of the basic processes which determine the steady-state and time-dependent characteristics of the two plasma sources. Specific suggestions for further work were given at the ends of the respective sections (e.g., Sections 2.4., 3.4., 4.3. and 5.4.). Especially important within the context of this work would be further experimental and theoretical studies of the processes by which the energy of electron drift motion is dissipated into increasing the energy of random motion of charged particles in the two plasma sources, i.e., into plasma turbulence and heating. For example, a promising direction for further research would be the investigation of how high axial current, perhaps in the form of a pulse, would affect the characteristics of plasma.

REFERENCES

1. L. Tonks and I. Langmuir, Phys. Rev. 34, 876 (1929).

2. W. Schottky, Phys. Z. 25, 635 (1924).

3. H. N. Ewald, F. W. Crawford and S. A. Self, J. Appl. Phys. 38, 2753 (1967).

4. A. J. Duncan, J. R. Forrest, F. W. Crawford and S. A. Self, Phys. Fluids 14, 1959 (1971).

5. D. B. Ilić, J. Appl. Phys. (to appear September 1973).

6. D. B. Ilić and S. A. Self, J. Appl. Phys. 43, 2620 (1972) [appended].

7. H. Lehnert, Plasma Phys. 9, 301 (1967).

8. J. S.Luce, Proceedings of the Second United Nations Conference on Peaceful Uses of Atomic Energy, (United Nations, Geneva, 1958), vol. 31, p. 305.

9. Conference on Hollow-Cathode Discharges and Their Applications, (Laboratoire de Physique des Plasmas, Université Paris - Sud Orsay, 1971).

10. T. D. Rognlien, Institute for Plasma Research Report No. 487, Stanford University, October 1972.

11. D. B. Ilić, T. D. Rognlien, S. A. Self, and F. W. Crawford, Phys. Fluids (to appear August 1973).

12. J. V. Parker, Phys. Fluids 6, 1657 (1963).

13. S. A. Self, J. Appl. Phys. 36, 456 (1965).

14. G. Francis in Handbuch der Physik, edited by S. Flügge (Springer Verlag, Berlin, 1956), Vol. 22, p. 53.

15. K.-B. Persson, Phys. Fluids 5, 1625 (1962).

16. E. R. Mosberg, Jr. and K.-B. Persson, Phys. Fluids 7, 1829 (1964).

17. G. S. Kino and E. K. Shaw, Phys. Fluids 9, 587 (1966).

18. S. A. Self and H. N. Ewald, Phys. Fluids 9, 2486 (1966).

19. J. R. Forrest and R. N. Franklin, Brit. J. Appl. Phys. 17, 1061 and 1569 (1966).

20. S. A. Self, Phys. Fluids 10, 1569 (1967).

21. G. Ecker and O. Zöller, Phys. Fluids 7, 1996 (1964).

22. S. I. Braginskii, in Reviews of Plasma Physics, edited by M. A. Leontovich (Consultants Bureau, New York, N. Y., 1965), Vol. I, p. 205.

23. J. R. Forrest and R. N. Franklin, J. Phys. D 1, 1357 (1968).

24. S. C. Brown, Basic Data of Plasma Physics (MIT Press, Cambridge, Mass., 1965).

25. A. von Engel, Ionized Gases (Clarendon Press, Oxford, 1965).

26. B. Klarfeld, J. Phys. USSR 5, 155 (1941); Techn. Phys. USSR 4, 44 (1937).

27. N. A. Karelina, J. Phys. USSR 6, 218 (1942).

28. R. J. Bickerton and A. von Engel, Proc. Phys. Soc. (London) 69B, 468 (1956).

29. P. F. Little and H. G. Jones, Proc. Phys. Soc. (London) 85, 969 (1965).

30. L. B. Loeb, The Kinetic Theory of Gases (Dover Publications, Inc., New York, N. Y., 1961).

31. A. J. Duncan and J. R. Forrest, Phys. Fluids 14, 1973 (1971).

32. J. R. Forrest and R. N. Franklin, J. Phys. D 2, 471 (1969).

33. H. N. Ewald, F. W. Crawford and S. A. Self, Phys. Fluids 12, 303, 316 (1969).

34. S .A. Self, J. Plasma Phys. 4, 44 (1970).

35. V. Arunasalam and S. C. Brown, Phys. Rev. 140, A471 (1965).

36. H. Tanaca, A. Hirose and M. Koganei, Phys. Rev. 161, 94 (1967).

37. A. A. Zaitsev, B. Milić, A. A. Rukhadze and B. N. Shvilkin, Zh. Tekh. Fiz. 38, 229 (1968) [Sov. Phys. Tech. Phys. 13, 166 (1968)].

38. B. Milić and A. A. Rukhadze, Zh. Tekh. Fiz. 37, 1607 (1967).

39. M. Fujiwara, M. Raether and M. Yamada, J. Phys. Soc. Japan 27, 758 (1968).

40. D. B. Fenneman, M. Raether and M. Yamada, Bull. Am. Phys. Soc. 17, 1010 (1972); Phys. Fluids 16, 871 (1973); M. Yamada, Ph.D. Thesis, University of Illinois, Urbana, Ill., June 1973.

41. P. C. Clemmow and J. P. Dougherty, Electrodynamics of Particles and Plasmas (Addison-Wesley Publishing Company, Reading, Mass.,1969).

42. T. D. Rognlien and S. A. Self, J. Plasma Phys. 7, 13 (1972).

43. R. J. Briggs, Electron-Stream Interaction with Plasmas (MIT Press, Cambridge, Mass., 1964).

44. H. Derfler, Phys. Rev. A1, 1467 (1970).

45. H. Derfler and T. C. Simonen, Phys. Fluids 12, 269 (1969).

46. S. A. Self and C. H. Shih, Phys. Fluids 11, 1532 (1968).

47. J. G. Laframboise, University of Toronto Institute for Aerospace Studies Report No. 100, Toronto, Ont., Canada, June 1966.

48. F. F. Chen, in Plasma Diagnostic Techniques, edited by R. H. Huddlestone and S. L. Leonard (Academic Press Inc., New York, N. Y., 1965), Ch. 4.

49. I. Alexeff and W. D. Jones, Phys. Letters. 20, 269 (1966).

50. L. C. Woods, J. Fluid Mech. 23, 315 (1965).

51. F. W. Crawford and G. S. Kino, Proc. IRE 49, 1767 (1961).

52. B. B. Kadomtsev, Plasma Turbulence (Academic Press, New York, N.Y., 1965).

53. R. Z. Sagdeev and A. A. Galeev in Nonlinear Plasma Theory, edited by T. M. O'Neil and D. L. Book (W. A. Benjamin, Inc., New York, N.Y., 1969).

54. R. C. Davidson, Methods in Nonlinear Plasma Theory (Academic Press, New York, N. Y., 1972).

55. S. A. Self, Institute for Plasma Research Report No. 403, Stanford University, December 1970.

56. L. I. Rudakov and V. N. Tsytovich, Plasma Phys. 13, 213 (1971).

57. K. Nishikawa and C.-S. Wu, Phys. Rev. Letters 23, 1020 (1969).

58. A. Sleeper, J. Weinstock and B. Bezzerides, Phys. Rev. Letters 29, 343 (1972).

59. S. M. Hamberger and J. Jancarik, Phys. Fluids 15, 825 (1972).

60. C. M. Surko, R. E. Slusher, D. R. Moler and M. Porkolab, Phys. Rev. Letters 29, 81 (1972).

61. S. Watanabe and H. Tanaca, Nucl. Fusion 12, 593 (1972).

62. C. N. Judice, J. F. Decker and R. A. Stern, Phys. Rev. Letters 30, 267 (1973).

63. L. M. Lidsky, S. D. Rothleder, D. J. Rose, S. Yoshikawa, C. Michelson and R. J. Mackin, Jr., J. Appl. Phys. 33, 2490 (1962).

64. D. A. Huchital and J. D. Rigden, Rev. Sci. Inst. 39, 1472 (1968).

65. W. C. Jennings, J. H. Noon and E. H.Holt, Rev. Sci. Inst. 41, 322 (1970).

66. D.L. Flannery and S. C. Brown, Phys. Fluids 13, 1066 (1970).

67. B. E. Keen and R. V. Aldridge, Plasma Phys. 12, 839 (1970).

68. H. De Kluiver, H. W. Piekaar, W. R. Rutgers, H. Schrijver and B. De Groot, Proc. Fourth International Conference on Plasma Physics and Controlled Thermonuclear Research (I.A.E.A., Vienna, 1971), Vol. II, p. 67.

69. D. L. Morse, Phys. Fluids 8, 516 (1965).

70. J. L. Delcroix, H. Minoo and A. R. Trindade, J. Phys. 29, 605 (1968).

71. A. Lorente-Arcas, Plasma Phys. 14, 651 (1971).

72. J. L. Delcroix, H. Minoo and A. R. Trindade, Rev. Sci. Instr. 40, 1555 (1969).

73. R. L. Gunshor, J. H. Noon and E. H. Holt, Phys. Fluids 11, 1763 (1968).

74. K.Chung and K. Huang, Proceedings of the Conference on Hollow-Cathode Discharges and Their Applications, (Laboratoire de Physique des Plasmas, Université Paris - Sud, Orsay,1971), p. 35.

75. P. J. Blaas, K. L. Buisman and H. De Kluiver, Ann. Phys. 24, 173 (1970).

76. J. C. Woo and D. J. Rose, Phys. Fluids 10, 893 (1967).

77. K. Chung and D. J. Rose, Proceedings of the Symposium on Turbulence of Fluids and Plasmas (Polytechnic Press, Brooklyn, N. Y.,1968), p. 311.

78. C. B. Kretschmer, F. Boeschoten and L. J. Demeter, Phys. Fluids 11, 1050 (1968).

79. R. V. Aldridge and B. E. Keen, Plasma Phys. 12, 1 (1970).

80. I. G. Brown, A. B. Compher and W. B. Kunkel, Phys. Fluids 14, 1377 (1971).

81. M. Hudis and L. M. Lidsky, J. Appl. Phys. 41, 5011 (1970).

82. P. Blanc, P. Deschamps and M. Occhionorelli, Los Alamos Report LA-4431-TR, Los Alamos Scientific Laboratory, Los Alamos, New Mexico, March 1971.

83. R. F. Kemp and J. M. Sellen, Jr., Rev. Sci. Inst. 37, 455 (1966).

84. M. Hudis, K. Chung and D. J. Rose, J. Appl. Phys. 39, 3297 (1968).

85. B. Van Der Sijde and P. A. W. Tielemans, Proceedings of the Tenth Conference on Physics of Ionized Gases, (Donald Parsons & Co., Ltd., Oxford, 1971) p. 192.

86. S. L. Leonard, Proceedings of the Ninth Conference on Physics of Ionized Gases, (Akademii Republicii Socialiste Romania, Bucharest, 1969), p. 170.

87. B. Van Der Sijde, Proceedings of the Ninth Conference on Physics of Ionized Gases, (Akademii Republicii Socialiste Romania, Bucharest, 1969), p. 630

88. F. Boeschoten and L. J. Demeter, Plasma Phys. 10, 319 (1968).

89. E. T. Gerry and D. J. Rose, J. Appl. Phys. 37, 2715, 2725 (1966).

90. G. K. McCormick and L. M. Lidsky, Proceedings of the Conference on Hollow Cathode Discharges and Their Applications, (Laboratoire de Physique des Plasmas, Université Paris - Sud, Orsay, 1971), p. 43.

91. A. Simon, Phys. Rev. 98, 317 (1955); Proc. Second Intern. Conf. on Peaceful Uses of Atomic Energy, Geneva, 1958 (United Nations, Geneva, 1958), Report No. 366.

92. D. L. Morse, Phys. Fluids 8, 1339 (1965).

93. K. Chung, K. Huang and T. McManamy, Bull. Am. Phys. Soc. 15, 96 (1970).

94. K. Chung and D. J. Rose, Appl. Phys. Letters 11, 247 (1967).

95. G. M. Wheeler, Lawrence Laboratory Report No. 577, University of California, Berkeley, California, January 1972; Bull. Am. Phys. Soc. 17, 1012 (1972).

96. J. H. Noon, H. A. Schmidt and E. H. Holt, Plasma Phys. 12, 477 (1970).

97. J. C. Woo and D. J. Rose, Phys. Rev. Letters 19, 104 (1967).

98. B. E. Keen and R. V. Aldridge, J. Phys. A4, 120 (1971).

99. B. E. Keen, Phys. Rev. Letters 24, 259 (1970).

100. F. F. Chen, Phys. Fluids 9, 965 (1966).

101. F. W. Perkins and D. L. Jassby, Phys. Fluids 14, 102 (1971).

APPENDIX

Steady-State Theory of a Discharge Column in a Magnetic Field: Separable Solutions for a Finite Cylinder*

D.B. Ilić and S.A. Self

Institute for Plasma Research, Stanford University, Stanford, California 94305

(Received 17 January 1972)

The problem of the steady state of a magnetized discharge of the positive column type, in the case of a finite cylinder, is shown to have separable solutions for the radial and axial dependence of plasma density, potential, and electron and ion velocities. Consequently, the results of the corresponding one-dimensional theory may be directly applied to the two-dimensional case. In particular the theory is applicable to the case of a low-pressure discharge in a strong magnetic field, where the radial flow is collision dominated but the axial motion is collisionless.

I. INTRODUCTION

The steady state of dc or rf discharges, maintained by volume ionization against wall recombination, has been analyzed rather extensively in the case of the one-dimensional problem (infinite slab or cylinder). Such theories predict the profiles of plasma density n, potential ϕ, average velocities $v_{e,i}$, and sometimes temperatures $T_{e,i}$ of electrons and ions. The treatments vary considerably, depending on the pressure regime, and whether an external magnetic field is present. Most theories assume quasineutrality $n_e = n_i (\equiv n)$ and thereby do not treat the sheath region adjacent to the wall.

For unmagnetized discharges at pressures (strictly the pressure-radius product) high enough so that both electrons and ions are collision-dominated, the ambipolar diffusion theory[1] employs the first two moments of the Boltzmann equation (i.e., continuity and momentum transfer) for electrons and ions, neglecting inertia, the set being closed by assuming constant temperatures T_e, T_i (isothermal assumption). At lower pressures, where the particle motions are collisionless, it is common to assume that the electrons obey a Maxwell-Boltzmann distribution, while the ions are treated either by exact equations of motion[2,3] or by collisionless fluid equations.[4,5] In the latter case, use is made of either two moments neglecting pressure, or three moments neglecting heat flow. By including ion inertia, all the theories for low pressure lead to a plasma-sheath boundary not given by the inertialess ambipolar diffusion theory. A unified theory for a one-dimensional unmagnetized discharge at arbitrary pressure was developed by Self and Ewald,[6] using two moments for electrons and ions, including ion inertia and using the isothermal assumption. In this work, the pressure appears via a parameter $A = \nu^I/(\nu^I + \nu_i)$ where ν^I is the electron collision frequency In the low-pressures ($A \to 1$) limit the results approximate those of the low-pressure theories, while at high pressures ($A \to 0$) they go over to those of the ambipolar diffusion theory, but with a plasma-sheath boundary at the wall.

For a discharge in a uniform external magnetic field B, the one-dimensional problem is modified for flow across the field by the effect on the electrons and, to a lesser extent, the ions. For high pressures, the ambipolar diffusion theory was generalized to this case by Tonks.[7] For low pressures, the transverse electron motion becomes collision dominated for very weak magnetic fields, and the assumption of a Maxwell-Boltzmann distribution can no longer be made. Treatments using two moment equations for the electrons, and collisionless moment equations including inertia for the ions, have been given. Forrest and Franklin[8] used two moments for the ions, neglecting the magnetic field on the ions, while Self[9] used three moments and included the magnetic field on the ions. To deal with the magnetized discharge at arbitrary pressure, Ewald, Crawford, and Self[10] generalized the treatment of Self and Ewald by including the magnetic field in the two-moment equations for electrons and ions, using the isothermal assumption and including ion inertia. A similar treatment, but neglecting the magnetic field on the ions was given by Forrest and Franklin.[11] The solutions for the profiles of n, ϕ, and $v_{e,i}$, depend on pressure and magnetic field primarily through the parameter $C^2 \equiv [1 + (\omega_{ce}/\nu_e)^2](1 - A)/(\mu_e/\mu_i)$, where the mobility ratio (μ_e/μ_i) is a function only of gas type. For low pressures and low magnetic fields ($C^2 \lesssim 1$) the results approximate those of the low-pressure field-free theories. With increasing pressure and, or magnetic field, the results go over to those of the ambipolar diffusion theory but with a plasma-sheath boundary. It should be noted that the magnetic field causes the transverse flow to become collision dominated even though the pressure is low and motion along the field is collisionless.

For two-dimensional discharges (e.g., finite cylinder), solutions by separation of variables have been found in a number of cases subject to an assumption that the flow is separately ambipolar in the two dimensions. This assumption, that $v_{ir} = v_{er}$ and $v_{iz} = v_{ez}$ [or $(v_{iz} - v_{ez}) = J_z(r)/en(r)$, independent of z, to allow for an axial current]

excludes the possibility of Simon diffusion[12] in a discharge with conducting walls. For high pressures, the inertialess ambipolar diffusion theory, both with and without an axial magnetic field, has been solved for a finite cylinder by separation of variables by Brown.[13] For low pressures, and $B=0$, Kino and Shaw[4] solved two-dimensional problems by separation of variables, using a Maxwell-Boltzmann distribution for the electrons and two moments for the ions, including inertia, but neglecting pressure. They also assumed that the ion motion was irrotational ($\nabla\times\mathbf{v}_i=0$).

In recent years, a number of long cylindrical discharge configurations have been employed for the study of plasma-wave propagation and instabilities. These include the low-pressure positive column, the hollow cathode arc, and electron cyclotron resonance discharges. Typically, in all these cases, the pressure is low and the magnetic field high, so that while the axial motion is essentially collisionless, the transverse motion is collision dominated. Under these conditions, the axial plasma flow may dominate the radial flow, even though the column is physically very long compared with its diameter, and a suitable two-dimensional steady-state theory is necessary to describe it. The problem was recognized by Flannery and Brown[14] in a study of current-driven perturbations in a hollow cathode arc. They used the inertialess diffusion equations for the transverse motion and took account of the axial free streaming by an approximation based on the theory of Self and Ewald.[6]

In the present work, we show that within the formulation of Ewald, Crawford, and Self[10] for a discharge in a magnetic field at arbitrary pressure, separable solutions may be found for two- (or three-) dimensional problems. Thus the problem of the finite cylinder reduces to the separate problems for axial and radial flow, for which solutions have already been given. In particular, this allows a proper description of the important case of a magnetized discharge column at low pressures, where the axial flow is collisionless, but the radial flow is collision dominated.

II. THEORY

Consider a cylindrical weakly ionized discharge of radius a, length L, in a uniform external magnetic field B_z, maintained by volume ionization at a rate $\nu^I(T_e)n$, where $n=n_e=n_i$ is the plasma density in the quasineutral approximation. In general, all quantities are functions of coordinates r and z, but are assumed independent of azimuth θ.

The continuity equations for electrons and ions are

$$\nabla\cdot n\mathbf{v}_{e,i}=\nu^I n. \tag{1}$$

Combining them we have

$$\nabla\cdot(n\mathbf{v}_e-n\mathbf{v}_i)=0. \tag{2}$$

For insulating walls, we must have $v_{er}=v_{ir}$ at $r=a$. While this condition is not sufficient to ensure that the radial flow is ambipolar everywhere, we shall consider only the case where this holds. Thus

$$v_{er}=v_{ir}\equiv v_r. \tag{3}$$

In general a current J_z flows in the axial direction in response to an externally applied voltage. According to Eqs. (2) and (3) it must depend only on r; thus

$$ne(v_{iz}-v_{ez})=J_z(r). \tag{4}$$

We note that in general the azimuthal (Hall) current is nonzero ($v_{e\theta}\neq v_{i\theta}$).

The equation of momentum transfer, assuming constant temperatures $T_{e,i}$ (energy units) may be written for either species:

$$(\mathbf{v}\cdot\nabla)\mathbf{v}=(q/m)(\mathbf{E}+\mathbf{v}\times\mathbf{B})-(T/m)\nabla\ln n-\nu'\mathbf{v}, \tag{5}$$

where $\nu'\equiv\nu^I+\nu$, and ν is the collision frequency for momentum-transfer collisions with neutrals.

For electrons, Eq. (5), neglecting the nonlinear inertia term, may be solved for the velocity components

$$v_r=\mu'_{e\perp}\frac{\partial\phi}{\partial r}-D'_{e\perp}\frac{\partial\ln n}{\partial r}, \tag{6a}$$

$$v_{e\theta}=(\omega_{ce}/\nu'_e)v_r, \tag{6b}$$

$$v_{ez}=\mu'_e\frac{\partial\phi}{\partial z}-D'_e\frac{\partial\ln n}{\partial z}, \tag{6c}$$

where ω_c is the cyclotron frequency, and the parallel and transverse mobilities and diffusion coefficients are defined by

$$\mu'_e=\frac{e}{m_e\nu'_e},\qquad D'_e=\frac{T_e}{m_e\nu'_e},$$

$$\mu_{e\perp}=\frac{\mu'_e}{1+(\omega_{ce}/\nu'_e)^2},\qquad D'_{e\perp}=\frac{D'_e}{1+(\omega_{ce}/\nu'_e)^2}.$$

Retaining the nonlinear inertia terms for the ions, we have from Eq. (5) the component equations

$$v_r\frac{\partial v_r}{\partial r}-\frac{v_{i\theta}^2}{r}+v_{iz}\frac{\partial v_r}{\partial z}=-\frac{e}{m_i}\frac{\partial\phi}{\partial r}+\omega_{ci}v_{i\theta}-\frac{T_i}{m_i}\frac{\partial\ln n}{\partial r}-\nu'_i v_r, \tag{7a}$$

$$v_r\frac{\partial v_{i\theta}}{\partial r}+\frac{v_r v_{i\theta}}{r}+v_{iz}\frac{\partial v_{i\theta}}{\partial z}=-\omega_{ci}v_r-\nu'_i v_{i\theta}, \tag{7b}$$

$$v_r\frac{\partial v_{iz}}{\partial r}+v_{iz}\frac{\partial v_{iz}}{\partial z}=-\frac{e}{m_i}\frac{\partial\phi}{\partial z}-\frac{T_i}{m_i}\frac{\partial\ln n}{\partial z}-\nu'_i v_{iz}. \tag{7c}$$

Taking n and ϕ to be separable in the forms $n=n_0\mathcal{R}(r)\times Z(z)$, $\phi=\phi_r(r)+\phi_z(z)$, and $J_0\mathcal{R}(r)$, where subscript zero refers to the origin, it follows from Eqs. (4), (6), and (7) that v_r, $v_{e\theta}$, $v_{i\theta}$ depend only on r, while v_{ez}, v_{iz} depend only on z. Then Eqs. (7a) and (7b), give the radial dependence of v_r, $v_{i\theta}$ and are identical to Eqs. (6) and (7) of Ref. 10 with $\beta=1$ for an infinite cylinder, while Eq. (7c) gives the axial dependence of v_{iz} and is identical to Eq. (7) of Ref. 6 for planar geometry.

On expanding the continuity equation, we note that it separates into radial and axial parts

$$\frac{dv_r}{dr}+\frac{v_r}{r}+v_r\frac{d(\ln\mathcal{R})}{dr}=\nu_r^I=\text{const}, \tag{8a}$$

$$\frac{dv_{iz}}{dz}+v_{iz}\frac{d(\ln Z)}{dz}=\nu_z^I=\text{const}, \tag{8b}$$

where

$$\nu_r^I+\nu_z^I=\nu^I. \tag{9}$$

This indicates that the plasma generated at a volume rate $\nu^I n$ at every point flows radially and axially in a fixed ratio ν_r^I/ν_z^I.

Equation (8a) is identical to Eq. (9) of Ref. 10, when $A \equiv \nu^I/\nu_i'$ is replaced by $A_r \equiv \nu_r^I/\nu_i'$. Together with Eqs. (6a), (7a), and (7b), it forms a closed set for the quantities $\mathfrak{R}(r)$, $\phi_r(r)$, $v_r(r)$, and $v_{i\theta}(r)$, identical to the treatment of Ref. 10 for an infinite cylinder. Consequently we may use the numerical solutions given there for these quantities. Furthermore, it was shown in Ref. 10 that the solutions have a singularity, identified as a plasma-sheath boundary at $r=a$, where $v_r = c_s \equiv [(T_e + T_i)/m_i]^{1/2}$, the ion sound speed. Numerical values of the normalized tube radius

$$s_r \equiv (m_i/T_e)^{1/2}\nu_i' a \tag{10}$$

were given as a function of the normalized parameters $R' \equiv (\mu_e/\mu_i)/(1-A)$, A (taken as A_r in the present case), $\tau \equiv T_i/T_e$, and $C^2 \equiv [1+(\omega_{ce}/\nu_e)^2](1-A)/R$. These may be used, in conjunction with similar results for the axial problem, to determine the ratio ν_r^I/ν_z^I as described below.

Considering now the axial dependence, Eq. (8b) is identical to Eq. (9) of Refs. 6 and 10, when A is replaced by $A_z \equiv \nu_z^I/\nu_i'$. Together with Eqs. (4), (6c), and (7c), it forms a closed set for $Z(z)$, $\phi_z(z)$, $v_{ez}(z)$, and $v_{iz}(z)$. These equations differ from those of Refs. 6 and 10 through the inclusion of the axial current in the present case. Elimination of ϕ_z and v_{ez} between Eqs. (4), (6c), and (7c) yields

$$v_{iz}\left(\frac{dv_{iz}}{dz} + \frac{m_e\nu_e'}{m_i}\right) + c_s^2\frac{d\ln Z}{dz} = \frac{m_e\nu_e'}{m_i}\left(\frac{J_0}{n_0 e}\right)\frac{1}{Z}. \tag{11}$$

From Eqs. (8b) and (11) we have

$$\frac{dv_{iz}}{dz} = \frac{\nu_z^I c_s^2 + (\nu_i' + m_e\nu_e'/m_i)v_{iz}^2 - (m_e\nu_e'/m_i)(J_0/n_0 e)v_{iz}Z^{-1}}{c_s^2 - v_{iz}^2}. \tag{12}$$

This shows the occurrence of singularities where $v_{iz} = \pm c_s$, corresponding to plasma-sheath transitions at the axial boundaries. In general, Eqs (8b) and (11) must be solved together numerically for $v_{iz}(z)$ and $Z(z)$, and hence $v_{ez}(z)$ and $\phi_z(z)$, as discussed below.

In the case of zero axial current ($v_{iz} = v_{ez}$) corresponding to an rf-maintained discharge, Eq. (12) may be integrated to give analytic solutions for v_z, ϕ_z, and Z as discussed in Ref. 6. In this case the discharge is symmetric about the center plane which is conveniently taken as the origin $z=0$. The normalized half-length is given, from Eq. (20) of Ref. 6, as

$$s_z \equiv \left(\frac{m_i}{T_e}\right)^{1/2}\nu_i'\left(\frac{L}{2}\right) = \frac{(1+\tau)^{1/2}}{A_z^{1/2}}\,\frac{1+1/R'+A_z}{(1+1/R')^{3/2}}\tan^{-1}\left(\frac{1+1/R'}{A_z}\right)^{1/2} - \frac{(1+\tau)^{1/2}}{1+1/R'}, \tag{13}$$

where $\tau = T_i/T_e$ and $R' = (\mu_e/\mu_i)/(1-A)$.

To complete the solution for a finite cylindrical discharge in the case of zero current, it remains to give a prescription for determining the ratio $\nu_r^I/\nu_z^I = A_r/A_z$ corresponding to some particular experimental conditions. For a one-dimensional discharge it was pointed out in Refs. 6 and 10 that it is usually possible to determine all the parameters appearing in the theory with reasonable precision from experimental values, with the exception of ν^I. This is because the electron distribution is never accurately Maxwellian at high energies, so that calculations of $\nu^I(T_e)$ based on known collision cross sections and a Maxwellian electron distribution can give quite incorrect values. On the other hand, it was shown that, knowing the other parameters, one can use the numerical results for the normalized dimensions $s_{r,z}(R, A, C, \tau)$, in conjuntion with the definitions of $s_{r,z}$, to determine the value of ν^I, and a graphical procedure was given for doing so. For the finite cylindrical discharge, similar methods may be used, employing the numerical values of s_r and s_z for the radial and axial solutions to determine ν_r^I and ν_z^I and thus fully specify the parameters in the theory appropriate to a particular experimental discharge.

This is particularly simple to do for the case of a magnetized low-pressure discharge such that the axial flow dominates the radial flow ($\nu_r^I \ll \nu_z^I \approx \nu^I \gg \nu_i$). For the axial problem we may use the analytic result, Eq. (13), in the approximation $R' \gg 1$, $\tau \ll 1$,

$$s_z \equiv (m_i/T_e)^{1/2}\tfrac{1}{2}\nu_i' L \approx \tfrac{1}{2}\pi - 1 \approx 0.57, \tag{14}$$

to determine $\nu_z^I \approx \nu^I$. For the radial problem we may use the analytic result corresponding to the ambipolar diffusion limit, $\tau \ll 1$, $C \gg 1$,

$$s_r \equiv (m_i/T_e)^{1/2}\nu_i' a \approx 2.4/A_r^{1/2}C, \tag{15}$$

to determine $A_r = \nu_r^I/\nu_i'$, and hence ν_r^I.

From Eqs. (14) and (15) we then have

$$A_r \approx \frac{\nu_r^I}{\nu_z^I} \approx \left(\frac{2.4}{0.57}\right)^2\frac{(L/2a)^2}{C^2} \approx \frac{(2.4/0.57)^2(\mu_e/\mu_i)}{\tfrac{1}{2}(m_i/T_e)^{1/2}\nu_i L}\,\frac{(L/2a)^2}{(\omega_{ce}/\nu_e)^2} \ll 1. \tag{16}$$

This gives a condition on the length/diameter ratio, magnetic field, and pressure, that the discharge be dominated by flow to the ends rather than the side walls. Typically $\mu_e/\mu_i \approx 50 \sim 500$ for most gases, while the term $\tfrac{1}{2}(m_i/T_e)^{1/2}\nu_i L$ is a measure of the probability ($\ll 1$) that an ion suffers a collision in transit to the ends. Thus it follows that the ratio ω_{ce}/ν_e must exceed the ratio $L/2a$ by a considerable factor before the end losses become dominant.

It remains to discuss the effect of axial current on the axial profiles, which must be found by solving Eqs. (8b) and (11) numerically. In this case the profiles are no longer symmetric about the center plane and it is convenient to take the origin $z=0$ at the point where $v_{iz}=0$. Some typical computer solutions for the profiles of n, ϕ_z, and v_{iz} are shown in Fig. 1, for various values of normalized current. The normalized distances to the plasma-sheath boundaries s_{z+} and s_{z-} are no longer equal, and in place of Eq. (13) we must use the condition

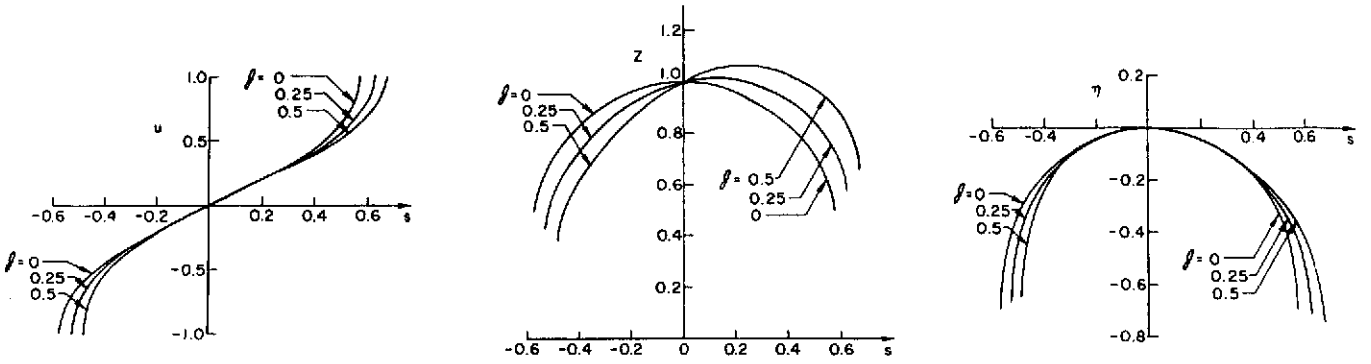

FIG. 1. Axial profiles of normalized ion velocity $u \equiv (m_i/T_e)^{1/2} v_{iz}$, plasma density $Z \equiv n(z)/n(0)$, and potential $\eta \equiv e\phi/T_e$ vs normalized distance $s \equiv (m_i/T_e)^{1/2} \nu_i' z$, for various values of normalized current density $\mathcal{J} \equiv (J_0/n_0 e)\ (m_i/T_e)^{1/2}/R'$, computed for low pressures, $A \approx 1$, and zero ion temperature, $\tau = 0$.

$$s_{g+} - s_{g-} = (m_i/T_e)^{1/2} \nu_i' L. \tag{17}$$

However, in practice, the numerical solutions show that for moderate currents, $s_{g+} - s_{g-} \approx 2 s_g$, where s_g is the value with zero current. Consequently, for moderate currents, it is sufficient to determine the parameters ν_r^I, ν_z^I using the results for zero current, as described above.

III. DISCUSSION

Within the framework of a discharge theory based on the first two moments of the Boltzmann equation for electrons and ions, assuming constant temperatures $T_{e,i}$, we have shown how separable solutions may be obtained for the radial and axial profiles of plasma density, potential, and electron and ion velocities in a weakly ionized magnetized cylindrical discharge column maintained by volume generation against wall recombination. Separation of the radial and axial variations allows the one-dimensional results of Ewald, Crawford, and Self to be directly applied to the finite cylinder. The theory provides a description of a short cylindrical discharge of the positive column type with insulating side walls when the tube is short ($L/a \gg 1$), or when it is long and the magnetic field accentuates flow to the ends. It is particularly relevant to the commonly encountered case of a low-pressure discharge column in a strong magnetic field, when the radial flow is collision dominated but the axial flow is collisionless, and for which the usual inertialess ambipolar diffusion theory is inappropriate.

The theory is not directly applicable to intense arcs at high pressure or in strong magnetic fields, such as the hollow cathode discharge, since in such cases the Joule heating combined with the low transverse thermal conductivity leads to appreciable radial temperature gradients. To describe this situation one must abandon the isothermal assumption and employ the third-moment (heat-transfer) equations. Furthermore, if the plasma is appreciably ionized, it is necessary to include collisions of charged particles among themselves. While one-dimensional theories can be developed on this basis, we have so far been unable to find separable solutions for two dimensions in this case.

ACKNOWLEDGMENTS

We are indebted to Dr. F.W. Crawford for useful discussions and T.D. Rognlien for performing the computations.

*Work supported by U.S. Air Force, Office of Scientific Research.

[1]W. Schottky, Physik Z. 25, 635 (1924).
[2]L. Tonks and I. Langmuir, Phys. Rev. 34, 876 (1929).
[3]S.A. Self, J. Appl. Phys. 36, 456 (1965).
[4]G.S. Kino and E.K. Shaw, Phys. Fluids 9, 587 (1966).
[5]L.C. Woods, J. Fluid Mech. 23, 315 (1965).
[6]S.A. Self and H.N. Ewald, Phys. Fluids 9, 2486 (1966).
[7]L. Tonks, Phys. Rev. 56, 360 (1939).
[8]J.R. Forrest and R.N. Franklin, Brit. J. Appl. Phys. 17, 1061 (1966).
[9]S.A. Self, Phys. Fluids 10, 1569 (1967).
[10]H.N. Ewald, F.W. Crawford, and S.A. Self, J. Appl. Phys. 38, 2753 (1967).
[11]J.R. Forrest and R.N. Franklin, Brit. J. Appl. Phys. 17, 1569 (1966).
[12]A. Simon, Phys. Rev. 98, 317 (1955); *Proceedings of the Second International Conference on the Peaceful Uses of Atomic Energy, Geneva*, 1958 (United Nations, Geneva, 1958), Rept. No. 366.
[13]S.C. Brown, *Basic Data of Plasma Physics* (MIT, Boston, Mass., 1959), Chaps. 2 and 5.
[14]D.L. Flannery and S.C. Brown, Phys. Fluids 13, 1066 (1970).